DOKUZ EYLÜL UNIVERSITY
GRADUATE SCHOOL OF NATURAL AND APPLIED SCIENCES

STRUCTURAL ANALYSIS AND FATIGUE LIFE EVALUATION OF BRACKET TYPE COMPONENTS SUBJECTED TO RANDOM EXCITATIONS

by
Ülgen YEŞİLÇİMEN

October, 2022
İZMİR

STRUCTURAL ANALYSIS AND FATIGUE LIFE EVALUATION OF BRACKET TYPE COMPONENTS SUBJECTED TO RANDOM EXCITATIONS

A Thesis Submitted to the
Graduate School of Natural and Applied Sciences of Dokuz Eylül University
In Partial Fulfillment of the Requirements for the Degree of Master of Science
in Mechanical Engineering, Machine Theory and Dynamics Program

by
Ülgen YEŞİLÇİMEN

October, 2022
İZMİR

M.Sc THESIS EXAMINATION RESULT FORM

We have read the thesis entitled **“STRUCTURAL ANALYSIS AND FATIGUE LIFE EVALUATION OF BRACKET TYPE COMPONENTS SUBJECTED TO RANDOM EXCITATIONS”** completed by **ÜLGEN YEŞİLÇİMEN** under supervision of **PROF.DR. ZEKİ KIRAL** and we certify that in our opinion it is fully adequate, in scope and in quality, as a thesis for the degree of Master of Science.

....

Prof. Dr. Zeki KIRAL

Supervisor

....

Prof. Dr. Hasan ÖZTÜRK

(Jury Member)

....

Asst. Prof. Dr. Turgay ERAY

(Jury Member)

Prof. Dr. Okan FISTIKOĞLU
Director
Graduate School of Natural and Applied Sciences

ACKNOWLEDGEMENT

I would like to thank my thesis supervisor, Prof. Dr. Zeki KIRAL, who shared his knowledge and experience with me on all aspects of the study.

I am grateful to Turkish Aerospace for giving me this opportunity to complete my master’s degree. I want to express my gratitude to every one of my friends and coworkers who helped with the thesis preparation, offered suggestions, and offered moral support.

Lastly, I would want to offer my heartfelt gratitude to my family for their unending support and assistance.

Ülgen YEŞİLÇİMEN

STRUCTURAL ANALYSIS AND FATIGUE LIFE EVALUATION OF BRACKET TYPE COMPONENTS SUBJECTED TO RANDOM EXCITATIONS

ABSTRACT

Fatigue is a significant issue when structures are subjected to dynamic and fluctuating loads, as encountered in commercial applications like automotive, military vehicles, defense, and aircraft. When the form of the loading is dynamic, the structure's dynamics will have an influence on fatigue. Furthermore, if the frequency spectrum of the loading is wide band, the potential for driving the structure's resonant frequencies becomes considerable. The assessment of fatigue damage in aeronautical structures, those exposed to unpredictable and random loading, is of major interest, and designs are improved according to those calculations. This thesis aims to demonstrate a methodology and improvement study that includes the fatigue life estimation of hydraulic reservoir tank system components with a modal stress approach and the natural vibration modes of the system. First, modal stress analysis of the hydraulic reservoir tank system is conducted to figure out the system behavior in a dynamic structure and to obtain fatigue hotspots. The time signal is represented by its power spectral density (PSD) in the frequency domain, and fatigue analyses are realized at these hotspots to shorten the total analysis time. The Dirlik method was chosen to compute the fatigue life directly from the PSD of stress.

In this thesis, structural random-vibration fatigue evaluation of hydraulic reservoir tank system components with a modal stress approach is performed in the frequency domain by using Altair HyperWorks software with the OptiStruct solver. By performing optimization analyses for the system components, an optimized design that meets the system targets is obtained.

Keywords: Dirlik method, modal stress approach, power spectral density (PSD), random-vibration fatigue, size/parameter optimization, topology optimization

RASTGELE UYARIMA MARUZ BRAKET TİPİ BİLEŞENLERİN YAPISAL ANALİZİ VE YORULMA ÖMÜRLERİNİN DEĞERLENDİRİLMESİ

ÖZ

Yorulma, otomotiv, askeri araç, savunma ve uçak gibi ticari uygulamalarda karşılaşılan dinamik ve değişken yüklere maruz kalan yapılarda önemli bir sorundur. Yüklemenin formu dinamik olduğunda, yapının dinamikleri yorulma üzerinde etkili olacaktır. Ayrıca, yüklemenin frekans spektrumu geniş bant ise, yapının rezonans frekanslarını uyarma potansiyeli oldukça fazladır. Öngörülemeyen ve rastgele yüklemeye maruz kalan havacılık yapılarında yorulma hasarının değerlendirilmesi önemli bir ilgi alanıdır ve tasarımlar bu hesaplamalara göre geliştirilmektedir. Bu tez, hidrolik rezervuar tank sistemi bileşenlerinin modal gerilme yaklaşımı ile yorulma ömrü tahminini ve sistemin doğal titreşim modlarını içeren bir metodoloji ve iyileştirme çalışmasını ortaya koymayı amaçlamaktadır. İlk olarak, dinamik bir yapıdaki sistem davranışını anlamak ve yorulma kritik noktaları elde etmek için hidrolik rezervuar tank sisteminin modal gerilme analizi yapılır. Zaman sinyali, frekans alanındaki güç spektral yoğunluğu (PSD) ile temsil edilir ve toplam analiz süresini kısaltmak için bu kritik noktalarda yorulma analizleri gerçekleştirilir. Dirlik yöntemi, yorulma ömrünü doğrudan stresin PSD'sinden hesaplamak için seçilmiştir.

Bu tezde, OptiStruct çözücü ile Altair HyperWorks yazılımı kullanılarak frekans alanında modal gerilme yaklaşımıyla hidrolik rezervuar tank sistemi bileşenlerinin yapısal rastgele titreşimli yorulma değerlendirmesi yapılmıştır. Sistem bileşenleri için optimizasyon analizleri yapılarak sistem hedeflerini karşılayan optimize edilmiş bir tasarım elde edilir.

Anahtar kelimeler: Dirlik metodu, modal gerilme yaklaşımı, güç spektral yoğunluğu (PSD), rastgele-titreşim yorulması, boyut/parametre optimizasyonu, topoloji optimizasyonu

CONTENTS

LIST OF FIGURES

LIST OF TABLES

LIST OF SYMBOLS

σ_{max}	The maximum stress
σ_{min}	The minimum stress
$\Delta\sigma$	The stress range
$\sigma_a, \sigma_{ai}, S_a$	The stress amplitude
σ_m	The mean stress
N_f, N_{fi}	The number of cycles to failure
C, D	The fitting constants of the material on a log-linear plot
σ_f'	The constant of the material
b, k	Basquin exponent
N, N_i	The applied number of stress cycles
$E[D], \bar{D}$	The expected damage
$x(t)$	A periodic function
w_0	The fundamental frequency
c_n	The complex Fourier coefficients
τ, T_p	Time period
$X(w)$	The Fourier transform of a time signal
f, f_n	Frequency
$Y(f)$	The response FFT
$X(f)$	The input excitation
$H(f)$	The transfer function
$H^*(f)$	The conjugate of the transfer function
$G_r(f)$	The PSD of response
$G_i(f)$	The PSD of input
m_n	The spectral moments, n=0,1,2,3,4
$G(f)$	The PSD data
δf	The frequency increment
$E[0], \nu_0$	The expected number of upward zero crossings per second
$E[P], \nu_p$	The expected number of peaks per second
γ	The irregularity factor

$p_a(s)$	The amplitude probability density
$\Gamma(.)$	Euler gamma function
Z	The normalized amplitude for the Dirlik equation
x_m	The mean frequency for the Dirlik equation
G_1, G_2, G_3	The parameters for the Dirlik equation
R, Q	The parameters for the Dirlik equation
x	A vector of design variables
$g(x)$	The constraint function
$f(x)$	The objective function
$\check{K}$, K	The stiffness matrices of the penalized and original

ABBREVIATIONS

RMS	Root Mean Square
PSD	Power Spectral Density
UTS	Ultimate Tensile Strength
NB	Narrow Band
WL	Wirsching and Light
OC	Ortiz and Chen
SM	Larsen and Lutes
BT	Benascuitti and Tovo
α.75	Benascuitti and Tovo with α.75
ZB	Zhao and Baker
LaL	Lalanne
HF	High Frequency
MF	Intermediate Frequency
LF	Low Frequency
RFC	Rainflow Counting
SN	Stress Life
R	Ratio of Minimum to Maximum Stress
EN	Strain Life
FFT	Fast Fourier Transform
PDF	Probability Density Function
FE	Finite Element
AMSES	The Automated Multi-Level Sub-Structuring Eigenvalue Solution
EIGRL	The Eigenvalue Extraction Data for Lanczos
EIGRA	The Eigenvalue Extraction Data for AMSES
SIMP	Solid Isotropic Material with Penalty
RANDPS	Random Case Control
RNF	Rainflow
STL	Stereolithography

CHAPTER 1
INTRODUCTION

1.1 Fatigue

Fatigue is considered as the deterioration or eventual failure of a material under time-dependent and cyclic loads that are lower than the material's static strength (Dowling, 2013). Fatigue is critical in engineering applications because it can cause unpredictably sudden damage to load-bearing components. In addition, repair or replacement of damaged parts causes a loss of time and increases the cost.

1.2 Fatigue Mechanism

Fatigue damage is defined as the progressive, localized, and permanent microstructural change in a structure caused by variable stresses or strains. These microstructural changes could lead to cracks forming and growing, finally leading to fracture, with enough stress and strain repetitions (Schijve, 2009).

The initiation and propagation of a crack are the fatigue periods that represent a structure’s total fatigue life (Figure 1.1). A small amount of crack propagation also happens during the crack initiation stage, but fatigue cracks do not reach the size to be visible. During the propagation period, the crack broadens under the cyclic load, and when the crack size reaches a critical value, it collapses. This means that it's a crucial issue in engineering to distinguish between the initiation and propagation stages of cracks to manage crack propagation. In addition, the component's surface conditions have a major effect on crack nucleation. Stress concentrators, such as surface burrs and scratches, behave like cracks on the component surface and promote crack initiation (Schijve, 2009).

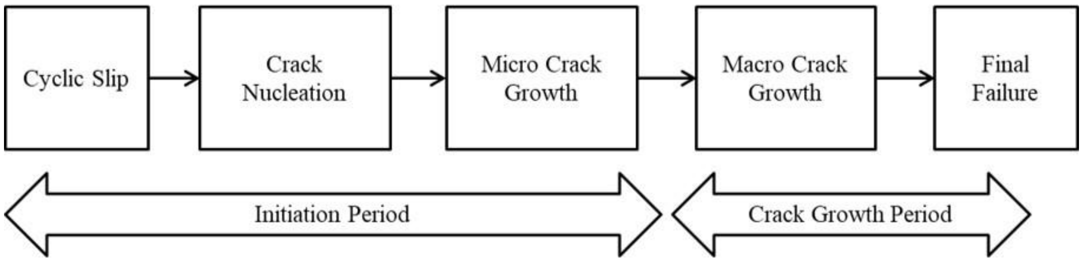

Figure 1.1 Fatigue failure process from crack nucleation to final failure (Schijve, 2009)

Cycle slips, also known as cyclic plastic deformation, that is what induces the initiation and progress of fatigue cracks in the component.

Components may sustain fatigue damage under cyclic loads and at stress amplitudes below the material yield strength. At such low stress levels, it is limited plastic deformation to a small number of grains, and due to the low slip resistance, microplasticity develops in the grains on the surface of the material. The material's free surface will be open to the external environment, such as air or liquid, and the surrounding material is only present in one direction. As a result, surface grains are less restricted to plastic deformation by neighboring grains than subsurface grains, the crack may initiate at a lower stress level (Schijve, 2009).

Nonuniform stress distribution driven by a notch, hole, or other geometric discontinuity is another reason for crack initiation on the surface. The stress on the surface increases because of this distribution. Surface roughness also contributes to the formation of surface cracks. Wear or corrosion cavities increase the possibility of crack initiation.

For there to be cyclic slip on the material, it requires cyclic shear stress, and this stress is not uniformly distributed throughout the material on a micro-scale. According to the grain's size, shape, orientation, and elastic anisotropy of the material, the shear stress on shear planes differs from grain to grain. Some grains on the material surface are more favorable to these situations than others. A slip step appears on the material surface when grain slip occurs. It is shown in Figure 1.2. This slip step means that a new fresh surface will be exposed to the external environment. This slip causes strain hardening on the slip band as the load increases. During unloading, the same slip band will encounter a higher shear stress in the opposite direction. As a result, opposing slip will happen on adjacent parallel slip planes even if it happens on the identical slip band (Schijve, 2009).

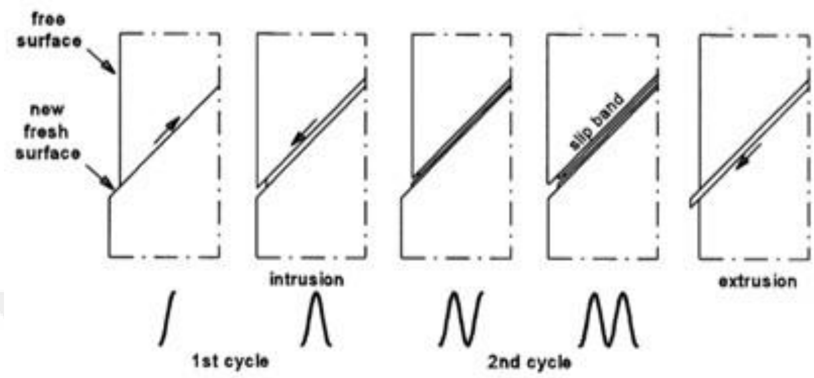

Figure 1.2 Crack nucleation due to successive slip (Schijve, 2009)

Fatigue is a fundamental surface phenomenon of materials during the crack initiation phase. In summary about crack initiation:

I. Applying a single cycle is all that is required to develop a microcrack or intrusion into the material.
II. The first cycle's process is performed in the second cycle and all succeeding cycles. The crack grows with each cycle.
III. The formation of the first microcrack occurs along the slip plane. This slip band is actually a microcrack.
IV. The slip plane grows in forward slip (intrusion) and backward slip (extrusion).
V. The bonds between atoms weaken as a result of slipping. This also applies to the tip of a growing fatigue crack.

A microcrack drives a non-uniform distribution of stress at the micro level. The stress is concentrated at the microcrack's tip. It is therefore attainable that more than one slip system will be stimulated. Additionally, when the crack propagates through neighboring grains into the material, because of the existence of these adjacent grains, shear displacement resistance will improve. Similarly, constraining slip displacements with a single slip plane will become progressively challenging, the number of slip planes will gradually increase. The growth direction of the microcrack in this case differs from the orientation of the first slip band. In general, it tends to expand perpendicular to the direction of loading as shown in Figure 1.3 (Schijve, 2009).

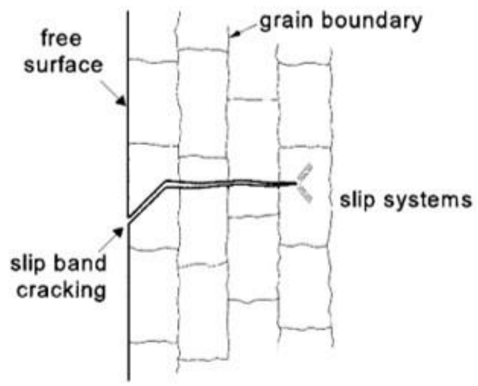

Figure 1.3 Microcrack cross section (Schijve, 2009)

Shear resistant barriers could specify a crack propagation threshold since microcrack propagation is dependent on cyclic plasticity. It is shown in Figure 1.4 that the effect of grain boundary on crack growth. When the crack approaches the first grain barrier, the growth rate, which is expressed as the length of the crack extended each cycle, diminishes. Growth is accelerated as the crack enters the second grain and slows when it reaches the boundary of the second grain. The crack grows at an increasing pace after crossing the third grain (Schijve, 2009).

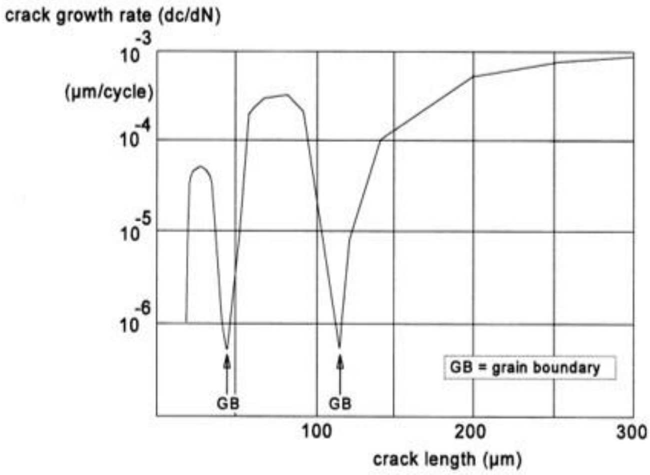

Figure 1.4 The influence of grain boundaries on crack propagation in an Al-alloy (Schijve, 2009)

In various studies, it has been observed that the growth rate of a microcrack that initially grows inhomogeneously decreases or even is over because of structural obstacles in the material. When the crack passes a large number of grains and generates a certain crack front, the situation changes. Because the crack front must grow as a whole, the crack cannot grow in various directions or at different rates in each grain. It is shown in Figure 1.5 that the crack front passes through many grains. Crack growth occurs in an almost continuous process throughout the whole crack front when the crack front is sufficiently wide to encompass a significant number of grains. The two major surface features from the initial stages have now lost their significance. The material's low resistance to cyclic slip on the surface has risen in the interior portions. Secondly, crack propagation is unaffected by characteristics of surface roughness or another surface. As a result, as the crack propagates inside the material, the material's resistance to the crack is decided by the material's characteristics as a whole. Crack growth is no longer a surface phenomenon (Schijve, 2009).

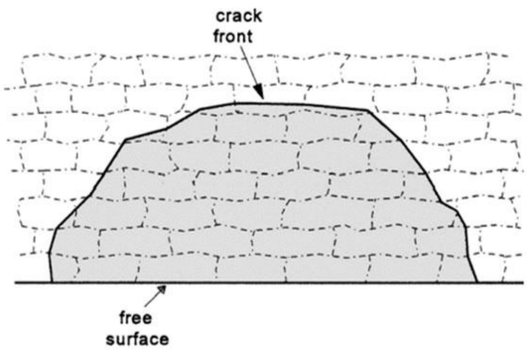

Figure 1.5 Top view of a crack illustrating how many grains the crack front passes through (Schijve, 2009)

A continuous line with a semi-elliptical form might be considered to be the crack front. The rate at which the crack progresses is determined by the material's resistance to crack propagation.

For fatigue life, surface and environmental factors might be quite significant. These factors cover any situation that might shorten the crack initiation phase. They include the occurrences that strengthen the crack initiation mechanism, in other words. Well-known effects are listed in Figure 1.6 for crack initiation and crack growth periods.

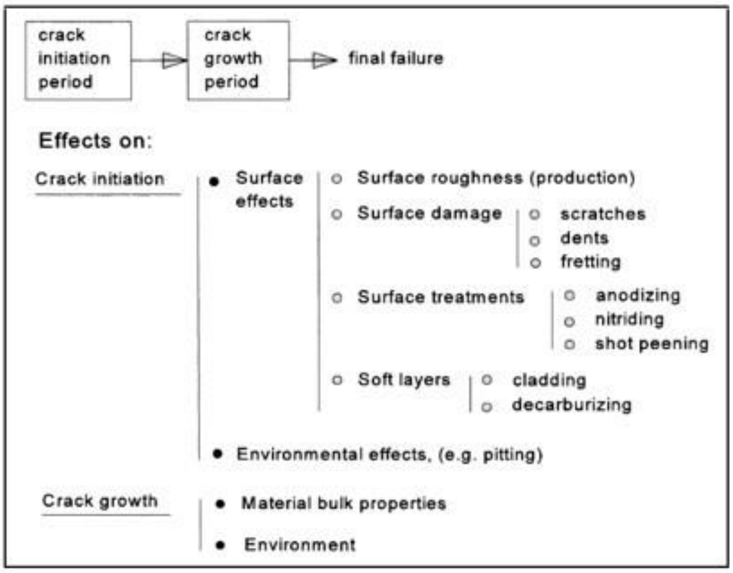

Figure 1.6 Summary table of factors that may affect crack initiation and growth processes (Schijve, 2009)

1.3 Major Fatigue Damage Accidents During in Service

For many years, metallic material fatigue has been a point of interest. This interest extends from the invention of the steam engine to the more extensive application of mechanical technologies. Numerous components are subjected to fatigue loads, and with these advances, fatigue failure assessment is becoming more commonplace.

According to experience, fractures of structures or machine parts during operational life are mostly due to fatigue. Industrial progress has always been limited by structural integrity. Its effects have become obvious with the growth of the machinery sector in the nineteenth century. Several catastrophic incidents that occurred throughout the industrial revolution have influenced the development of rail transportation. A train disaster at Versailles in 1842, for example, resulted in a huge number of deaths due to an axle fracture (Smith, 1990). This type of failure on railway transportation has tended to make scientists do extensive research into the causes of metal fatigue.

In 1919, a large tank filled with molasses exploded in Boston’s North End neighborhood owing to mechanical fatigue. In history, this event is known as "The Boston Molasses Disaster." The rivets of the 50-foot-tall tank were shot out because of the explosion, and that collapse caused a molasses wave that reached a height of 25 feet and had a peak speed of 35 mph. An elevated railway track's steel girders were destroyed by the severe wave, which also lifted many buildings off their foundations and swamped numerous city blocks. The suspected reason is that a fatigue crack starts near to the manhole cover and grows to a dangerous size (*Five disasters caused by material fatigue and what we learned from them,* 2022).

The first production commercial airliner in the history of Great Britain was the De Havilland Comet, which was constructed by De Havilland. This aircraft had a catastrophic decompression over the Mediterranean Sea on its way from Rome to London in January 1954. In investigators' reports, it was stated that the major cause of catastrophic decompression was an engine turbine explosion. After a while, this aircraft encountered another catastrophic decompression over the Mediterranean on its way from Rome to Johannesburg, only weeks after being authorized for flight. Investigators came to the conclusion that decompression was the main reason for crashes. After careful consideration, it has been realized that squared window designs cause fatigue failure due to high stress concentration and sharp corners, causing fatigue failure where repeated pressurization cycles take crucial place. Due to the fact that investigators reached a consensus that in order to reduce catastrophic events in aircraft, fatigue failures must be avoided by taking into account sharp corners in the designs.

In the Norwegian Seas of the North Sea, the oil drilling rig Alexander L. Kielland sank in 1980. There were six anchor cables on the rig, but five of them had snapped, leaving only one wire to endure the extreme stress. The cause of the collapse was determined to be fatigue cracking in one of the rig's structural braces (Naess, 1982).

In 1998, the failure of a single train wheel caused the derailment of a high-speed train, setting off a cascading effect that resulted in a bridge collapsing and more than a dozen train carriages misdirecting. Mechanical fatigue was caused by a single-cast mono-block train wheel. Following the accident, the wheel was altered to add a 20 mm thick rubber dampening ring between the metal wheel rim and the wheel's main body (*Five disasters caused by material fatigue and what we learned from them,* 2022).

1.4 Scope of the Thesis

Aviation structures are exposed to extremely high dynamic loads as a result of operational circumstances. The components exposed to these stresses may sustain severe damage. This subject is addressed in engineering under the category of random vibration fatigue. The objective of this thesis is to demonstrate the implementation of the random-vibration fatigue technique on bracket-type components subjected to dynamic loads. It is also focused on design improvements by using optimization techniques to meet frequency and fatigue targets. The studies performed in this thesis are given below.

- Examining/researching studies on random-vibration fatigue estimation.

- Determining the types of loading to which the structure is exposed and obtaining the loads.
- Preparing a finite element model of the structure and identifying boundary conditions.
- Performing modal analysis of the hydraulic reservoir tank system and examining fundamental modes of the system.
- Obtaining a unit frequency response of the structure.
- Defining random loads on the structure in the frequency domain, obtaining stress response at the exciting frequency and calculating RMS (root mean square) stresses.
- Conducting random-vibration fatigue analysis.
- To review the results of the analyses of random-vibration fatigue and natural frequency.
- To propose a methodology and improvement study to meet the system's targets
- Performing optimization analyses after defining appropriate constraints and objectives using Altair HyperWorks software and the OptiStruct solver.
- To obtain a feasible design for production by using the optimization results.
- Analyzing the final design to determine the suitability of the generated design for the target

1.5 Outline of the Thesis

Chapter 1 starts with an overview of the fatigue term, the fatigue mechanism, and the major fatigue accidents and their root causes during service.

In Chapter 2, there is a mention of a literature review about the vibration fatigue approach.

Chapter 3 is dedicated to fatigue theory. It includes discussion of both time-domain and frequency-domain approaches. The stress-based approach is extensively researched, and the effects of mean stress and counting techniques are described. The approaches of strain-based approach and the fracture mechanics are briefly explained.

The frequency domain vibration fatigue theory is thoroughly examined, including narrow band, Steinberg, and Dirlik (wide band) solutions.

Chapter 4 includes the methodology used in the thesis. It begins with the preparation of a finite element model of the hydraulic reservoir tank system, and then material information and boundary conditions are defined. The analyses of modal, frequency-response, random-response, and random-vibration fatigue and their inputs and outputs are explained in this chapter. Also, optimization techniques used are mentioned briefly.

In Chapter 5, the methodology described in Chapter 4 is applied to the hydraulic reservoir tank system and its components. The fundamental frequencies and mode shapes of the existing design are evaluated, as well as random-vibration fatigue life under multiaxial PSD (power spectral density) loading. The aim of this chapter is to perform optimization studies for the system and its components, including topology and size/parameter optimization, and then to obtain a design providing the system's targets.

Chapter 6 summarizes the results of the performed study for the hydraulic reservoir tank system. Also, the finite element analysis results and improvements to the system components are discussed.

CHAPTER 2
LITERATURE SURVEY

2.1 Background of Vibration Fatigue

The vibration-induced fatigue problem is an active research topic that is still being discussed in the literature. Halfpenny (1999) investigated appropriate techniques for performing frequency domain fatigue analysis. Evaluation of fatigue life determined from time domain approach is the traditional method, and it requires very large stress or strain time records. The frequency domain is another way to characterize a time signal. It is usually represented by power spectral density (PSD). In this study, fatigue life results are carried out in the frequency domain for several methods like Wirsching, Steinberg, Tunna, and Dirlik, and the fatigue life results of these methods are compared to those in the time domain. It is observed that Dirlik's method has been found to be widely applicable compared to other available methods. It is also illustrated how to perform finite element-based vibration analysis in frequency domain.

Benasciutti & Tovo (2005) proposed a new frequency domain fatigue damage evaluation. The effects of spectral moments and bandwidth parameters on rainflow damage are examined in this research. Using narrow and broad band frequency approaches, the advantages of the new method are demonstrated. It is a well-known fact that compared to wide band evaluation, called the Dirlik method, the narrow band approach generates results that are on the safer side. They also confirmed that result in their study. The benefit of the new method over Dirlik's approach is the ability to obtain the whole cycle distribution, including both amplitudes and mean of stresses. It is determined that the new technique appears to be a satisfactory solution to the rainflow damage assessment problem.

Demirel & Kayran (2019) performed frequency domain fatigue estimation with the Dirlik method. This study covers both fatigue evaluation numerically and experimentally on a notched beam. Vibration fatigue analyses were realized by using nCode Design Life. There are standard stress life curves of materials in this software, and two consecutive UTS values were chosen to realize fatigue analyses due to the lack of appropriate SN curves in the nCode material library according to real tensile values. Also, tensile tests were conducted in this study to extract the ultimate tensile strength (UTS) values of aluminum and steel materials. The experimentally acquired fatigue lives and UTS values are found to be in between the fatigue lives of these two consecutive UTS and their strength values, and the fatigue results are not found to have a linear relationship. This discrepancy is thought to be due to the fact that the crack initiation phase is terminated by eye examination. In addition, modal damping ratios at each natural frequency were extracted from modal testing using the half power bandwidth method. Vibration fatigue analyses were repeated with different modal damping ratios, and it was found that stress amplitudes are sensitive to changing damping ratios. Thus, it is concluded that an accurate correlation between fatigue analysis and testing also depends on accurate damping ratios.

Zigo & Arslan (2019) have suggested an effective methodology for estimating damage on spot welds in automotive parts. First, modal analysis of the structure was performed with coarse mesh to obtain actual forces and moments. The spotwelds are represented by hexahedron elements with beam elements in the coarse mesh model. In the meantime, stress tensors of spotwelds were extracted from the fine mesh analysis model under predetermined unit load cases. Using the FEMSITE database, the nodal forces of the coarse model are transformed to nodal forces of the fine mesh model of spot welds. The actual stresses on a spotweld are obtained by superposing these forces with unit stress tensors. They applied this method to obtain the fatigue lives on spotwelds and bracket surfaces of an expansion tank in a passenger car in the frequency and time domain. It was observed that the discrepancy between the damages is about 11%. It is well known that the frequency domain technique outperforms the time domain method when calculation time is compared. Also, the calculation time of fatigue analysis is reduced using both the proposed and the frequency domain approaches. It was concluded that the proposed method is a more efficient solution for a large number of spotwelds in the automotive industry.

Quigley & Lee (2016) evaluated the change of mean and standard deviation errors for several fatigue damage models in the frequency domain, considering fatigue slope exponent change. These fatigue damage models are Narrow Band (NB), Wirsching and Light (WL), Ortiz and Chen (OC), Larsen and Lutes (SM), Benascuitti and Tovo (BT), Benascuitti and Tovo with α.75 (α.75), Dirlik, Zhao and Baker (ZB), and Lalanne (LaL). For wideband random loading, the narrowband method overestimates the damage. So, there are fatigue damage models calculated from the formulation of NB multiplied with a correction factor for wideband applications like WL, OC, SM, BT, and α.75. These correction factors are a function of the fatigue slope exponent and spectral width parameter. Other methods use the probability density function formula to estimate fatigue damage. They demonstrated with test results that the approaches of OC, α.75, SM, Dirlik, and BT give considerably more precise fatigue damage than the LaL, NB, and ZB methods by using seventy power spectrum densities taken from Dirlik's dissertation. Dirlik's method is a well-known method, and it is known to give more accurate results. On the other hand, test results showed that approaches of SM, α.75, and OC have more realistic mean errors in common than Dirlik's. Compared to Dirlik, BT has a relatively small standard deviation error. They deduced that ranking the methods is complicated considering mean errors, standard deviations of the error, and slope exponents.

Zhou, Fei, & Wu (2017) performed random-vibration fatigue analysis of a plate structure that included holes with modal stress approach. They verified that the highly stressed elements in modal stress analysis become the critical regions of fatigue damage. Fatigue analysis was performed on global and local mesh models. They demonstrated that the global mesh model is time-consuming and not computationally efficient because of the requirement for refined mesh at stress concentrators. With a local mesh model, fatigue damage calculations were conducted only at fatigue critical hotspots, which are extracted from stress mode shapes. They compared analysis models in terms of memory requirement and output database size. It is concluded that the local mesh model gives accurate results and needs less computation and storage burden.

An ideal narrow-band process includes a single peak in the frequency spectrum. Some systems in offshore engineering could be excited at multiple frequency peaks. Gao & Moan (2008) proposed a method to evaluate fatigue damage in wideband processes. With this method, the wideband spectrum is separated into three segments, each having the same variance. It means that the area under the spectral density function is the same at each segment. Also, these segments have three different central frequencies: high, intermediate, and low. From the combined effects of the high frequency (HF), intermediate frequency (MF), and low frequency (LF) regions, total damage is calculated. The envelopes of these frequency regions should also be considered. The results of the proposed approach are compared to rainflow counting (RFC) results obtained using MATLAB, and also Dirlik's and Benasciutti & Tovo's results. It is also demonstrated that fatigue damage varies with bandwidth parameter. When the bandwidth parameter is ranged from 0.5 to 0.8, the proposed approach accurately estimates damage close to RFC. The fatigue damage is overestimated when the bandwidth parameter exceeds 0.85. It is indicated that for each spectral form and bandwidth parameters taken into consideration in the research, the Dirlik and Benasciutti & Tovo methods assess fatigue damage accurately.

CHAPTER 3
FATIGUE THEORY

Engineering component failures due to fatigue are a widespread issue. To analyze and design for fatigue failures in engineering components, there are three main fatigue approaches, and the stress-based approach employed in this study is one of them. Others are the strain-based approach and the fracture mechanics approach. Additionally, there are two approaches as time domain and frequency domain to predict fatigue failure according to load categorization (Benasciutti & Tovo, 2005). In this thesis, it is carried out frequency domain fatigue analysis, called the vibration fatigue method.

3.1 Stress-Based Approach

The stress-based approach is the first approach employed to understand and measure fatigue in metal materials. It is assumed that deformations are in elastic regions in this approach. Material strength parameters are significant and stress concentrations of the geometry should be considered. This approach performs the fatigue calculation by using stress-life (S-N) curves, also called Wöhler curves, of the material. It is well-known that this approach does not give accurate results in low cycle, below 1000 fatigue cycles, fatigue applications, where the stresses are in the plastic region.

To estimate fatigue life according to the stress-based approach, the cyclic loading definitions, stress-life curves of the material, empirical relationships that take into account the influence of mean stress on fatigue life, and definition of cumulative damage calculation under variable amplitude loading should be known.

3.1.1 Description of Cyclic Loading

The characteristics of cyclic loading are represented by the maximum, σ_{max}, and minimum, σ_{min}, stress levels. Other terms are derived from these stresses. Stress amplitude, σ_a, is equal to half of the stress range, $\Delta\sigma$, which is the discrepancy between the maximum and minimum values. There is significant effect of mean stress, σ_m, on fatigue life, and it is calculated by averaging the maximum and minimum values (Dowling, 2013).

$$\Delta\sigma = \sigma_{max} - \sigma_{min} \tag{3.1}$$

$$\sigma_a = \frac{\Delta\sigma}{2} = \frac{\sigma_{max}-\sigma_{min}}{2}, \quad \sigma_m = \frac{\sigma_{max}+\sigma_{min}}{2} \tag{3.2}$$

Three different stress cycles are illustrated in Figure 3.1 according to mean stresses and R-ratios.

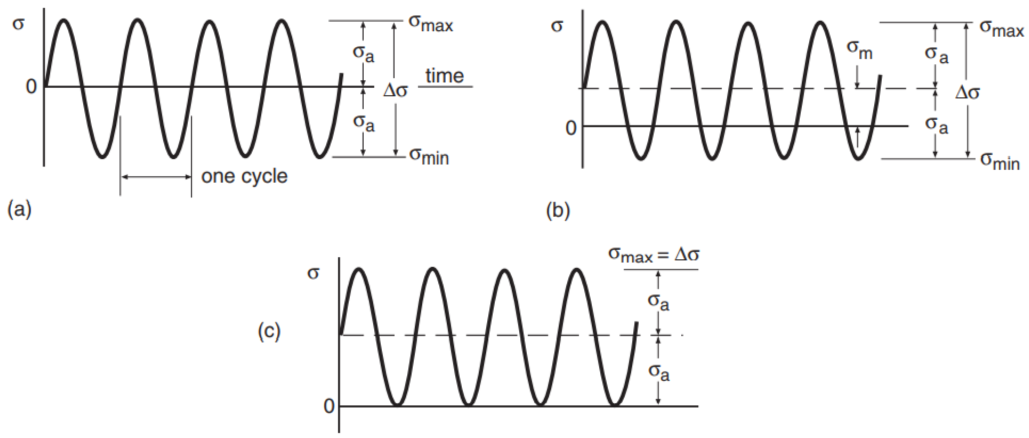

Figure 3.1 Constant amplitude loading (a) fully reversed stress cycle (b) alternating stress between minimum and maximum (c) zero to tension stress (Dowling, 2013)

3.1.2 Stress-Life (S-N) Curve or Wöhler Curve

The stress-life approach calculation is determined by considering the S-N or Wöhler curve (Dowling, 2013). To obtain the S-N curve of a material, fatigue tests of samples are performed under a number of different stress cycles, and the tests are continued until the samples fail. On the S-N curve, each stress amplitude, σ_a or S_a, is indicated against the number of failure cycles, N_f. For instance, the S-N curve of an aluminum alloy is illustrated in Figure 3.2.

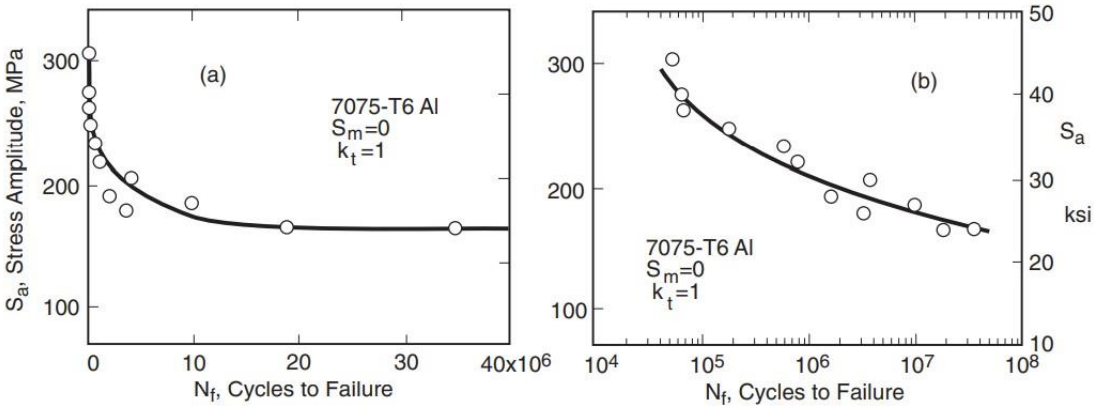

Figure 3.2 Aluminum alloy's S-N curves for unnotched samples (a) plotted on a linear scale (b) plotted on a logarithmic scale (Dowling, 2013)

When S-N data are observed to approximate a straight line on a log-linear scale, the curve can be mathematically described by matching it with the following equation.

$$\sigma_a = C + D \log N_f \tag{3.3}$$

Fitting constants are expressed by C and D. On a log-log scale, when the S-N curve may be observed to approximate a straight line, the curve can be represented as the following equation.

$$\sigma_a = \sigma_f'(2N_f)^b \tag{3.4}$$

The terms of high-cycle fatigue and low-cycle fatigue are mentioned with the S-N curve. When the stress is relatively low, high-cycle fatigue indicates a long life that is not controlled by the yielding effects. On the other hand, local plasticity is relevant to low-cycle fatigue. These terms vary with material, and the cycles below the range of 10^2 to 10^4 cycles are accepted as a low-cycle fatigue region (Dowling, 2013).

3.1.3 Mean Stress' Effect on Fatigue Life

It is necessary to take into consideration the influence of mean stress on the material's S-N curve. Increasing mean stress results in decreasing fatigue life. Considering the influence of mean stress, empirical relationships have been proposed, which are aimed at obtaining a realistic fatigue life. These are called constant life diagrams: Goodman relation (Bishop & Sherratt, 2000), Gerber relation, Soderberg relation. These relations modify stress amplitude or alternating stress according to mean stress.

3.1.4 Variable Amplitude Loading and Cumulative Damage Rule

Fatigue loadings in real life involve stress amplitudes that fluctuate irregularly. These types of loadings are called variable amplitude loadings (Dowling, 2013). The applied stress cycles number, N_i, at a certain amplitude, σ_{ai}, is extracted from the cyclic loading. Using the S-N curve, the number of stress cycles to failure, N_{fi}, is taken at that stress amplitude. Ratios of the applied stress cycle number to the failure stress cycle number are found for each stress amplitude. The expected damage, E[D], equals the sum of these ratios linearly. If expected damage is below 1, parts will not fail. This method is known as the Palmgren-Miner cumulative damage rule and is illustrated in Figure 3.3.

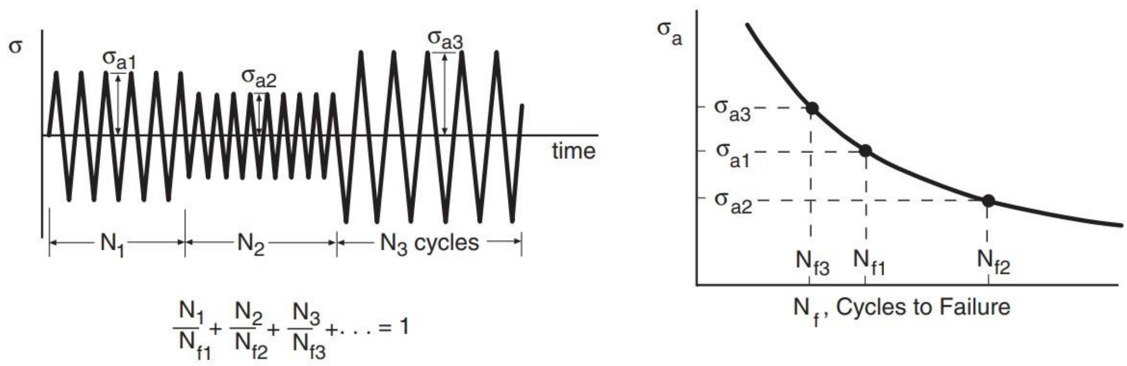

Figure 3.3 Fatigue estimation under varying stresses by Palmgren–Miner rule (Dowling, 2013)

$$E[D] = \sum_{i=1}^{j} \frac{N_i}{N_{fi}} = \frac{N_1}{N_{f1}} + \frac{N_2}{N_{f2}} + \cdots + \frac{N_j}{N_{fj}} = 1 \tag{3.5}$$

In this method, it is considered that the order in which the loads are imposed has no discernible effect on the part's lifetime. In fact, the sequence of the loads may affect the lifetime significantly.

3.1.5 Cycle Counting Method

The Palmgren-Miner rule may be implemented together with the cycle counting method to evaluate the total damage of a part exposed to variable loading. The rainflow cycle counting technique was proposed by Matsuishi and Endo (Matsuishi & Endo, 1968). Peak counting, zero-crossing, and level-crossing are further cycle counting techniques. All the parameters required for fatigue assessments under fluctuating loads are provided by imposing the rainflow cycle counting technique.

A histogram data depicting the association between amplitude, averaged stress, and the number of repeats might be provided by the rain flow cycle counting method. It is mentioned below this technique in detail (Dowling, 2013).

When counting rainflow cycles, a cycle is completed when it follows the requirement demonstrated in the Figure 3.4. If the next stress range, σ_{YZ}, is higher than or equal to the previous stress range, σ_{XY}, then the loading history of interest is assumed to include a cycle. For this cycle, the stress range and mean stress are calculated from $\Delta\sigma=\sigma_X-\sigma_Y$, and $\sigma_m=(\sigma_X+\sigma_Y)/2$, respectively.

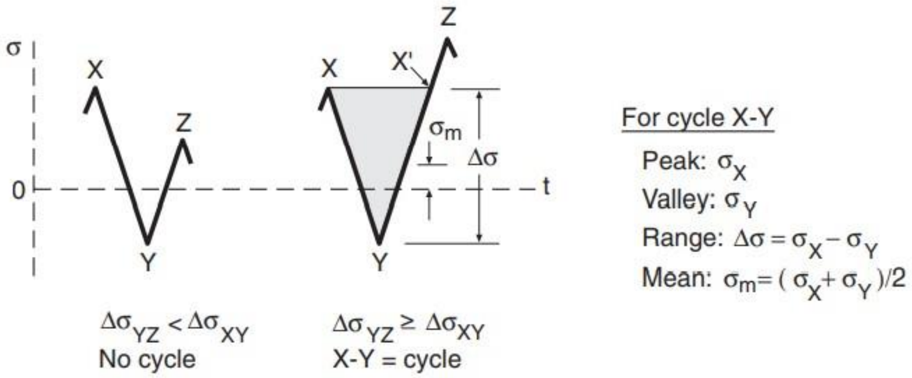

Figure 3.4 Procedures for employing the rainflow technique (Dowling, 2013)

The stress time signal is assumed to be repeatedly applied, and the rainflow cycle counting method starts with defining points of peak or valley. It is suitable to shift a portion of the time signal to the end in order to generate a sequence that initiates and terminates with the greatest peak or lowest valley. The shifting portion of the time signal is demonstrated in Figure 3.5 (a) and (b). The rearranged stress time signal is separated into cycles using the counting method that is demonstrated in Figure 3.4. When a cycle is counted, the statistical values of this cycle are recorded. The peak and trough of the recorded cycle are removed for the purpose of counting subsequent cycles, cycle E-F as demonstrated in Figure 3.5 (c). It is progressed until a count can be made if the specified location's cycles do not count. As illustrated in Figure 3.5 (d), the counting condition is then accomplished for A-B after E-F have been counted. The stress range between the greatest peak and the lowest trough, in this case, D-G, is the one that is always the biggest.

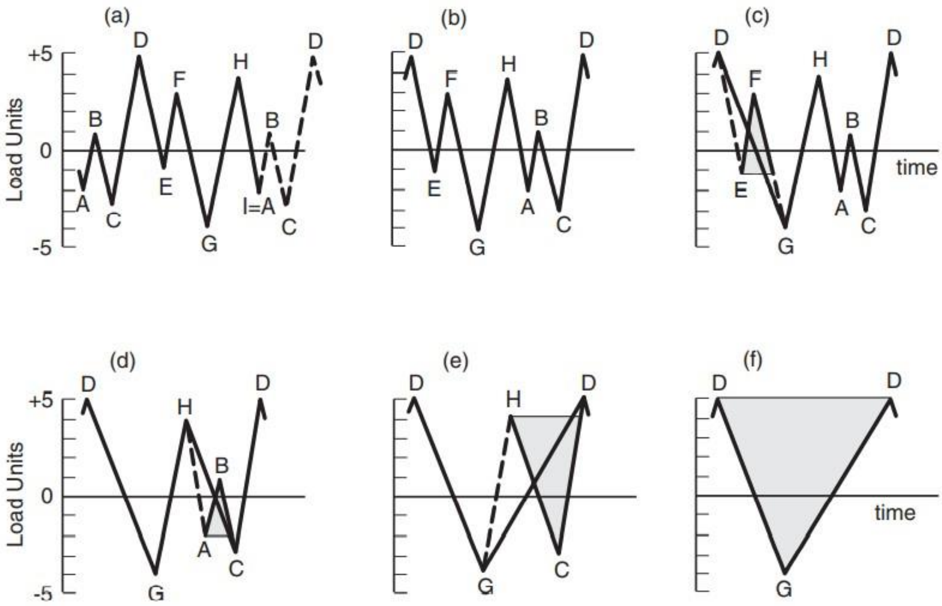

Cycle	Range	Mean
E-F	4.0	1.0
A-B	3.0	-0.5
H-C	7.0	0.5
D-G	9.0	0.5

Figure 3.5 Example of rainflow cycle counting (Dowling, 2013)

3.2 Strain-Based Approach

The strain-based approach considers cyclic plastic deformation occurring in localized regions under cyclic loading. Cyclic plastic deformation through the entire volume of the material causes changes in the mechanical properties of the material and is a prerequisite for the formation of microcracks. Fatigue cracks initiate in these microcrack regions where stress concentrators, which are like surface scratches, machining marks, holes, and also corrosion attacks, which roughen the surface. This approach performs the fatigue calculation by using strain-life (E-N) curves of the material. It considers fatigue analysis in detail, involving local yielding in parts having relatively short lifetimes. It can also be employed for applications including little plasticity at long lives, as it is a comprehensive approach compared to the stress-based approach.

3.3 Fracture Mechanics Approach

Approaches based on stress and strain are viable until the crack is initiated. When a crack initiates, it is a major issue to predict how long the propagation time of the crack will last until the fracture. The Linear Elastic Fracture Mechanics theory is used for estimating the propagation time.

3.4 Vibration Fatigue Approach

Fatigue occurs as a result of damage accumulation under cyclic loading. Loadings are categorized as deterministic cyclic loading and random loading, shown in Figure 3.6. When cyclic loading characteristics depend on time, the loading is called deterministic cyclic loading. However, every load might not be defined as a time-dependent function due to random characteristics of the loading. It is called nondeterministic or random loading (Singiresu, 2011).

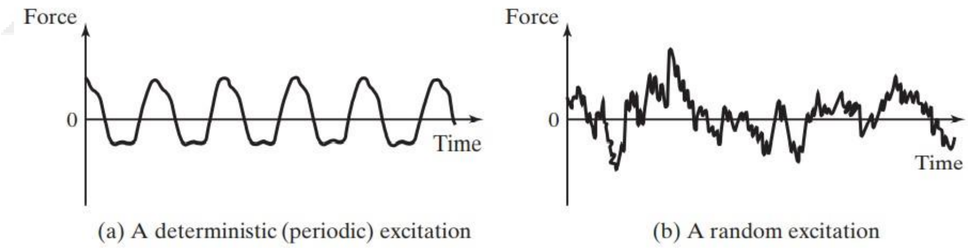

Figure 3.6 Deterministic and random loadings/excitations, respectively (Singiresu, 2011)

There are two approaches as time domain and frequency domain to evaluate fatigue failure according to load categorization. Fatigue is conventionally estimated using time-dependent signals, which are generally in the form of stress or strain. It is called the time domain approach. This approach works well for deterministic or periodic loading but requires a large number of time recordings and test results to adequately represent random loading processes.

The time domain approach is more time-consuming compared to the frequency domain approach due to the requirement for large time recordings. When the system's transfer function in the frequency domain is obtained once, fatigue assessment can be performed repeatedly under different loads (Bishop & Sherratt, 2000).

The frequency domain is another way to characterize a time signal. Methods of Fourier series expansion and Fourier transform are used to express a periodic function and a nonperiodic function in the frequency domain, respectively. These techniques allow for the acquisition of the frequency spectrum of temporal signals. It depicts mean square values of time signals versus frequency content, multiples of the fundamental frequency.

Random loadings in the time domain are usually represented by a power spectral density (PSD) in the frequency domain. The frequency content of the time signal can be demonstrated by the PSD derived by the Fourier transform (Singiresu, 2011).

3.4.1 Frequency Spectrum of a Periodic Function (Fourier Series Expansion)

A complex (exponential) Fourier series can be used to represent a periodic function x(t):

$$x(t) = \sum_{n=-\infty}^{+\infty} c_n e^{in\omega_0 t} \tag{3.6}$$

where ω_0 is the fundamental frequency given by;

$$\omega_0 = \frac{2\pi}{\tau} \tag{3.7}$$

and c_n represents the complex Fourier coefficients that may be obtained by multiplying both sides of Equation (3.6) with $e^{-in\omega_0 t}$ and integrating over one period.

$$c_n = \frac{1}{\tau}\int_{-\tau/2}^{+\tau/2} x(t)e^{-in\omega_0 t}dt \tag{3.8}$$

Equation (3.6) indicates that the x(t) function can be specified as a combination of harmonics, including various sines and cosines. The amplitudes of harmonics are found by Equation (3.8). As an example, the complex Fourier series representation of a triangular periodic function is demonstrated in Figure 3.7.

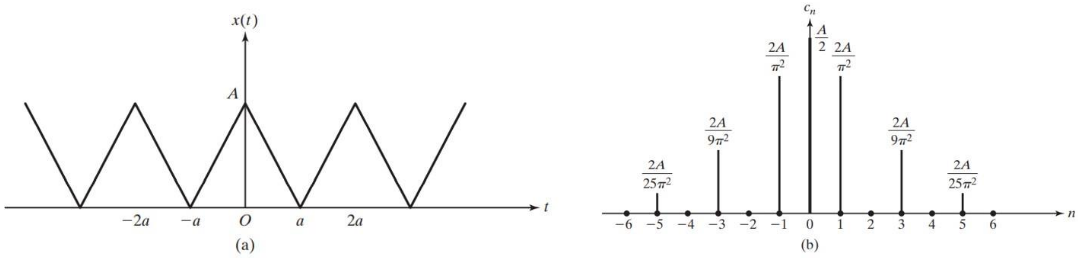

Figure 3.7 A triangular periodic function in (a), the frequency spectrum in (b) (Singiresu, 2011)

Equation (3.9) , referred to as Parseval's formula, can be used to get the mean square value of x(t). The following equation can be employed to calculate the mean square value of a function.

$$\overline{x^2(t)} = \frac{1}{\tau}\int_{-\tau/2}^{+\tau/2} x^2(t)dt = \frac{1}{\tau}\int_{-\tau/2}^{+\tau/2}\left(\sum_{n=-\infty}^{+\infty} c_n e^{in\omega_0 t}\right)^2 dt$$

$$\overline{x^2(t)} = \sum_{n=-\infty}^{+\infty} |c_n|^2 \tag{3.9}$$

3.4.2 Frequency Spectrum of a Nonperiodic Function

Nonperiodic functions could be stated as deterministic functions with infinite periods (τ→∞). The Fourier series expansion of a periodic function is represented by Equation (3.6), (3.7), and (3.8). As τ→∞, the frequency spectrum is no longer discrete and the fundamental frequency approaches infinitesimal. The fundamental frequency, ω_0 being extremely low, the following equation is derived from Equation (3.8).

$$\lim_{\tau\to\infty} \tau c_n = \lim_{\tau\to\infty} \int_{-\tau/2}^{+\tau/2} x(t)e^{-i\omega t}dt = \int_{-\infty}^{+\infty} x(t)e^{-i\omega t}dt \tag{3.10}$$

By defining X(ω) as

$$X(\omega) = \lim_{\tau\to\infty} \tau c_n = \int_{-\infty}^{+\infty} x(t)e^{-i\omega t}dt \tag{3.11}$$

It can be expressed x(t) by from

$$x(t) = \frac{1}{2\pi}\int_{-\infty}^{+\infty} X(\omega)e^{i\omega t}d\omega \tag{3.12}$$

The Fourier integral pair for nonperiodic and periodic functions is defined by equations (3.11) and (3.12). The frequency spectrum of a nonperiodic function is continuous, as opposed to the discrete frequency domain of the periodic function. As an example, the Fourier integral of a triangular pulse is demonstrated in Figure 3.8.

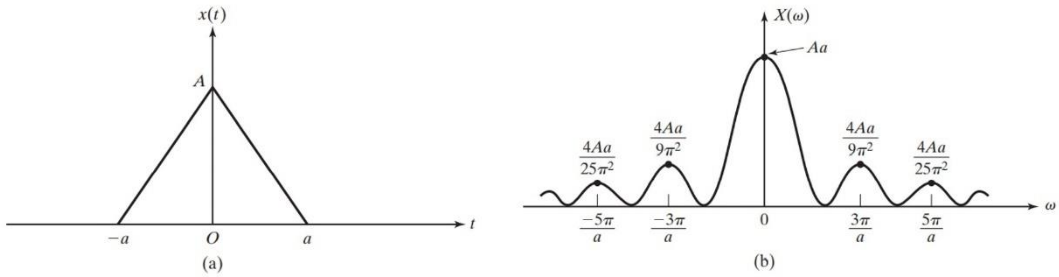

Figure 3.8 A triangular pulse (a), Fourier integral of pulse (b) (Singiresu, 2011)

Equation (3.13), referred to as Parseval's formula, can be employed to calculate the nonperiodic function’ mean square.

$$\overline{x^2(t)} = \frac{1}{\tau}\int_{-\tau/2}^{+\tau/2} x^2(t)dt = \frac{1}{\tau}\int_{-\infty}^{+\infty} \frac{|X(\omega)|^2}{2\pi\tau} d\omega \tag{3.13}$$

3.4.3 Power Spectral Density (PSD)

In practice, time signals are collected in the form of discrete data. Since the Fourier integral is employed for continuous temporal signals, a discrete Fourier integral pair that may be performed on data stored digitally is required. Cooley & Tukey (1965) developed a discrete Fourier integral methodology called the fast Fourier transform (FFT). This transform pair functions similarly to the Fourier transform pair, but on data stored digitally.

$$x(f_n) = \frac{T_p}{N}\sum_k x(t_k)e^{i\left(\frac{2\pi n}{N}\right)k} \tag{3.14}$$

$$x(t_k) = \frac{1}{T_p}\sum_n x(f_n)e^{i\left(\frac{2\pi k}{N}\right)n} \tag{3.15}$$

where T_p is the $x(t_k)$ function's period and N is the data points for Fourier integral.

Under some circumstances, time varying histories can be characterized in the frequency domain. Time varying histories cannot be characterized as deterministic, but if generated from a stationary random process, it could be described in the frequency domain. A time signal whose statistics are unaffected by a move in time origin is said to have a stationary time history. Put differently, for any values of, the statistics that apply to time history x(t) are also applicable to time history x(t+τ). The statistics derived from a sampling time history are reflective of the statistics of the entire random process.

The PSD is generated by squaring the amplitude of the FFT and reducing it by twice the period. While obtaining PSD, phase information is not contained, but each harmonic's frequency and amplitude are preserved (Bishop & Sherratt, 2000).

$$PSD = \frac{1}{2T_p}|x(f_n)|^2 \tag{3.16}$$

The entire area of the PSD curve indicates the mean square of the time history, and the harmonic wave's mean square at each peak in Figure 3.9 is expressed by the area underneath each peak. The PSD has non-negative values and can be identified in terms of x^2/unit of frequency.

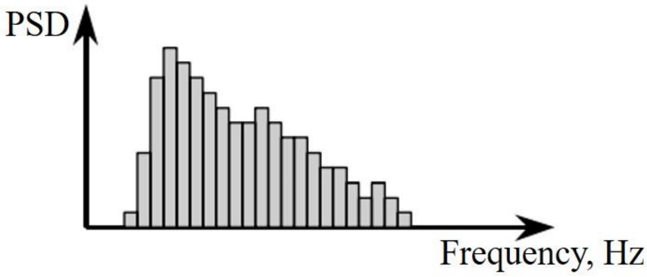

Figure 3.9 FFT to PSD transformation (Bishop & Sherratt, 2000)

In a linear system, the response of the structure is associated with the input excitation by a linear transfer function. Frequency response analysis is employed to calculate the linear systems' transfer functions at each frequency.

$$Y(f) = H(f) \times X(f) \tag{3.17}$$

Here, Y(f) is the system's FFT response, H(f) is the system's transfer function in the frequency domain, and X(f) is the excitation of the system. In this thesis, units of input excitation and the response of the system are defined as acceleration and stress, respectively. When the input excitation is specified as a PSD, the response PSD is derived by using a linear transfer function, H(f), its conjugate, $H^*(f)$, and the excitation PSD.

$$G_r(f) = H(f) \times H^*(f) \times G_i(f) \tag{3.18}$$

where the response PSD, $G_r(f)$, the excitation PSD, $G_i(f)$.

$$G_r(f) = |H(f)|^2 \times \; G_i(f) \tag{3.19}$$

Equation (3.18) can be reinterpreted in the form of Equation (3.19). $G_r(f)$ is equal to the product of the modulus square of the transfer function with $G_i(f)$. Predictions of the vibration fatigue life utilize PSD of stress directly.

3.4.4 Characterization of Engineering Processes Using Statistical Measures

It is possible to categorize engineering processes in a variety of ways. A general summary of these processes is shown in Figure 3.10.

The PSD spectrum of a sinus wave time history, as shown in Figure 3.10 (a), includes one peak amplitude centered at the frequency, and the area under this peak defines the mean square amplitude of the wave. Theoretically, for a pure sine wave, this peak should be infinitely tall and infinitely narrow. The peak, however, has a finite height and a finite width since any sinus wave utilized is finite in length. The area below the PSD plot is of significance, not the height. A broad band process consists of sine waves at various frequencies, as demonstrated in Figure 3.10 (b). In the PSD plot, they are displayed as either many distinct response peaks or a single wide peak including numerous frequencies. Figure 3.10 (c) shows a narrow-band process made of sine waves that only includes a narrow range of frequencies. Figure 3.10 (d) depicts a process of white noise. This time history is unique, composed of sine waves spanning the whole frequency range.

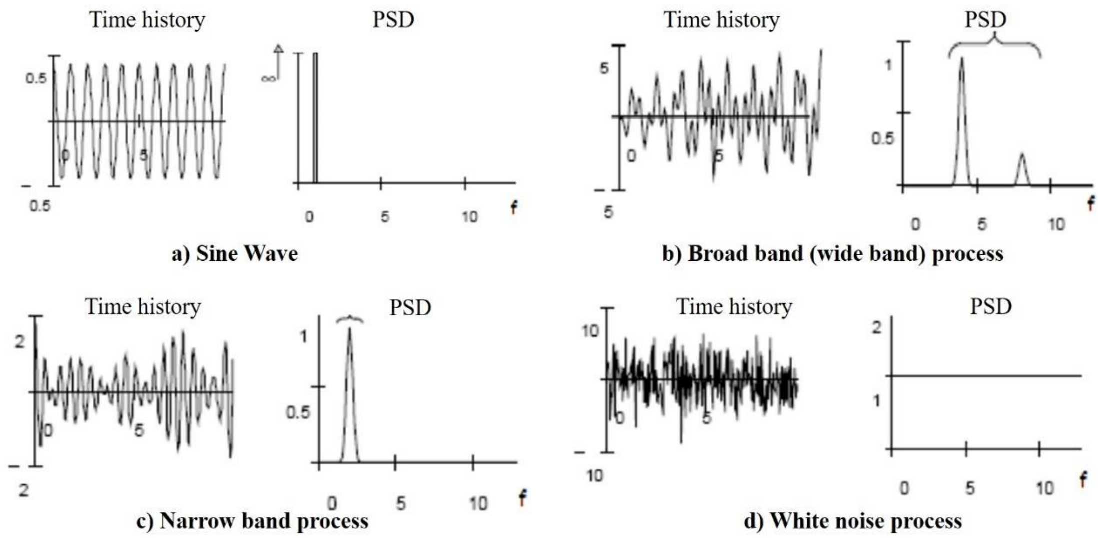

Figure 3.10 Equivalent time histories and PSDs (Bishop & Sherratt, 2000)

3.4.5 Spectral Moment Calculation of a PSD

The frequency content of the stresses is considered in vibration fatigue calculations using the stress range’s probability density function (PDF). The PSD of stresses can be employed to directly extract the PDF. The spectral moments of the PSD function are the PSD characteristics utilized to generate PDF. In theory, all computed spectral moments are required for PSD's overall characteristics. However, in practical applications, the calculation of four moments (m_0, m_1, m_2, m_4) is sufficient for fatigue damage (Bishop & Sherratt). These spectral moments provide all the information necessary for fatigue damage estimation.

Some definitions should be explained before proceeding with the fatigue analysis. When G(f) is defined as the PSD, the nth spectral moment of the PSD may also be determined. Figure 3.11 illustrates this, and the relevant formula is stated in Equation (3.20).

$$m_n = \int_0^\infty G(f)df = \sum_{k=1}^{m} f_k^n G_k(f_k)\delta f \tag{3.20}$$

where the frequency increments, δf. The root mean square value (RMS) of the PSD curve equals the square root of the first spectral moment.

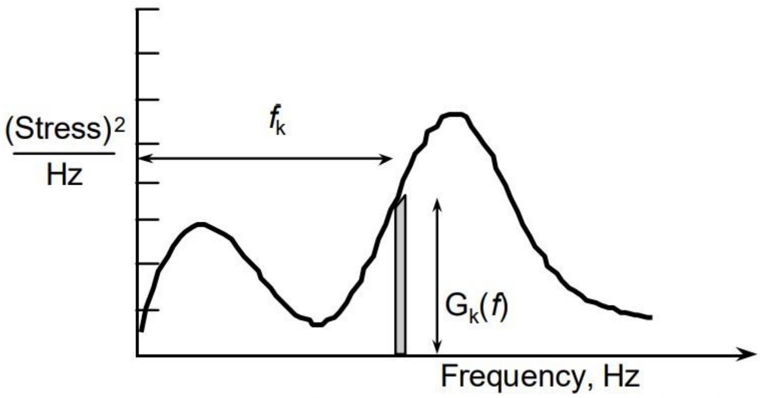

Figure 3.11 Determination of a PSD's spectral moment (Bishop & Sherratt, 2000)

3.4.6 Expected Zeros, Peaks and Irregularity Factor

The initial attempt to provide a solution for calculating damage from PSDs was offered by Rice in 1954. It is defined by two major terms: the number of upward zero crossings, E[0] or ν_0, and the number of peak crossings, E[P] or ν_p, for a random process (Rice, 1954). These terms are expressed in terms of spectral moments.

$$E[P] = \sqrt{\frac{m_4}{m_2}} \tag{3.21}$$

$$E[0] = \sqrt{\frac{m_2}{m_0}} \tag{3.22}$$

Another significant term, called the irregularity factor, is derived from spectral moments. This parameter takes values from 0 to 1. As the irregularity factor comes closer to 1, the random process reduces into a narrow spectrum. The random process turns into a broad band process as it nears to 0.

$$\gamma = \frac{E[0]}{E[P]} = \sqrt{\frac{{m_2}^2}{m_0 m_4}} \tag{3.23}$$

3.4.7 Cumulative Fatigue Damage in the Frequency Domain

Fatigue damage due to fluctuating amplitudes is estimated using the Palmgren-Miner rule, as given in Equation (3.5), in the time domain approach. This equation can be modified to be used for the frequency domain (Wijker, 2018).

The association between the occurring stress, s, and the relevant allowable number of cycles, N, can be expressed by the Basquin equation.

$$s^k N = C \tag{3.24}$$

where k and C are the material constants. Figure 3.12 demonstrates the Basquin equation.

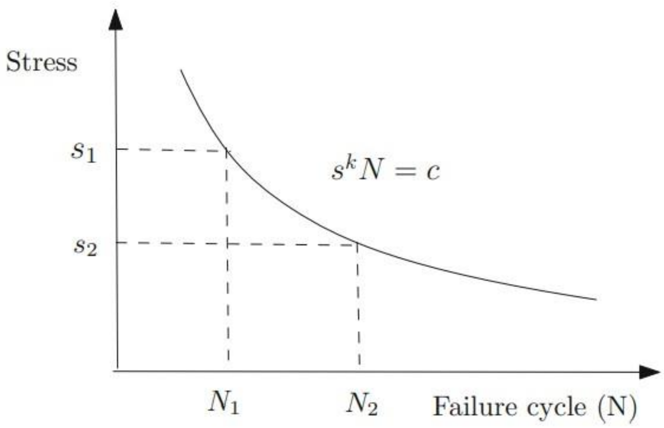

Figure 3.12 Standard Wöhler curve of a material (Wijker, 2018)

The expected damage, $\overline{D}$, per second as dependent on the Palmgren-Miner rule can be predicted by the following formulation (Wicker, 2018).

$$\overline{D} = \frac{v_p}{C}\int_0^\infty s^k p_a(s)ds \tag{3.25}$$

where the expected peak occurrence frequency, ν_p, the amplitude probability density, $p_a(s)$. The estimation of fatigue life is given by

$$T = \frac{1}{\overline{D}} \tag{3.26}$$

Several empirical solutions are proposed by researchers to ascertain the probability density function. The aim of these empirical solutions is to acquire the PDF from the output PSD and evaluate fatigue life in the frequency domain.

3.4.8 Narrow Band Approach

Bendat (1964) showed the theoretical basis of the narrow band approach that is the first approach to estimate fatigue damage from PSD of stress. The spectral moments up to m_4 are sufficient to express this process. It is assumed that each peak coincides with a stress cycle. The cycle amplitudes in this process follow the Rayleigh distribution. The formula for the narrow band approach is given below (Mrsnick & Slavic, 2013).

$$\overline{D}^{NB} = \frac{v_0}{C}\left(\sqrt{2m_0}\right)^k \Gamma\left(1+\frac{k}{2}\right) \tag{3.27}$$

For a narrow band process, the expected zero crossing intensity is very close to the peak intensity. $\Gamma(.)$ is the Euler gamma function, which is expressed as,

$$\Gamma(z) = \int_0^\infty t^{z-1}e^{-t}dt \tag{3.28}$$

For wide band random loading, the narrow band approach overestimates fatigue damage. There are various approaches that use a correction factor in the narrow band approach to obtain a more accurate result.

3.4.9 Steinberg Approach

Steinberg (2000) suggests a three-band method as an approximate estimate for the fatigue damage evaluation. In this method, the PDF of a random stress response is assumed to follow a Gaussian distribution. Certain probability levels constrain the expected values of the stress response amplitudes. The expected fatigue damage is indicated by (Wicker, 2018).

$$\overline{D}^{SB} = \frac{v_0}{C}\left[0.683\left(\sqrt{m_0}\right)^k + 0.271\left(2\sqrt{m_0}\right)^k + 0.043\left(3\sqrt{m_0}\right)^k\right] \qquad (3.29)$$

68.27%, 27.1%, and 4.3% are the probabilities that the stress amplitude cycles will not surpass the peak of one, two, and three times the RMS of the stress response signal, respectively. This method is widely utilized in the field of electronics testing.

3.4.10 Dirlik Approach

Dirlik (1985) offered an empirical formula for the probability density function, which is derived from extensive computer simulations using the Monte Carlo approach to represent the signals. A weighted summation of one exponential and two Rayleigh probability densities is used in the Dirlik approach, which was developed in 1985, to approximate the cycle-amplitude distribution. Estimates of the rainflow cycle amplitude probability density are as follows:

$$p_a(s) = \frac{1}{\sqrt{m_0}}\left[\frac{G_1}{Q}e^{\frac{-Z}{Q}} + \frac{G_2 Z}{R^2}e^{\frac{-Z^2}{2R^2}} + G_3 Z e^{\frac{-Z^2}{2}}\right] \qquad (3.30)$$

The probability density function is defined by the normalized amplitude, Z, the mean frequency, x_m, and the parameters G_1, G_2, G_3, R and Q.

$$Z = \frac{s}{\sqrt{m_0}}, \quad x_m = \frac{m_1}{m_0}\sqrt{\frac{m_2}{m_4}} \tag{3.31}$$

$$G_1 = \frac{2.(x_m - \gamma^2)}{1+\gamma^2}, \quad G_2 = \frac{1-\gamma-G_1+{G_1}^2}{1-R}, \quad G_3 = 1 - G_1 - G_2,$$
$$R = \frac{\gamma - x_m - {G_1}^2}{1-\gamma-G_1+{G_1}^2}, \quad Q = \frac{1.25.(\gamma - G_3 - G_2.R)}{G_1} \tag{3.32}$$

The closed-form expression for estimating fatigue life is as follows (Mrsnick & Slavic, 2013).

$$\overline{D}^{DK} = \frac{1}{C} v_p {m_0}^{\frac{k}{2}} \left[G_1 Q^k \Gamma(1+k) + \sqrt{2}^k \Gamma\left(1+\frac{k}{2}\right)(G_2|R|^k + G_3) \right] \tag{3.33}$$

Dirlik's empirical formula is demonstrated to be significantly superior for the PDF of rainflow stress ranges (Rahman & Ariffin, 2008). This method is more generally applicable to a wide range of problems, especially where frequency content is not narrow band.

CHAPTER 4
MODEL AND METHOD

The hydraulic reservoir tank provides the fluid required to fulfill system requirements. It also serves as an additional system to compensate for spillage or vaporization losses. The reservoir can be intended to allow for fluid expansion, to let trapped air out, and to enable the fluid to cool. The hydraulic reservoir tank is connected to the structure using four brackets. The general components of the hydraulic reservoir tank are shown in Figure 4.1.

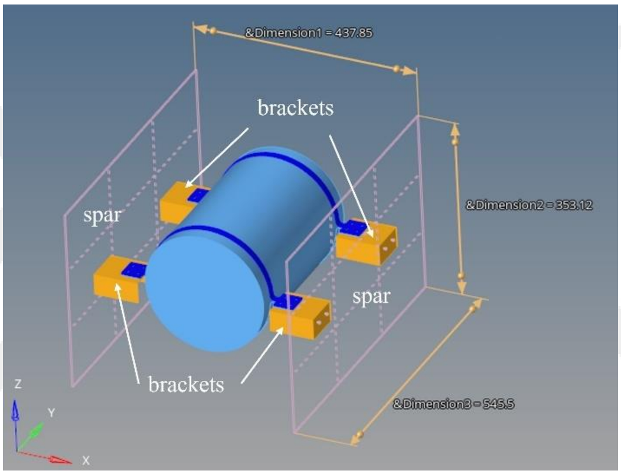

Figure 4.1 The general component of the hydraulic reservoir tank system

There is a hydraulic pump in the connection area of the hydraulic reservoir tank system to the aircraft structures. The hydraulic reservoir tank system is affected by the operating frequency range of the hydraulic pump, and the natural frequency values of the reservoir and connection brackets should be examined. The angular rotation speed of the hydraulic pump is assumed to be 3000 rpm. Thus, the target natural frequency value is 50Hz, and with the analysis studies, it is expected that the hydraulic reservoir tank system will meet the target frequency and the target fatigue life of 2000 flight cycles. PSD's exposure duration was determined to be 4 hours.

Structural random-vibration fatigue evaluation of the hydraulic reservoir tank system components with modal stress approach (Yeşilçimen & Kıral, 2022) is examined in this thesis, and the methodologies employed are outlined in Figure 4.2.

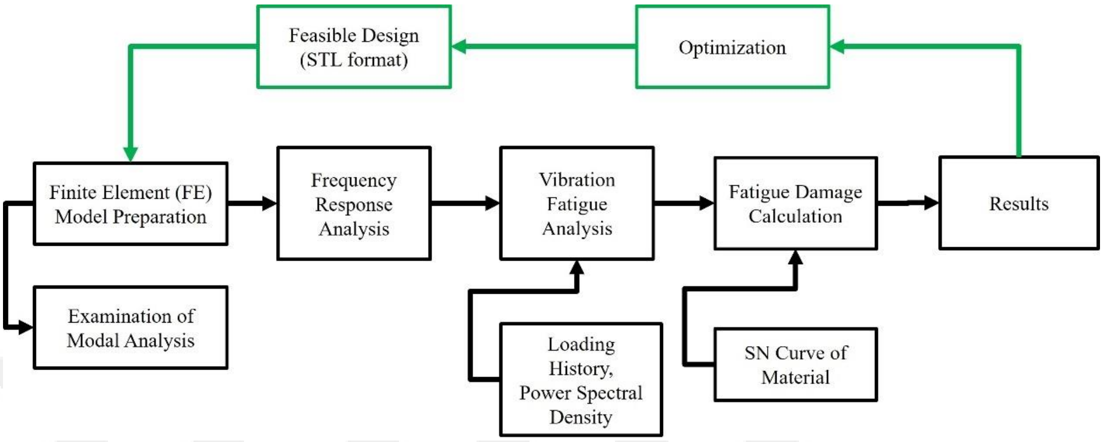

Figure 4.2 Methodology (Yeşilçimen & Kıral, 2022)

4.1 Finite Element (FE) Model Preparation

The FE model and analysis of hydraulic reservoir system brackets are carried out using Altair HyperMesh software. The linear quadrilateral plate elements of type CQUAD4 and linear triangular plate elements of type CTRIA3 are employed in the FE model. These plate elements feature six degrees of freedom per node formulation. The model has a total of 42600 elements and 37086 nodes. RBE2 rigid elements for fasteners are defined. The mesh model of tank geometry is created to account for inertial effects and stiffness. For modeling the overall tank mass, the concentrated mass element type of CONM2 is employed. Figure 4.3 illustrates the bracket's FE model in detail.

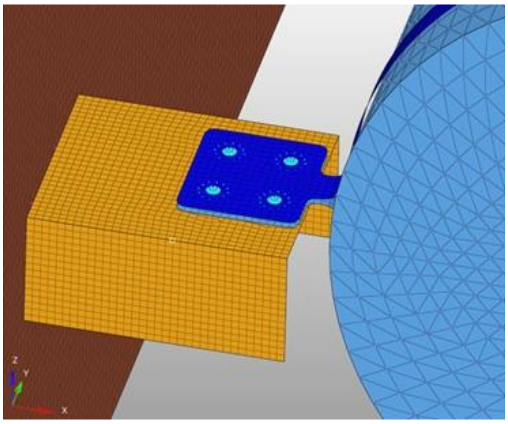

Figure 4.3 Finite element model of brackets

The structure's boundary conditions are restricted by the x and z axes of the nodes at the front-rear edges of spars, as well as the x and y axes of the nodes at the up-down edges of spars in Figure 4.4.

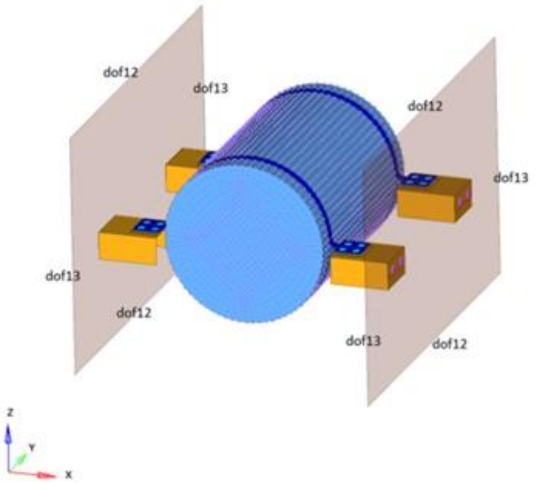

Figure 4.4 Boundary conditions

4.2 Materials Information in General

The materials used in the aerospace industry are classified as metallic or non-metallic. Metallic materials include aluminum, titanium, nickel, magnesium, and their alloys, and steel. Non-metal materials, on the other hand, are composite materials that continue to evolve.

Materials of the hydraulic reservoir system brackets and connected spars are chosen Aluminum and Titanium material respectively. The following headings describe the materials that will be used in the design of the components as well as their mechanical properties.

4.2.1 Aluminum and Its Alloys

Aluminum and aluminum-based alloys are widely used in the aircraft industry due to their high corrosion resistance and high specific strength. Aluminum UTS400 material mechanical properties and SN curve parameters are obtained from nCode Materials Manager Library, and then used as input in Altair HyperMesh. These mechanical properties are listed in Table 4.1, and the material's SN curve is depicted in Figure 4.5.

Table 4.1 Mechanical properties of aluminum UTS400 material (*nCode 11.0: Material Library Documentation.*, 2022)

Elastic Modulus	7.0e4 MPa
Poisson Ratio	0.33
Yield Strength	307.692 MPa
Ultimate Tensile Strength	400 MPa
Stress Range Intercept	947 MPa
First Fatigue Strength Exponent	-0.07606
Fatigue Transition Point	5E8 Cycles

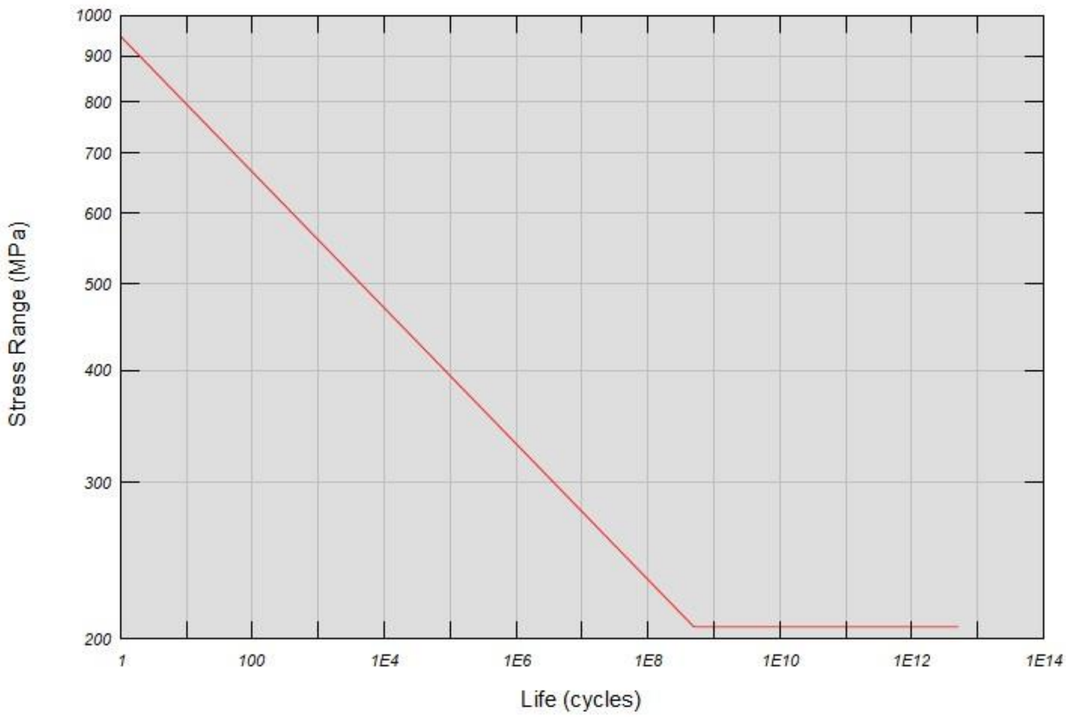

Figure 4.5 SN curve of aluminum UTS400 material (*nCode 11.0: Material Library Documentation.*, 2022)

4.2.2 Titanium and Its Alloys

Titanium and its alloys are noted for their thermal strength, light weight, and corrosion resistance. Due to this reason, it is used in the aircraft industry, the manufacture of firearms in the war industry, and in the alloying of many industrial materials it also acts a significant role. Titanium UTS500 material mechanical properties and SN curve parameters are obtained from nCode Materials Manager Library, and then used as input in Altair HyperMesh. These mechanical properties are listed in Table 4.2, and the material's SN curve is depicted in Figure 4.6.

Table 4.2 Mechanical properties of titanium UTS500 material (*nCode 11.0: Material Library Documentation.*, 2022)

Elastic Modulus	1.1E5 MPa
Poisson Ratio	0.4
Yield Strength	384.615 MPa
Ultimate Tensile Strength	500 MPa
Stress Range Intercept	2084 MPa
First Fatigue Strength Exponent	-0.1387
Fatigue Transition Point	1E6 Cycles

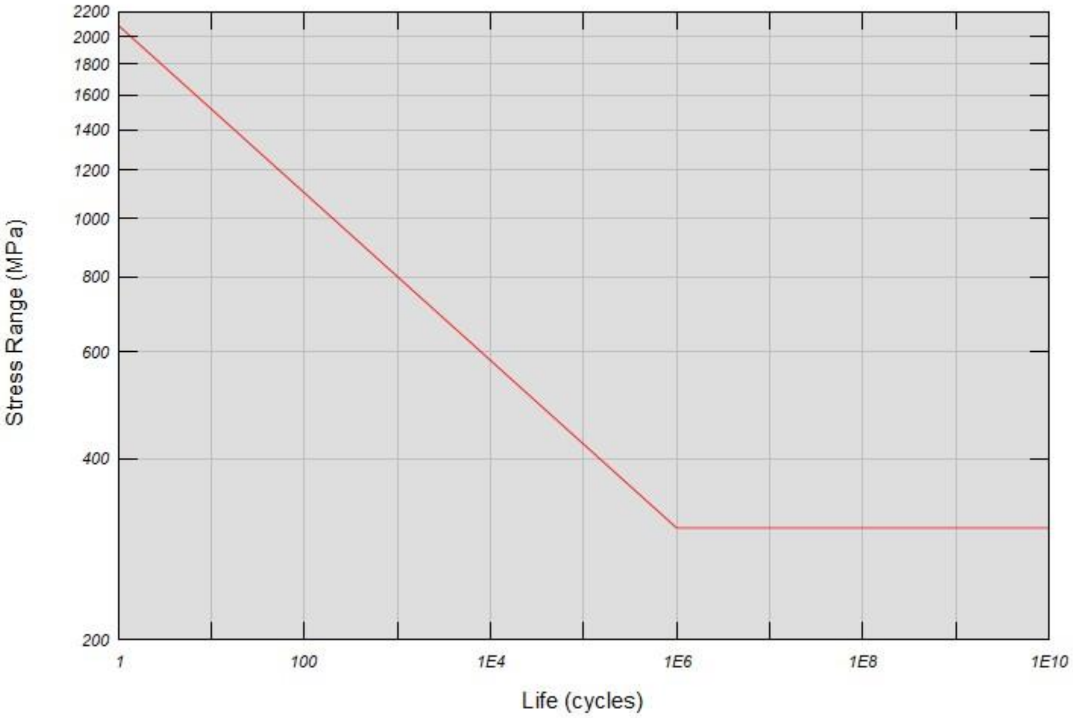

Figure 4.6 SN curve of titanium UTS500 material (*nCode 11.0: Material Library Documentation.*, 2022)

4.3 Modal Analysis

The purpose of modal analysis is to evaluate the dynamic behavior of the system and to determine the fundamental free vibration frequencies and mode shapes of the system.

In OptiStruct, normal mode analysis may be conducted employing either the Lanczos or the AMSES optimization algorithms. The EIGRL and EIGRA card definitions are available for the Lanczos and AMSES (automated multi-level sub-structuring eigenvalue solution) algorithms, respectively. The Lanczos approach has the benefit of precisely calculating the eigenvalues and related mode shapes. This approach is effective for computations involving a small number of modes and the entire geometry of each mode. For complex problems requiring hundreds of modes and millions of degrees of freedom, the disadvantage of the Lanczos technique is that it is slow. For these sorts of problems, it might easily take more than a day for analysis time. The AMSES technique must be utilized in these circumstances (*Altair 2021 Student Edition: OptiStruct.,* 2022).

In this study, the modal analysis of the hydraulic reservoir tank system is evaluated in the range of 0 to 2000 Hz using the Lanczos method.

4.4 Frequency Response Analysis

To begin with the vibration fatigue analysis under random loads, the transfer function for a structural model must be established/derived. The output and input of a system are affiliated with each other by the transfer function. The frequency transfer function of a structure is obtained from the structural response per unit input at each frequency of interest.

The frequency response analysis based on the modal stress approach was carried out to obtain the frequency transfer function of the structure. A sinusoidal loading with an acceleration amplitude of 1g mm/s^2 is employed to the structure as a base excitation, and output stresses are obtained at each frequency increment up to 2000 Hz in this study. In the entire frequency range, the structural damping is defined as 2%.

4.5 Vibration Fatigue Analysis

The inputs of the random-vibration fatigue analysis are transfer functions of the structure under acceleration excitation of 1g derived from frequency response analysis and the excitation loading that is PSD curve in the frequency domain. The y-axis of the PSD curve is in G^2/Hz and it is called the acceleration spectral density. By using the random response analysis, the stress value of each frequency is multiplied with the value of the acceleration spectral density of the relevant frequency. The output of the random response analysis is the PSD of stress, and it is used for determining the number of cycles to failure (*Altair 2021 Student Edition: OptiStruct.*, 2022).

In this study, random response analyses were conducted by employing an excitation on the x, y, and z axes separately. The structure is driven by the same PSD data at all three axes. The general exposure PSD curve is taken from a military standard (MIL-STD 810F, 2000) and is demonstrated in Figure 4.7 and Table 4.3. The PSD data, whose frequency range is between 15 and 2000Hz, depicts a zero-averaged stationary Gaussian process. The range of frequencies of interest has been determined for eigenvalue analysis, and it is intended that more than one structural mode will be contained. The average value of the PSD employed in the analysis is 4.02 g RMS acceleration.

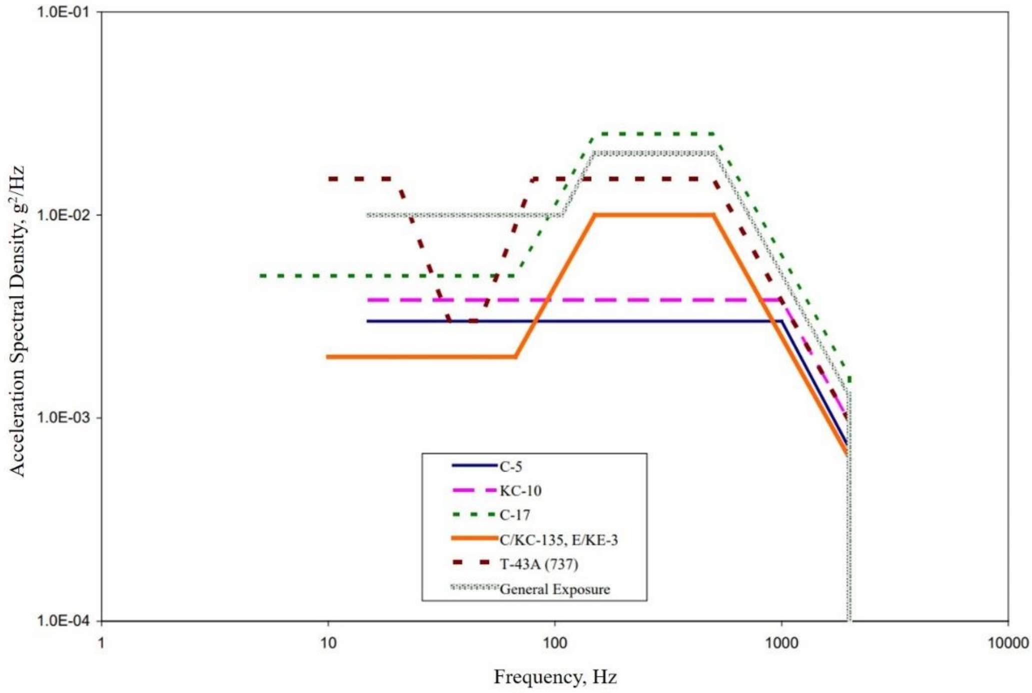

Figure 4.7 Input PSD for jet aircraft vibration exposure from MIL-STD 810G (MIL-STD 810F, 2000)

Table 4.3 Break points for input PSD from MIL-STD 810G (MIL-STD 810F, 2000)

C-5			KC-10			KC-135, E-3			C-17		
Hz	g^2/Hz	dB/Oct	Hz	g^2/Hz	dB/Oct	Hz	g^2/Hz	dB/Oct	Hz	g^2/Hz	dB/Oct
15	0.003		15	0.0038		10	0.002		5	0.005	
1000	0.003		1000	0.0038		67	0.002		67	0.005	
		-6			-6			6			6
2000	7.5E-4		2000	9.5E-4		150	0.01		150	0.025	
rms = 2.11 g			rms = 2.38 g			500	0.01		500	0.025	
								-6			-6
						2000	6.3E-4		2000	1.6E-3	
						rms = 2.80 g			rms = 4.43 g		

T-43A (737)			General Exposure			
Hz	g^2/Hz	dB/Oct	Hz	g^2/Hz	dB/Oct	Note: C-17 levels apply to the primary cargo floor. Levels for items carried on the aft ramp are higher.
10	0.015		15	0.01		
20	0.015		106	0.01		
		-9			6	
34	0.003		150	0.02		
47	0.003		500	0.02		
		9			-6	
80	0.015		2000	1.3E-3		
500	0.015		rms = 4.02 g			
		-6				
2000	9.5E-4					
rms = 3.54 g						

After that, the fatigue parameters of the material are defined for the stress life method. It was mentioned before that aluminum and titanium materials were chosen for the hydraulic reservoir system brackets and connected spar, respectively. In this study, since the fatigue life of the brackets was solely examined, the fatigue parameters of the material were defined for those components, and also outputs for vibration fatigue analysis were demanded. These parameters are taken from the nCode material library.

4.6 Fatigue Damage Calculation

Stress levels were obtained from the analysis of random response, which is the result of multiplying the transfer function with PSD. The modified Palmgren-Miner rule is employed to determine the accumulation of damage in the frequency domain. In this study, the cumulative damage of the hydraulic reservoir system brackets was calculated by using the density function of probability of the Dirlik approach in the frequency domain.

4.7 Structural Optimization

The process of selecting the appropriate material distribution is referred to as structural optimization. The aim of that is to find a design that can safely carry or withstand the imposed loading conditions within a volume domain. It is also defined as the best selection in general terms. Manufacturing and eventual use limitations must also be considered during the structural optimization process (Querin & Victoria, 2017).

In optimization problems, there is an output variable with a varying value according to the input variables. The process of achieving the output variable's minimum or maximum value is defined as optimization. There are three distinct sorts of optimization approaches under structural optimization: size, shape, and topology. Three different models used in structural optimization are shown in Figure 4.8.

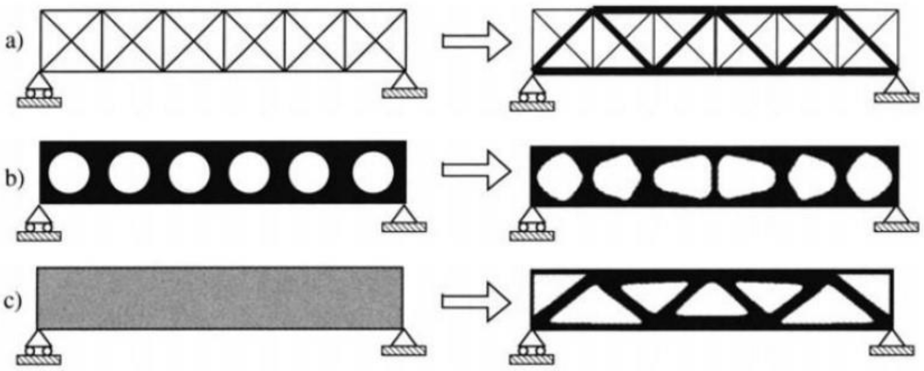

Figure 4.8 Three different models of structural optimization (a) size, (b) shape, (c) topology optimization (Bendsoe, 2003)

In size optimization, the components to be employed in the structure, such as cantilever beams, are the predefined design space. Considering the optimization results, detailed design parameters such as the cross-sectional size and area of the beam are acquired. They are shown in Figure 4.9 (a) and (b).

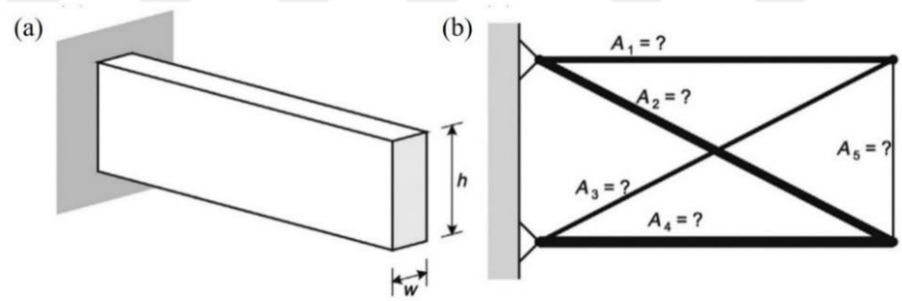

Figure 4.9 Structures where size optimization could be implemented: (a) cross-sectional measures of cantilever beam, (b) cross-sectional areas of bars in truss structure (Querin & Victoria, 2017)

In shape optimization, some sections' form of a structural design's boundary is unknown. The analysis result extracts the optimization boundaries or forms that might be expressed by equations or portrayed by a point cloud, Figure 4.10.

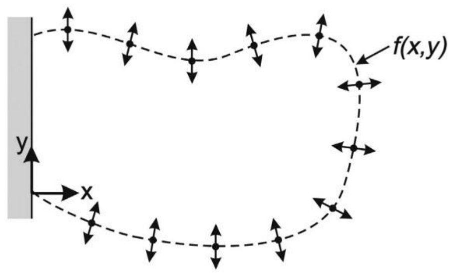

Figure 4.10 Design space that can be expressed by boundary's equation or control points moving perpendicular to boundary (Querin & Victoria, 2017)

The most general type of structural optimization is topology optimization. By allowing the design variables to have a value between the size of the minimum and the maximum, topology optimization is accomplished. It can be possible that some trusses are removed in truss structures (Figure 4.11) and the number and form of the holes are determined for continuum structures when the design variables have a zero value, for instance.

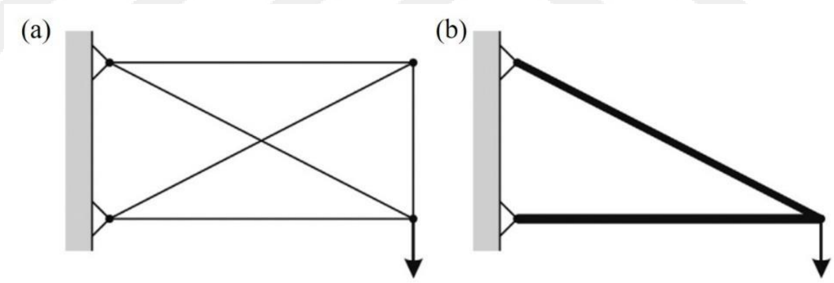

Figure 4.11 Truss structure's optimization: (a) topology design space; (b) optimized design that proposed to decrease the number of truss (Querin & Victoria, 2017)

While optimization processes can also be done by hand calculations, nowadays many conveniences are provided with the help of computer programs. Optimization problems involving more than one variable are easier to solve with computer-aided programs.

Within the scope of this thesis, optimization problems are performed by Altair HyperWorks software with the OptiStruct solver. It is an attested, contemporary structural solver that offers solutions that are thorough, precise, and scalable for linear and nonlinear studies across a variety of disciplines. It has an interface that specializes in creating and optimizing detailed “mesh” models. Since the controls on the model can be applied directly through the "mesh", it is suitable for topological optimization. In today's industry, optimization studies and various software for it are supported globally to optimize the design and increase the structural performance.

There are three basic terms in optimization: objective function, design variable, and design constraint. An objective function is a function that converts into a value that may describe the comparison of different designs and the degree of quality of the design. This function expresses the minimization or maximization. An optimal design is one in which the objective function is minimized or maximized. Design variables are parameters that must be altered for the design to achieve its objective. Design constraints are the limitations that the design must fulfill in an optimization problem. The objective function's mathematical formulation is as follows:

$$
\begin{gathered}
Minimize\ f(x) = f(x_1, x_2, x_3, \dots, x_n) \\
g_j(x) \leq 0\ where\ j = 0,1, \dots, m \\
x_i^L \leq x_i \leq x_i^U\ where\ i = 0,1, \dots, n
\end{gathered}
\tag{4.1}
$$

where x is a vector of design variables with lower (L) and upper (U) bounds, g(x) are constraint functions, and f(x) is the objective function (*Altair 2021 Student Edition: OptiStruct.*, 2022). An ideal design is obtained depending on a user-defined design space, performance objectives, and manufacturing restrictions. In this thesis, optimization techniques are used to obtain the optimal design of the hydraulic reservoir system components according to design limitations and objective function.

4.7.1 Topology Optimization

Topology optimization, a mathematical technique, constructs, within a particular package space, an optimal form and material distribution for a structure. In topology optimization, the density method is employed. The design parameter in this method is each element's density, which has a value ranging from 0 to 1. The element density is set to zero if a decrease in the design volume is required. It is presumed that the density has a direct proportionality with the material's stiffness. According to what we know about conventional materials, this material formulation provides consistency. For instance, titanium, which has a higher density than aluminum, has a higher stiffness.

OptiStruct employs the SIMP (Solid Isotropic Material with Penalty) method. Because a density of pseudo material is considered as the design parameter, it is also referred to as the density technique. The stiffness-density association is expressed by a penalization factor in the SIMP approach. This approach seeks to determine if a material is distributed as a solid or a void by using a value of 0 or 1 (*Altair 2021 Student Edition: OptiStruct.*, 2022).

$$\widetilde{K}(\rho) = \rho^{p} K \tag{4.2}$$

Where, $\check{K}$ and K are the stiffness matrices of the penalized and original, respectively. By combining the density ρ, and the factor of penalization p, a relation between the rigidities is established.

4.7.2 Size/Parameter Optimization

When optimizing for size or parameter, component characteristics like thickness, beam sections, and stiffness can be improved. A function among the design variables is implemented in optimization to achieve an optimum design. The simplest relationship between design variables and properties is the linear combination of design variables (*Altair 2021 Student Edition: OptiStruct.*, 2022).

$$p = C_0 + \sum d_i C_i \tag{4.3}$$

Where, p is the property to be optimized, C_i is the linear factors associated to the design variable d_i.

CHAPTER 5
ANALYSIS RESULTS

The FE model of the hydraulic reservoir tank system is modeled using Altair HyperMesh software and then analyses of modal, frequency response, fatigue, and optimization are performed using the OptiStruct solver.

5.1 The Existing Hydraulic Reservoir Tank System

Figure 5.1 shows the thickness map of the existing hydraulic reservoir tank system components. The current brackets and spars have 2mm and 3mm thickness values, respectively.

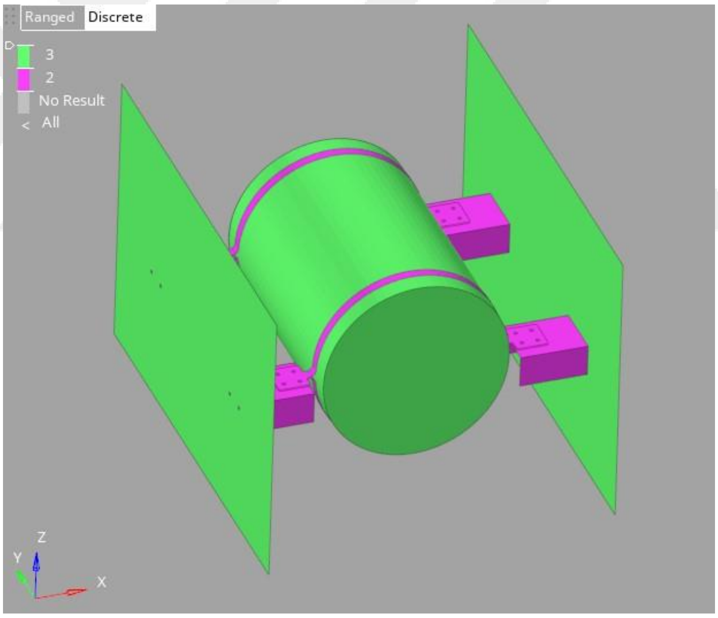

Figure 5.1 Thickness map [mm] of the existing hydraulic reservoir tank system components

5.1.1 Modal Analysis of the Existing Hydraulic Reservoir Tank System

A technique for determining a structure's vibration shapes and associated frequencies is modal analysis, commonly referred to as eigenvalue extraction. Stimulating the structure at its natural frequencies indicates that the structure is in a state of resonance. The amplitude of the system's response reaches its maximum value in the event of resonance and thus triggers destructive damage. Consequently, it is preferable to operate the system at a frequency higher than these excitations in order to eliminate conflicts with the structure's inherent frequencies.

The modal analysis of the existing hydraulic reservoir tank system is restricted by the x, y, and z axes of the nodes at the front-rear edges of spars as well as the x and y axes of the nodes at the up-down edges. The same frequency range is defined in the modal analysis since the PSD data that will be employed for the random-vibration fatigue evaluation is up to 2000Hz. Utilizing the Lanczos eigenvalue extraction technique, analysis was carried out in the OptiStruct solver. In figures between Figure 5.2 and Figure 5.6, the system's mode shapes, lower than 50Hz, are demonstrated.

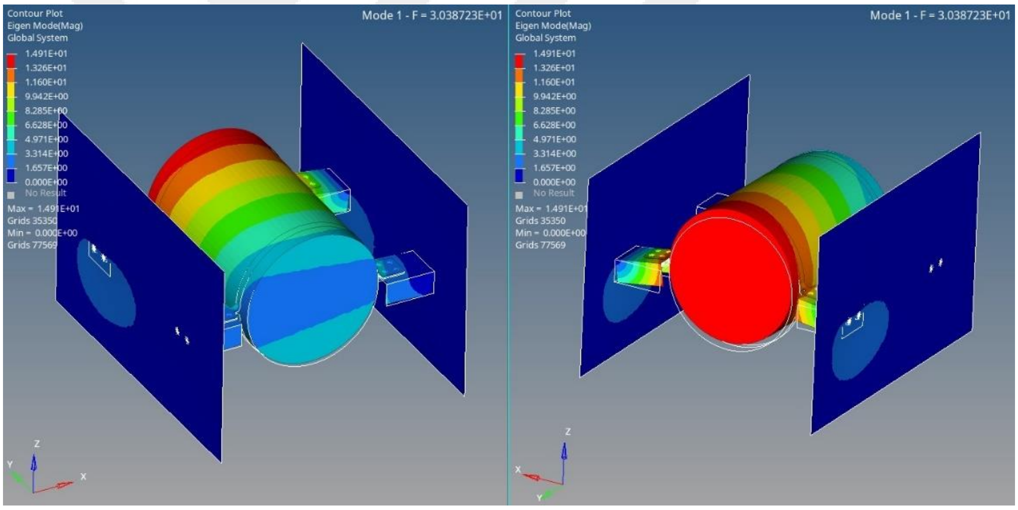

Figure 5.2 The first mode shape of the existing hydraulic reservoir tank system (Mode-1 f=30.38 Hz)

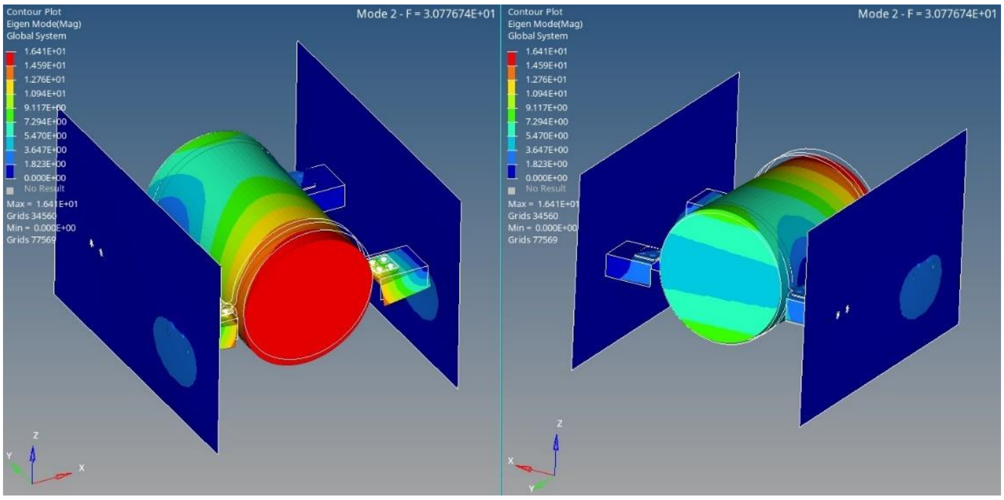

Figure 5.3 The second mode shape of the existing hydraulic reservoir tank system (Mode-2 f=30.77 Hz)

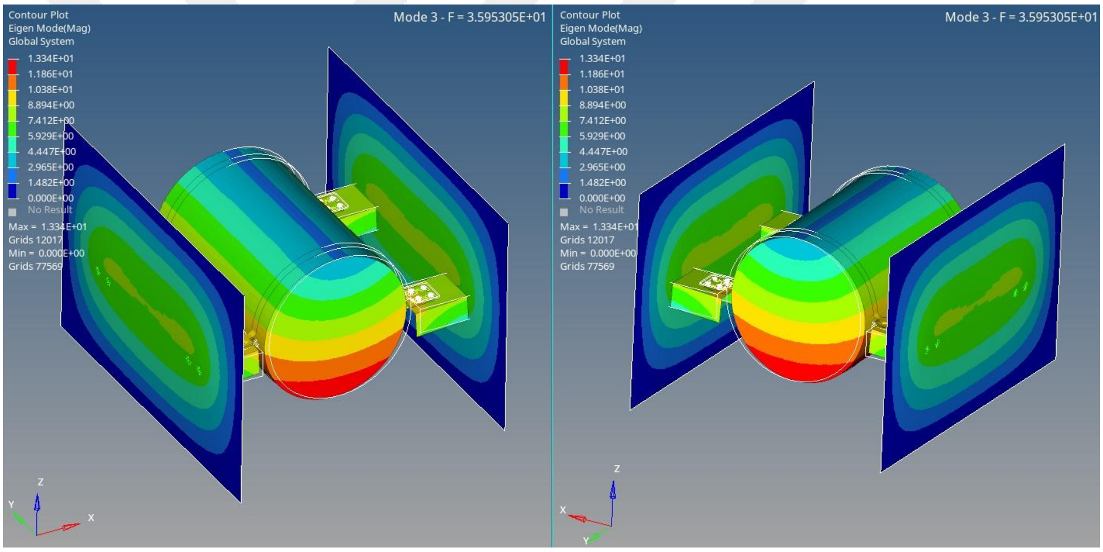

Figure 5.4 The third mode shape of the existing hydraulic reservoir tank system (Mode-3 f=35.95 Hz)

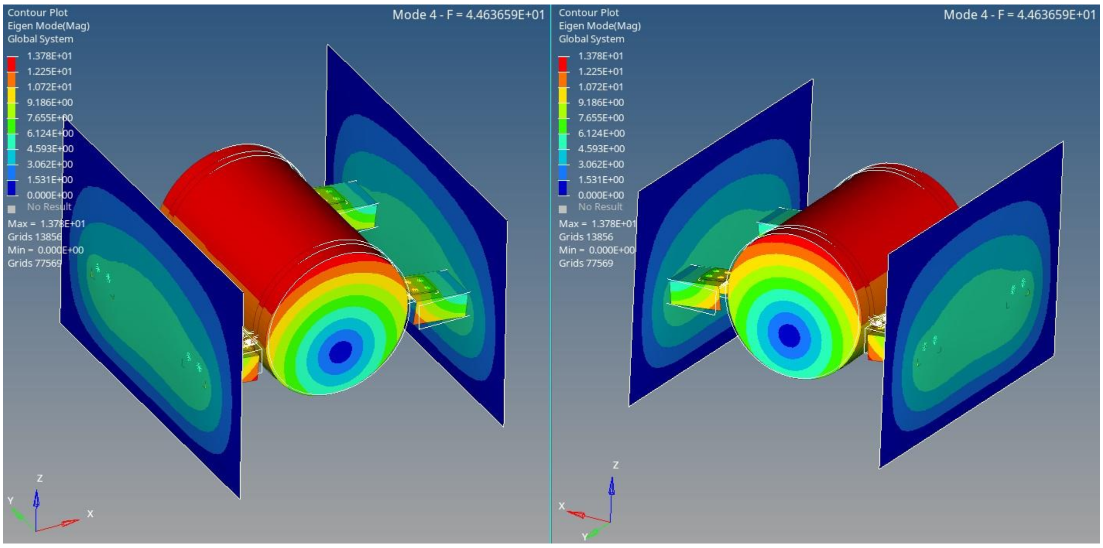

Figure 5.5 The fourth mode shape of the existing hydraulic reservoir tank system (Mode-4 f=44.64 Hz)

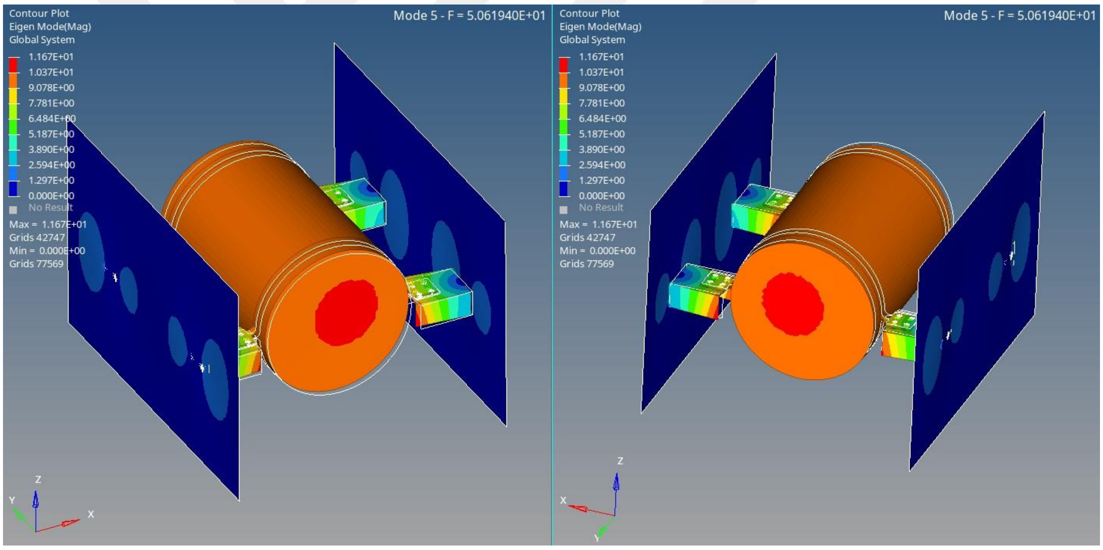

Figure 5.6 The fifth mode shape of the existing hydraulic reservoir tank system (Mode-5 f=50.62 Hz)

A numerical modal analysis was performed to determine the natural frequencies of the hydraulic reservoir tank system. Until 1000Hz, the natural frequencies are indicated in Table 5.1.

Table 5.1 The existing hydraulic reservoir tank system's natural frequencies until 1000 Hz

Mode	Frequency [Hz]	Mode	Frequency [Hz]	Mode	Frequency [Hz]
1	30.39	24	462.96	47	769.70
2	30.78	25	499.53	48	776.37
3	35.95	26	505.98	49	780.75
4	44.64	27	521.87	50	783.61
5	50.62	28	522.26	51	792.36
6	70.06	29	556.19	52	794.97
7	209.41	30	559.64	53	814.35
8	211.63	31	604.55	54	815.29
9	222.13	32	607.86	55	845.99
10	237.59	33	619.41	56	850.22
11	272.76	34	619.53	57	850.66
12	273.44	35	649.58	58	880.13
13	334.82	36	651.79	59	883.58
14	337.90	37	691.43	60	890.01
15	382.90	38	692.08	61	962.55
16	394.49	39	694.95	62	966.66
17	402.53	40	704.23	63	966.94
18	408.00	41	711.24	64	970.60
19	437.21	42	726.07	65	973.78
20	437.31	43	733.84	66	980.53
21	443.16	44	741.59	67	993.88
22	443.47	45	750.86	68	997.16
23	462.49	46	761.12	69	1016.78

When the modal participation factor ratios of the existing design are examined (Table 5.2), it is observed that the z-axis at the first and second modes, the x-axis at the third and fourth modes, and the y axis at the fifth mode are dominant. This means that stress results at the dominant axis are higher than those at other axes.

Table 5.2 Modal participation factors ratios of the existing hydraulic reservoir tank system from modal analysis up to 1000 Hz

Mode	Frequency [Hz]	X-Trans	Y-Trans	Z-Trans	Mode	Frequency [Hz]	X-Trans	Y-Trans	Z-Trans	Mode	Frequency [Hz]	X-Trans	Y-Trans	Z-Trans
1	30.39	1%	1%	100%	24	462.96	2%	0%	1%	47	769.70	8%	0%	0%
2	30.78	1%	2%	59%	25	499.53	0%	0%	0%	48	776.38	1%	0%	1%
3	35.95	100%	0%	3%	26	505.98	9%	0%	0%	49	780.76	5%	0%	0%
4	44.64	55%	0%	3%	27	521.89	0%	2%	0%	50	783.61	1%	0%	1%
5	50.63	0%	100%	0%	28	522.28	0%	5%	0%	51	792.36	0%	0%	3%
6	70.06	0%	5%	0%	29	556.19	0%	0%	0%	52	794.97	2%	0%	1%
7	209.41	0%	0%	1%	30	559.64	0%	0%	0%	53	814.35	0%	0%	0%
8	211.63	0%	0%	4%	31	604.55	1%	0%	1%	54	815.29	0%	0%	0%
9	222.13	10%	0%	0%	32	607.87	3%	0%	0%	55	845.99	0%	0%	0%
10	237.59	0%	2%	0%	33	619.41	0%	0%	0%	56	850.22	1%	0%	0%
11	272.76	0%	0%	4%	34	619.53	0%	1%	0%	57	850.66	1%	0%	0%
12	273.44	0%	0%	1%	35	649.58	0%	0%	0%	58	880.13	0%	0%	0%
13	334.82	0%	0%	0%	36	651.79	2%	0%	0%	59	883.58	3%	0%	2%
14	337.90	0%	0%	0%	37	691.43	0%	0%	0%	60	890.01	7%	0%	1%
15	382.90	0%	0%	0%	38	692.08	0%	1%	0%	61	962.55	0%	0%	1%
16	394.49	0%	0%	0%	39	694.95	0%	0%	0%	62	966.66	0%	1%	0%
17	402.53	3%	0%	3%	40	704.23	0%	0%	0%	63	966.94	0%	1%	1%
18	408.01	22%	0%	0%	41	711.24	0%	0%	0%	64	970.60	1%	0%	1%
19	437.21	0%	0%	0%	42	726.07	0%	0%	0%	65	973.80	1%	1%	0%
20	437.31	2%	0%	0%	43	733.84	0%	0%	0%	66	980.54	1%	1%	0%
21	443.16	0%	0%	0%	44	741.59	0%	0%	0%	67	993.89	0%	0%	2%
22	443.47	1%	0%	0%	45	750.86	0%	0%	0%	68	997.17	1%	0%	0%
23	462.49	4%	0%	1%	46	761.12	1%	0%	0%	69	1016.78	1%	0%	4%

5.1.2 Frequency Response Analysis of the Existing Hydraulic Reservoir Tank System under Unit Acceleration

The transfer function between the inputs and outputs required for fatigue calculations are obtained using frequency response analysis. The input and output in this study are acceleration and stress, respectively. The analysis of frequency response under 1g mm/s^2 unit acceleration is performed after the modal analysis of the existing hydraulic reservoir tank system. The ratio of structural damping is considered to be 2%.

The structure is subjected to a sinusoidally fluctuating 1g unit loading excitation, which is defined separately for each axis. The stress response under 1g sinusoidal excitation in the z-axis is demonstrated in Figure 5.7.

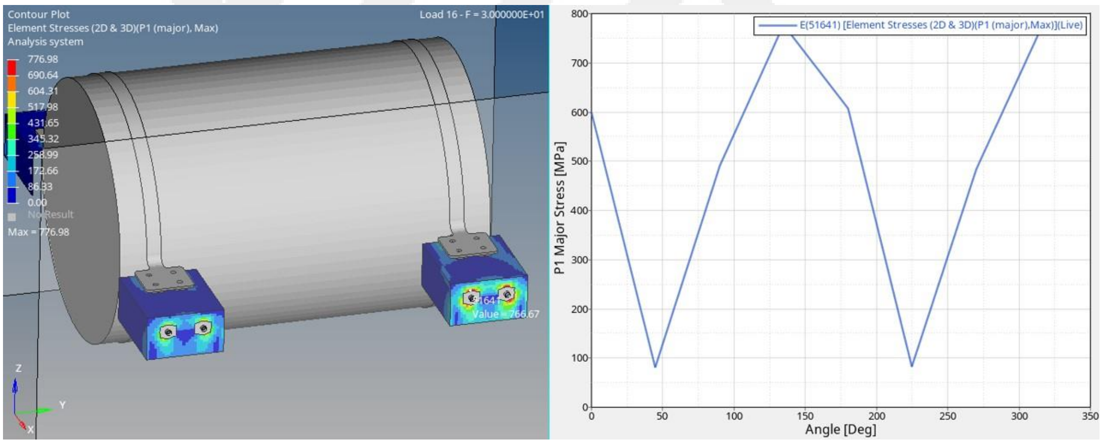

Figure 5.7 Stress response at 30 Hz under 1g sinusoidal excitation in the z-axis for frequency response analysis

From the numerical analysis, the transfer functions of the hydraulic reservoir tank system are extracted at each node. The frequency increment is set to 1 Hz and the stress values at each frequency are written to the output file. Figures from Figure 5.8 to Figure 5.10, respectively, represent the stress plot versus frequency obtained from the frequency response analysis under unit acceleration loading applied separately on the x, y, and z axes.

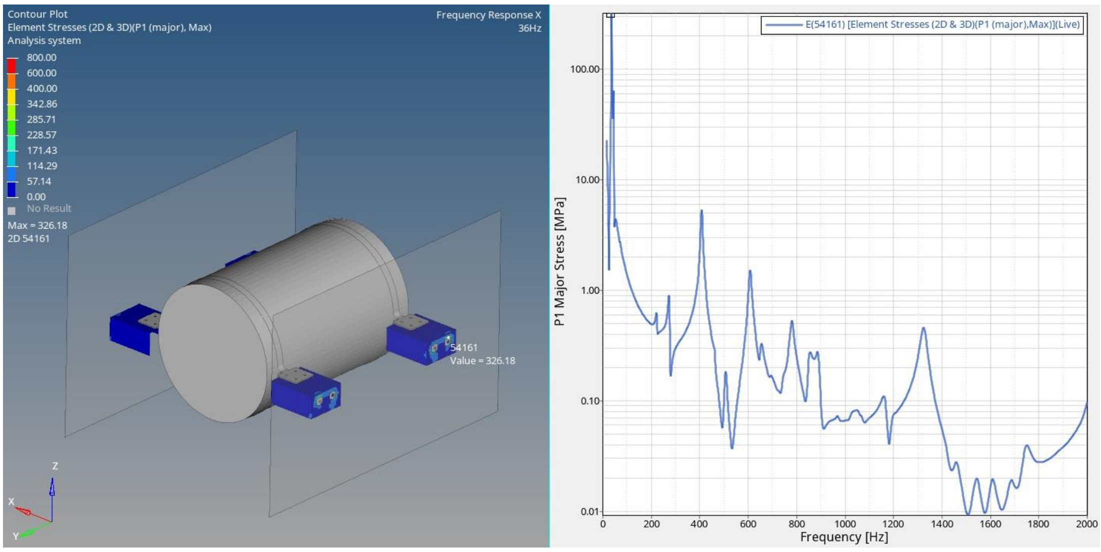

Figure 5.8 Maximum principal stress plot of the existing design versus frequency obtained from the frequency response analysis under x axis unit loading (logarithmic scale)

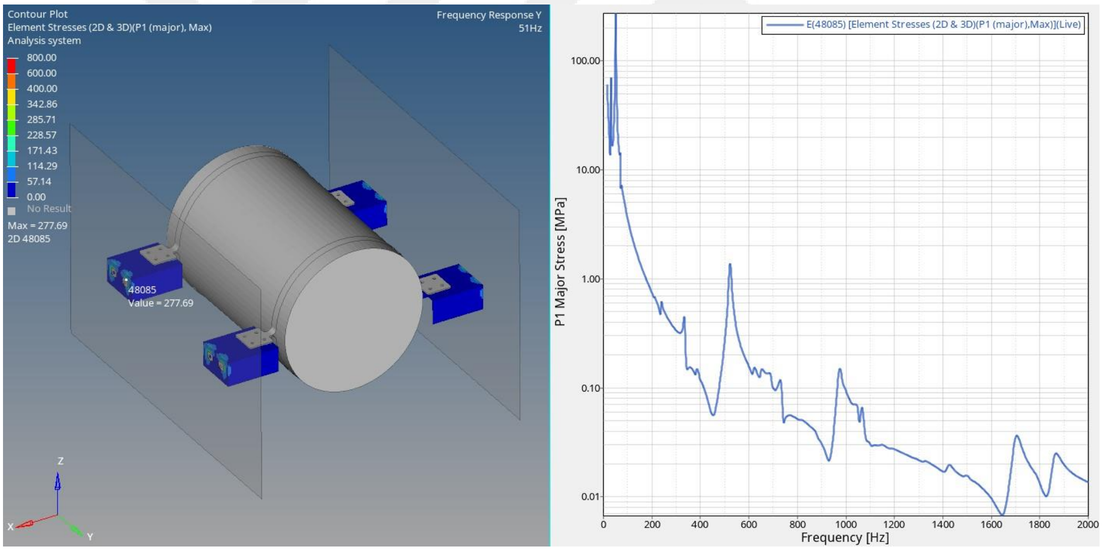

Figure 5.9 Maximum principal stress plot of the existing design versus frequency obtained from the frequency response analysis under y axis unit loading (logarithmic scale)

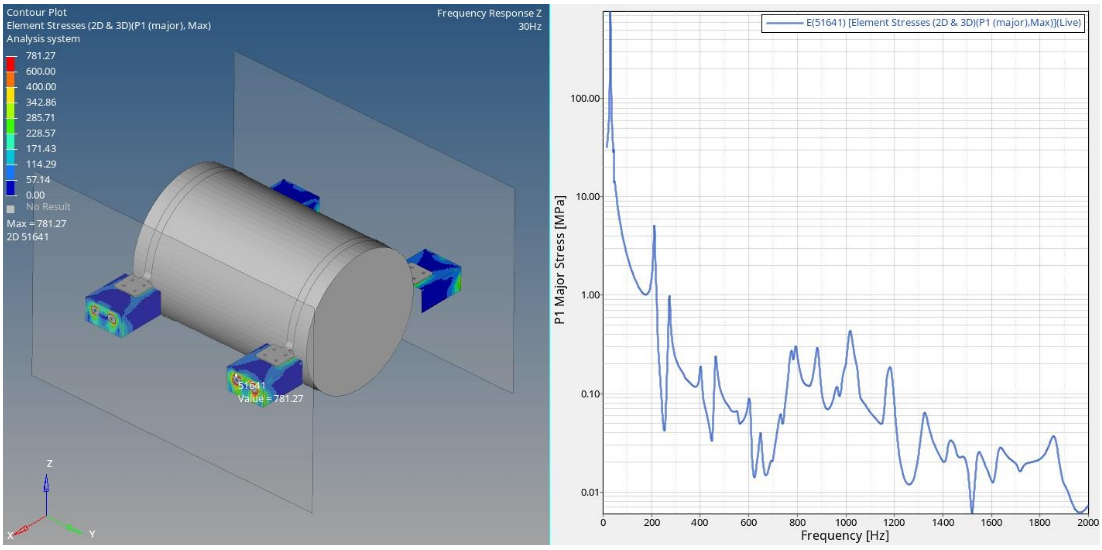

Figure 5.10 Maximum principal stress plot of the existing design versus frequency obtained from the frequency response analysis under z axis unit loading (logarithmic scale)

5.1.3 Random Response Analysis of the Existing Hydraulic Reservoir Tank System under Unit Acceleration

The inputs for random response analysis are the transfer functions derived from frequency response analysis and the PSD, which is taken from military standards.

The RANDPS (random case control) definition is employed in Altair HyperMesh to define a load case of random response analysis. It combines the frequency response analyses of the x, y, and z directions with PSD excitation. The maximum RMS stress value is 119.03 MPa on the system brackets obtained from the random response analysis and it is illustrated in Figure 5.11. The frequency-dependent PSD stress curve in element number 48106, where the maximum RMS stress occurs, is depicted in Figure 5.12.

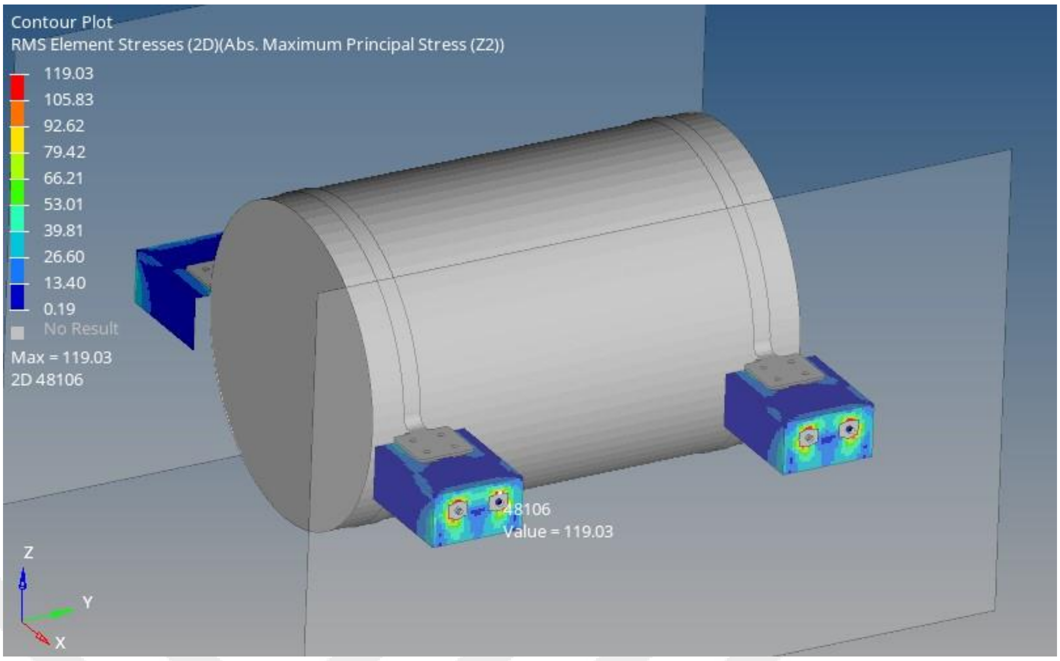

Figure 5.11 The maximum RMS stress value on the existing system brackets obtained from the random response analysis

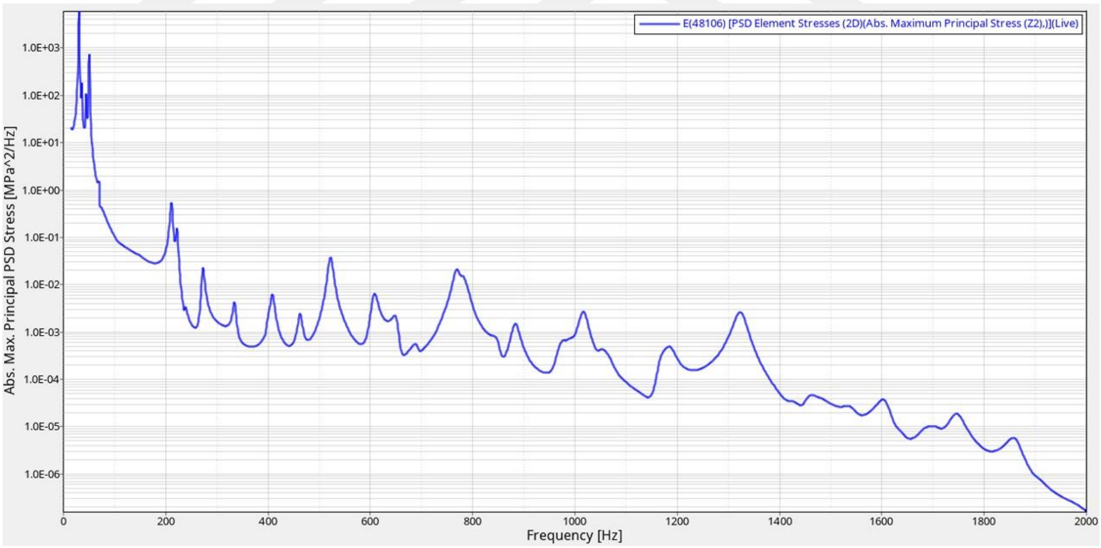

Figure 5.12 The frequency-dependent PSD stress curve in element number 48106

5.1.4 Random-Vibration Fatigue Analysis of the Existing Hydraulic Reservoir Tank System under Unit Acceleration

After the frequency-dependent PSD stress curves are obtained from random response analysis, Dirlik's approach is used for assessing the random-vibration fatigue life of the existing hydraulic reservoir tank system. In the numerical model, the effects of mean stress on fatigue are not taken into account. The absolute maximum principal stress value is preferred as the input of the analysis, and the total fatigue life is predicted from the stress ranges calculated by considering these stresses. The minimum fatigue life of the existing hydraulic reservoir tank system brackets is calculated as 242 cycles, as depicted in Figure 5.13.

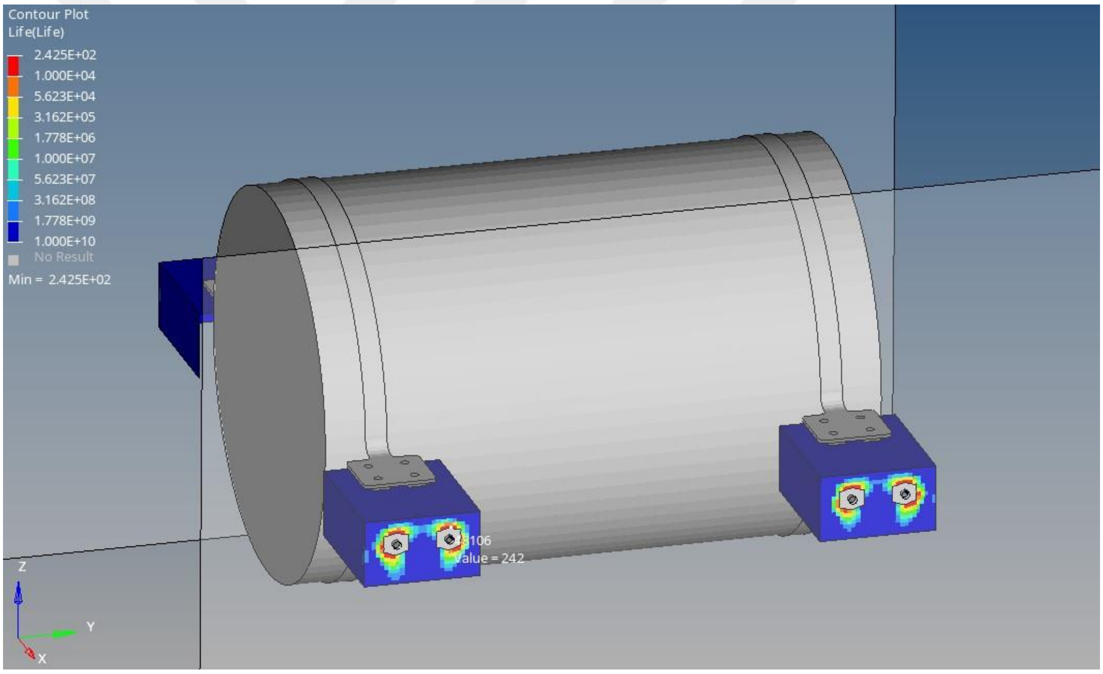

Figure 5.13 Fatigue life of the hydraulic reservoir tank system brackets

The rainflow cycle count history might be extracted from the analysis. Its extension file is the RNF file, as shown in Table 5.3. It contains stress amplitudes, the probability of the corresponding stress amplitude occurring, the number of cycles of the specific stress amplitude, and the cumulative damage value of all cycles at the current stress amplitude. In the last row, total damage is given for the exposure duration of PSD.

The rainflow cycle count history of element number 48106 is demonstrated in Table 5.3. For a PSD exposure duration of 60 seconds, the total damage is 0.171833E-04. For a total exposure duration of 4 hours, total life could be calculated as 242 cycles.

Table 5.3 Fatigue damage result table of random response fatigue analysis in element number 48106 for 60 second exposure duration

```
                               Element 48106
-------------------------------------------------------------------------------------------
 Event 9 (1st of total 1 event): 99 stress amplitudes
-------------------------------------------------------------------------------------------
 DIRLIK
  Stress #  Stress amp.    Prob.     No. of cycles  Mean stress  Cor. stress amp.  Damage
       1  0.476122E+01  0.377791E+00  0.865238E+02  0.000000E+00  0.476122E+01  0.000000E+00
       2  0.142836E+02  0.332028E+00  0.760429E+02  0.000000E+00  0.142836E+02  0.000000E+00
 .
 .
 .
      30  0.280912E+03  0.168895E-02  0.386812E+00  0.000000E+00  0.280912E+03  0.128138E-06
      31  0.290434E+03  0.143907E-02  0.329585E+00  0.000000E+00  0.290434E+03  0.163116E-06
      32  0.299957E+03  0.121732E-02  0.278797E+00  0.000000E+00  0.299957E+03  0.203491E-06
      33  0.309479E+03  0.102233E-02  0.234140E+00  0.000000E+00  0.309479E+03  0.248991E-06
      34  0.319001E+03  0.852427E-03  0.195228E+00  0.000000E+00  0.319001E+03  0.299053E-06
      35  0.328524E+03  0.705691E-03  0.161621E+00  0.000000E+00  0.328524E+03  0.352811E-06
      36  0.338046E+03  0.580065E-03  0.132850E+00  0.000000E+00  0.338046E+03  0.409114E-06
      37  0.347569E+03  0.473431E-03  0.108428E+00  0.000000E+00  0.347569E+03  0.466566E-06
      38  0.357091E+03  0.383678E-03  0.878722E-01  0.000000E+00  0.357091E+03  0.523582E-06
      39  0.366614E+03  0.308760E-03  0.707139E-01  0.000000E+00  0.366614E+03  0.578468E-06
      40  0.376136E+03  0.246734E-03  0.565085E-01  0.000000E+00  0.376136E+03  0.629505E-06
 .
 .
 .
      97  0.918915E+03  0.378895E-12  0.867766E-10  0.000000E+00  0.918915E+03  0.453935E-10
      98  0.928437E+03  0.287529E-12  0.658515E-10  0.000000E+00  0.928437E+03  0.390010E-10
      99  0.937960E+03  0.218659E-12  0.500784E-10  0.000000E+00  0.937960E+03  0.335373E-10
===========================================================================================
          Total damage                              0.171833E-04
```

5.2 Optimization Studies of the Hydraulic Reservoir Tank System

According to the analysis results of the existing hydraulic reservoir tank system, the first natural frequency is lower than the target frequency value, and the fatigue life of the brackets is unsatisfactory. Optimization studies were performed for the hydraulic reservoir tank system's first natural frequency and fatigue life targets.

The first step in an optimization study is to define design space. In this section, the hydraulic reservoir tank system brackets and spars are assessed to obtain an optimum design.

5.2.1 Topology Optimization for Brackets

At first, topology optimization is performed for brackets. The ribs were added inside the brackets and then, it is separated into design and non-design regions. Figure 5.14 depicts the design space of the bracket design 1. The density of each element in the design region is defined as a design variable. Region of connection holes is defined as the non-design region and extracted from design variable component.

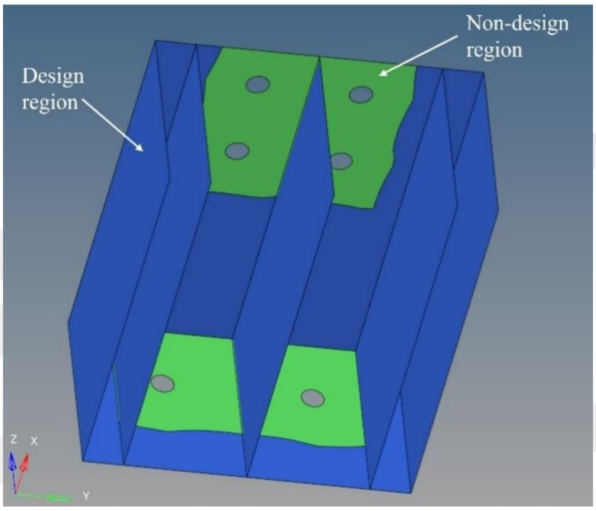

Figure 5.14 Design space of the bracket design 1

Volume fraction and the first natural frequency were defined as optimization responses. The natural frequency of the first normal mode was chosen as the topology lower bound constraint. The objective is to minimize volume fraction to identify locations for ribs in the designable region.

According to the current design, topology optimization yielded the optimal bracket design with reduced mass and higher frequency. The topology optimization result for bracket design 1 is illustrated in Figure 5.15.

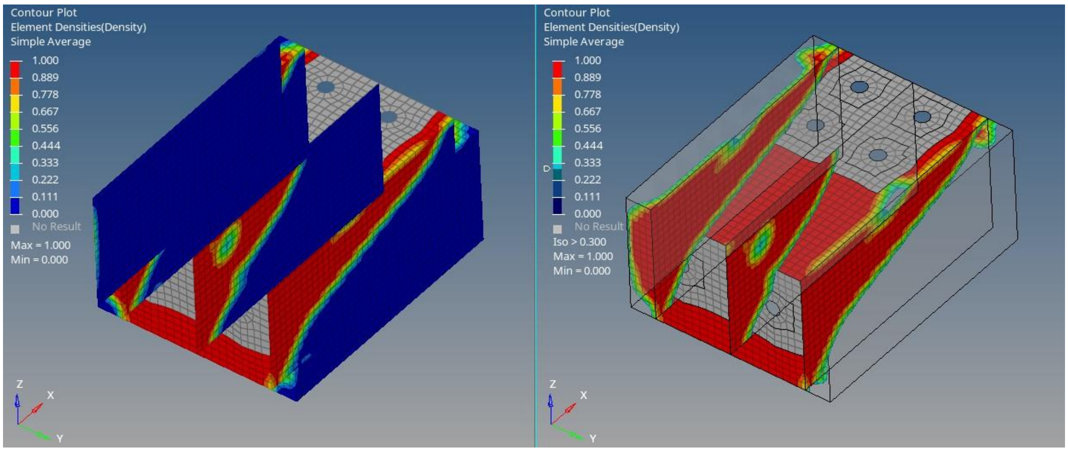

Figure 5.15 Topology optimization result for bracket design 1

The optimal design is exported in the form of an STL data format from HyperView. The FE model of bracket design 1 is illustrated in Figure 5.16. Modal and random-vibration fatigue analyses are repeated for the bracket design 1.

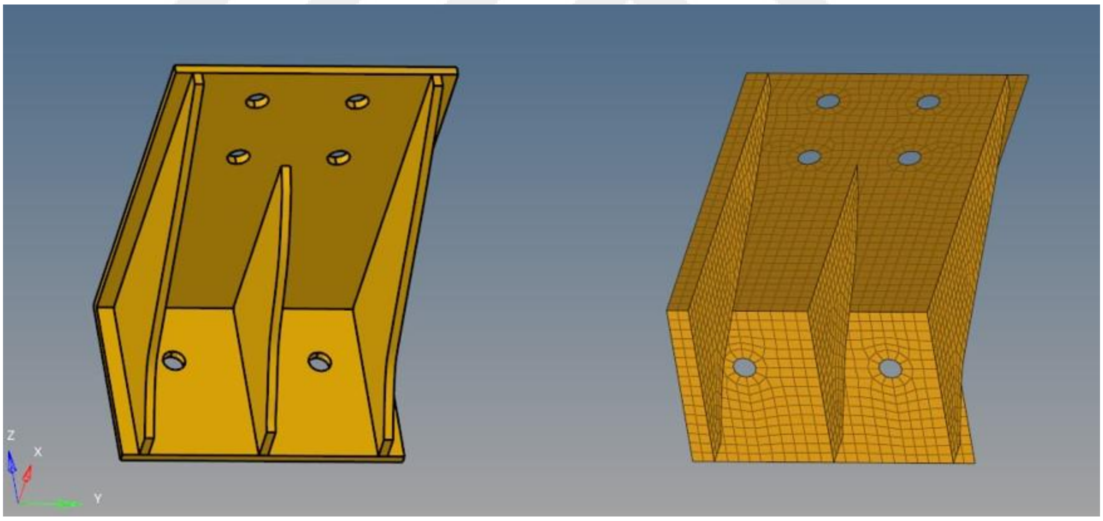

Figure 5.16 FE model of bracket design 1

The first natural frequency of bracket design 1 is compared to the existing design, and it is observed that the first mode increased by 23%, as shown in Table 5.4. In bracket design 1, there are three modes below 50Hz. The minimum fatigue life of bracket design 1 is calculated as 2525 cycles as depicted in Figure 5.17. The bracket's fatigue life increased from 242 cycles to 2525 cycles.

Table 5.4 Comparison of the natural frequencies of the existing design and bracket design 1

Mode	Frequency [Hz]		Increase Rate
	Existing Design	Bracket Design 1	
1	30.39	37.27	23%
2	30.78	37.82	23%
3	35.95	38.26	6%
4	44.64	52.47	18%
5	50.62	54.31	7%
6	70.06	72.22	3%

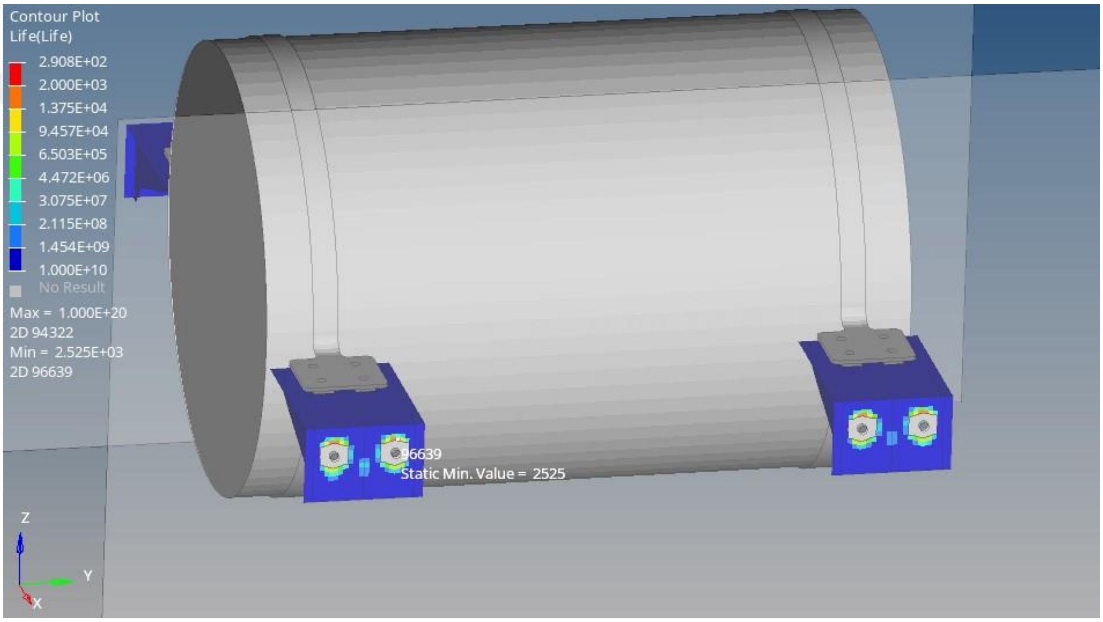

Figure 5.17 Fatigue life of the bracket design 1

A second design space is created in terms of access to the bolts during assembly, as shown in Figure 5.18. The density of each element in the design region is defined as a design variable. The design responses, constraints, and objective are the same as in the previous design.

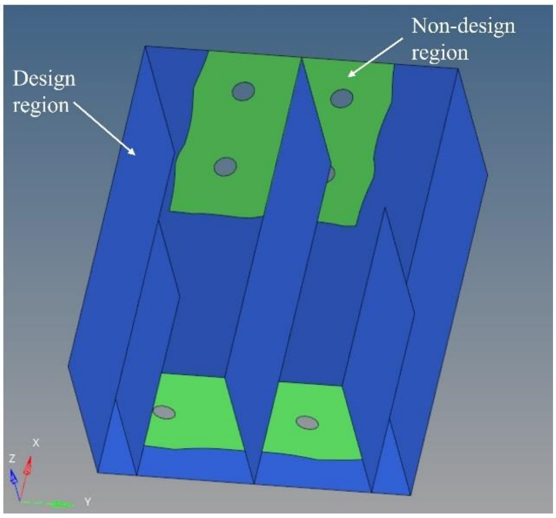

Figure 5.18 Design space of the bracket design 2

The topology optimization result for bracket design 2 is illustrated in Figure 5.19. The optimal design is exported in the form of an STL data format from HyperView. The FE model of bracket design 2 is illustrated in Figure 5.20. Modal and random-vibration fatigue analyses are repeated for the bracket design 2.

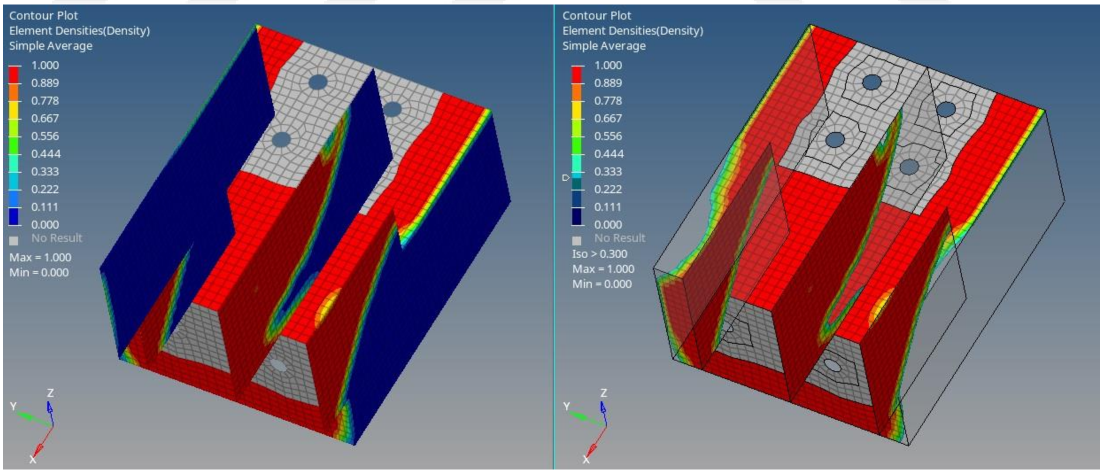

Figure 5.19 Topology optimization result for bracket design 2

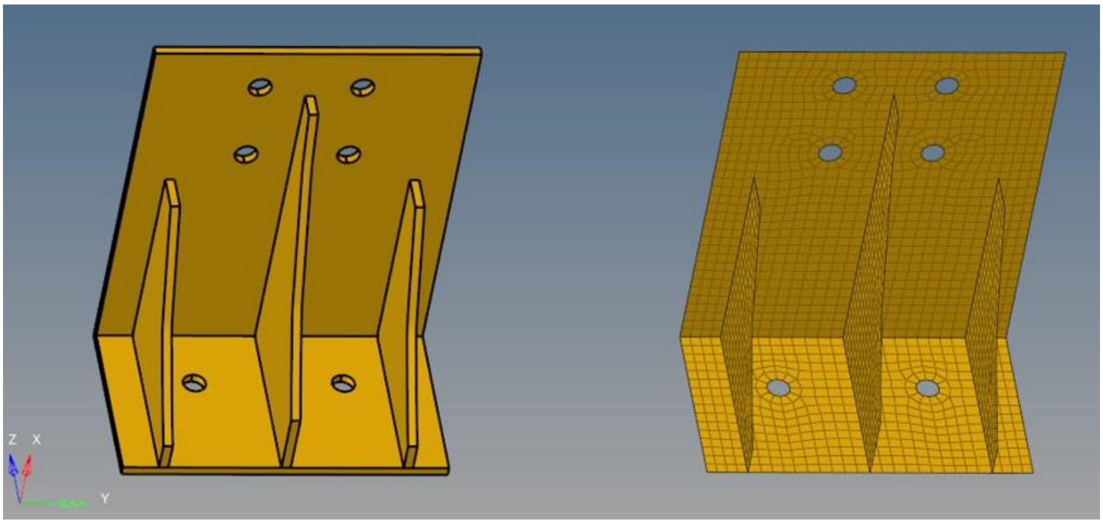

Figure 5.20 FE model of bracket design 2

The first natural frequency of bracket design 2 is compared to the existing design, and it is observed that the first mode increased by 22%, as shown in Table 5.5. In bracket design 2, there are three modes below 50Hz. The minimum fatigue life of bracket design 2 is calculated as 1123 cycles as shown in Figure 5.21Figure 5.17. The fatigue life of the bracket increased from 242 cycles to 1123 cycles.

Table 5.5 Comparison of the natural modes of the current bracket design and bracket design 2

Mode	Frequency [Hz]		Increase Rate
	Existing Design	Bracket Design 2	
1	30.39	37.14	22%
2	30.78	37.40	22%
3	35.95	37.85	5%
4	44.64	52.01	17%
5	50.62	53.22	5%
6	70.06	71.66	2%

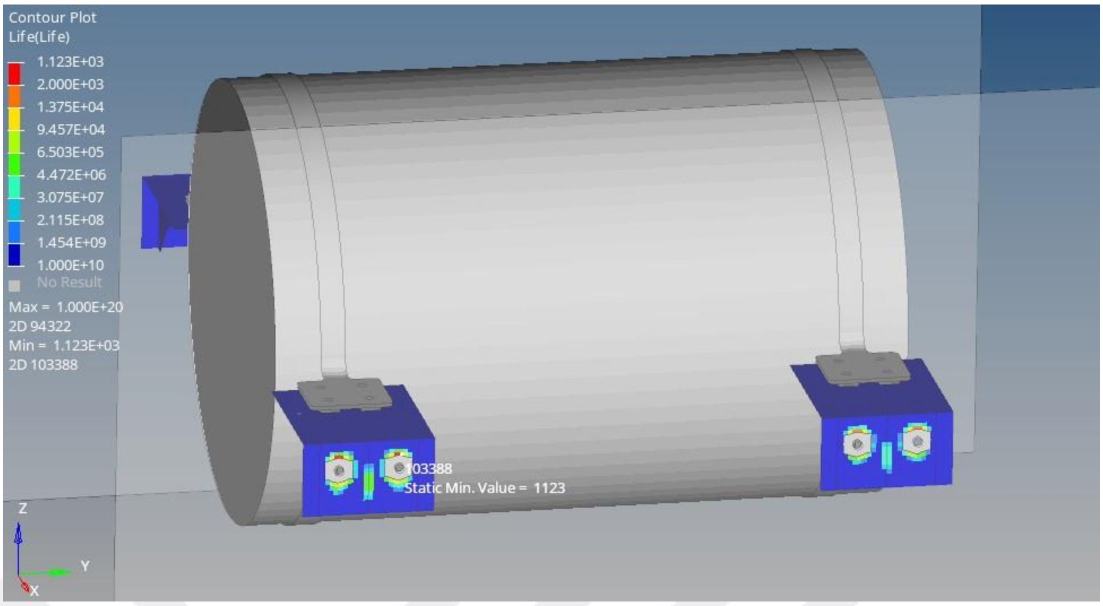

Figure 5.21 Fatigue life of the bracket design 2

Figure 5.22 demonstrates the first natural frequency change versus optimization iterations for bracket designs 1 and 2. When the modal analyses are conducted with the generated FE models again, it is apparent that the results are consistent with optimization results. The bracket's mass decreased by 18-20% and the first and second natural frequency values of bracket designs increased by 22-23% compared to the existing design. Table 5.6 illustrates that both bracket designs 1 and 2 are not superior to each other in terms of the first natural frequency. Also, there are three modes below 50Hz. The fatigue life on the brackets, on the other hand, have altered dramatically, as shown in Table 5.7.

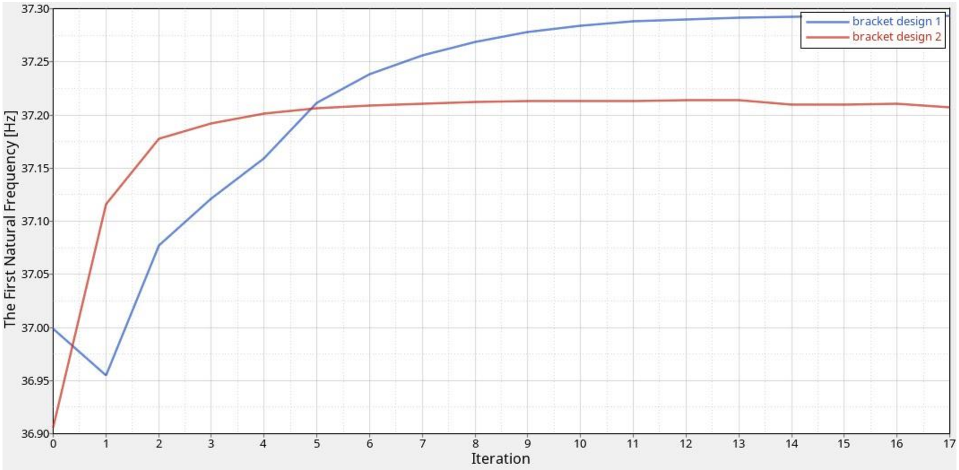

Figure 5.22 The first natural frequency change versus iterations for bracket designs 1 and 2

Table 5.6 Comparison of the frequencies of the existing design and optimization results

Mode	Frequency [Hz]		
	Existing Design	Bracket Design 1	Bracket Design 2
1	30.39	37.27	37.14
2	30.78	37.82	37.40
3	35.95	38.26	37.85
4	44.64	52.47	52.01
5	50.62	54.31	53.22
6	70.06	72.22	71.66

Table 5.7 Fatigue life evaluation on existing design and bracket optimization designs

Fatigue Life [Cycle]		
Existing Design	Bracket Design 1	Bracket Design 2
242	2525	1123

5.2.2 Topology Optimization for Spars

The FE model of bracket design 1 is preferred in spar topology optimization due to its high fatigue life. Figure 5.23 demonstrates the design space of the spars that are separated into design and non-design regions. The density of each element in the design region is defined as a design variable. The region of connection holes is defined as the non-design region and extracted from the design variable component.

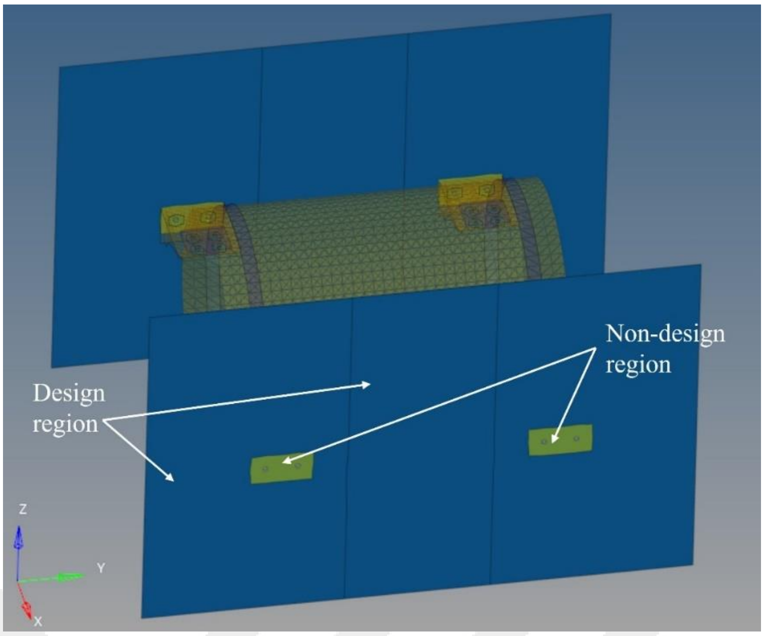

Figure 5.23 Design space of the spars

Volume fraction and compliance index were defined as optimization responses. The volume fraction of the design region of the spars was chosen as the topology upper bound constraint. The objective is to minimize the compliance index and, therefore, increase the rigidity and natural frequency values of the components of the hydraulic reservoir tank system.

The element densities of the spars are weighted 0 to 1 in the topology optimization. A weighted ratio of 1 means that material must be put into that region, while a weighted ratio of 0 indicates that the material does not need to be added to that region. The topology optimization result for spars is illustrated in Figure 5.24. According to the topology optimization results, it is concluded that regions with an element density of less than 0.3 are not needed. In the FE model, these regions represent the base thickness of the spars, and element densities greater than 0.3 indicate the regions that more material should be added. Also, the thickness of the minimum size of three elements around the non-design space of the spars is assigned an element density of 1. The purpose here is to make the bracket contact the spar surface and avoid the sharp thickness change in the connection regions.

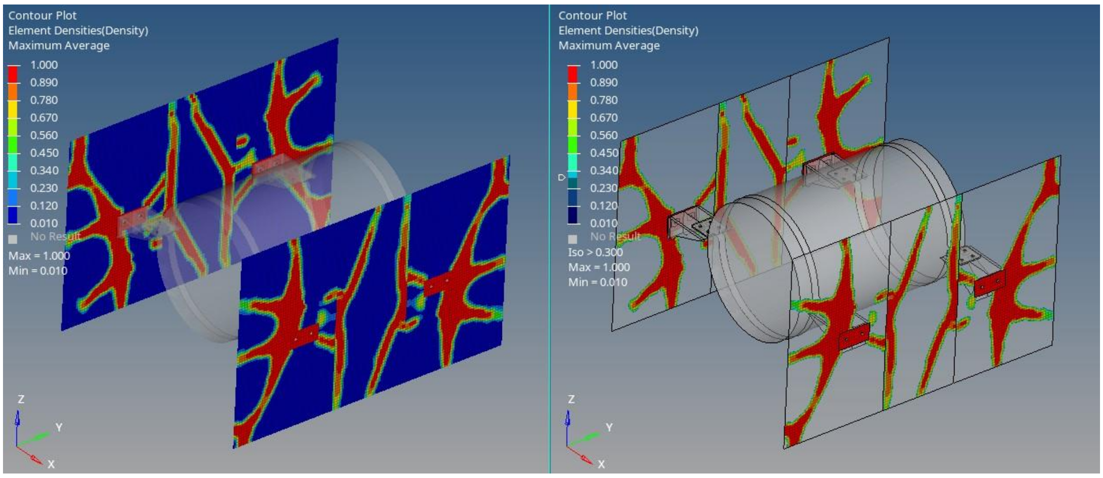

Figure 5.24 Topology optimization result for spars

The optimized design of the spars is exported in the form of an STL data format from HyperView. The FE model of spars is illustrated in Figure 5.25. The base thickness of the spars is defined as 3mm. The thickness of the optimized regions with element densities greater than 0.3 is taken as 5 mm. The thickness transition between the base thickness and the reinforcement regions is defined as 4 mm.

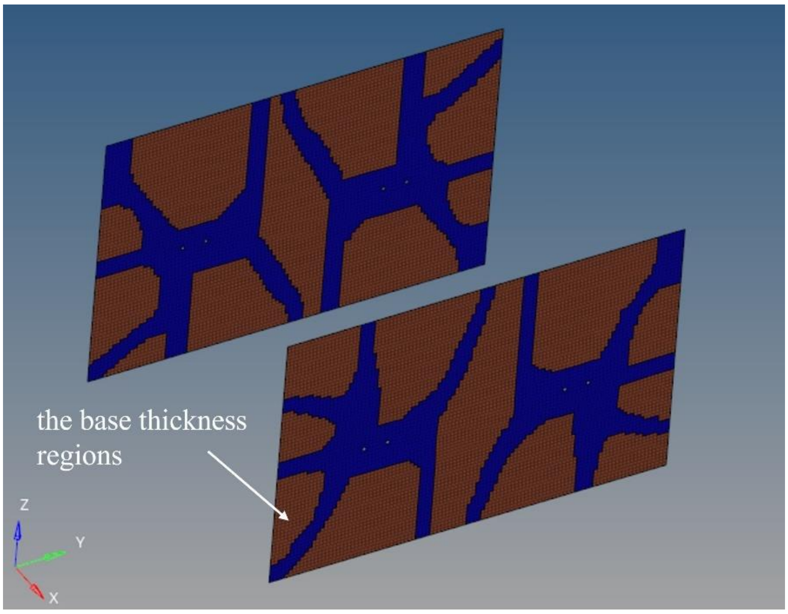

Figure 5.25 FE model of spars

Modal and random-vibration fatigue analyses are repeated for the optimized design of the spars and the results are compared to the current model (bracket design 1). When the natural frequencies of the optimized spar design are compared to the current model (bracket design 1), it is found that there are two modes under the target frequency value of 50 Hz, as indicated in Table 5.8.

Table 5.8 Assessment of the current model’s natural frequencies (bracket design 1) with the optimized spar design’s

Mode	Frequency [Hz]		Increase Rate
	Current Model (Bracket Design 1)	Optimized Spar Design	
1	37.27	46.95	26%
2	37.82	47.58	26%
3	38.26	52.42	37%
4	52.47	66.83	27%
5	54.31	75.65	39%
6	72.22	99.38	38%

The minimum fatigue life of the optimized spar design is calculated as 179 cycles as depicted in Figure 5.26.

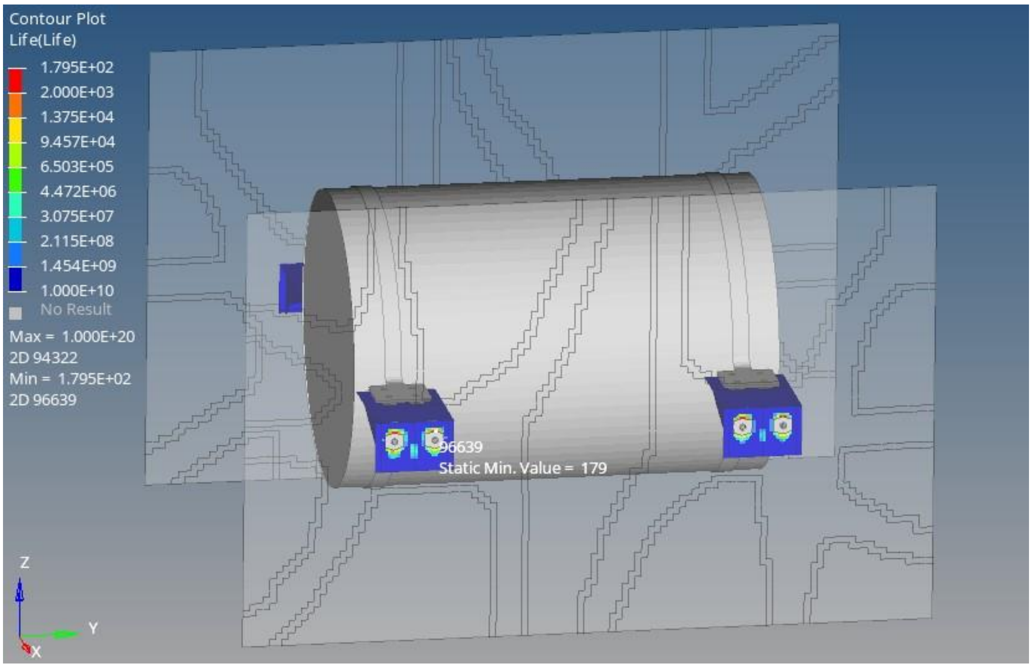

Figure 5.26 The optimized spar design’s fatigue life result

5.2.3 Size Optimization for Brackets and Spars

The first natural frequency of the optimized spar design is still below the target frequency and is 46.95Hz. Size optimization has been conducted on brackets and spars to achieve the goals. Figure 5.27 shows the thickness map of the optimized spar design before size optimization.

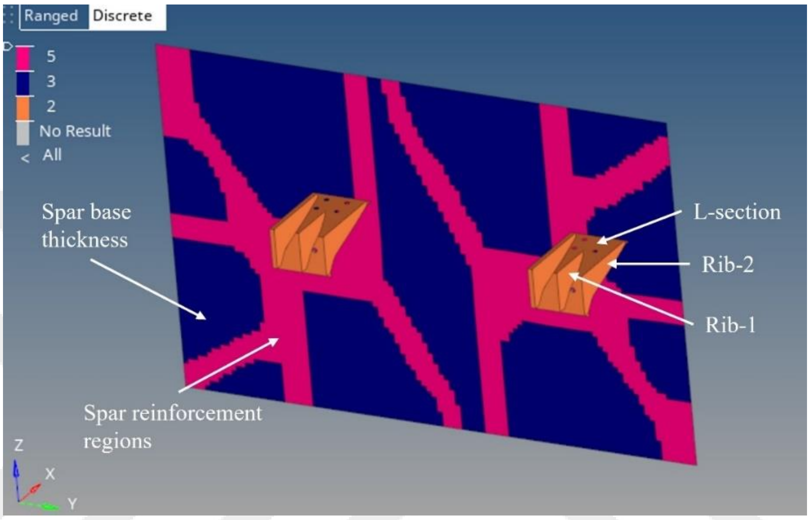

Figure 5.27 Thickness map of brackets and spars before size optimization

The property of the components is specified as a function of design variables rather than being the design variable in size (parameter) optimization. Accordingly, it could be possible to establish numerous parameters that rely on each other.

The thickness of the components was chosen as the property in size/parameter optimization. A linear combination of design variables is the most basic description of the design-variable-to-property association. The thickness property of each component was associated with a separate design variable as a linear function in this optimization study.

The thicknesses of L-sections and ribs, the thicknesses of the spars, and the reinforcement regions on them were specified as design variables in the size/parameter optimization. The thicknesses of L-sections and ribs were defined as parameters ranging from 2 to 2.5 mm and 2 to 3 mm, respectively. Also, the base thickness of the spars and the reinforcement regions on the spar were predetermined as parameters changing between 2 and 4 mm and 2 to 6 mm. The lower and upper limitations of the design variables are given in Table 5.9.

Table 5.9 Lower and upper limits of the design variables

Design Variables	Thickness [mm]				Comment
	Initial Value	Lower Bound	Upper Bound	Move Limit	
desvar_1	2	2	2.5	0.1	L-sections
desvar_2	2	2	3	0.1	Rib-1
desvar_3	2	2	3	0.1	Rib-2
desvar_4	2	2	4	0.1	Spar Base Thickness
desvar_5	2	2	6	0.1	Spar Reinforcement Regions

The mass and the first natural frequency value were defined as optimization responses. The first natural frequency of the hydraulic reservoir tank system is restricted between the lower bound of 50Hz and the upper bound of 55Hz. The purpose is to minimize the total mass of the design space components.

The initial thickness map of brackets and spars is illustrated in Figure 5.28 and the components of the hydraulic reservoir tank system are assigned a 2 mm thickness as an initial value.

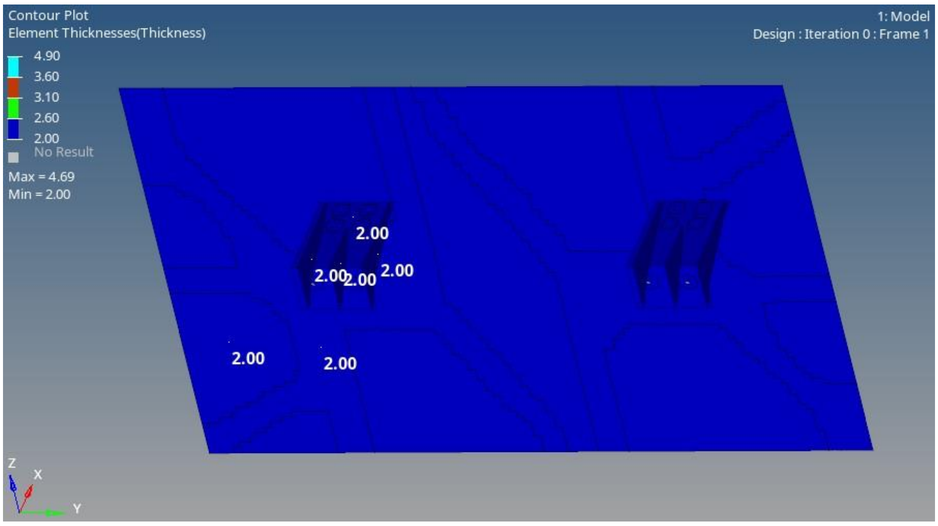

Figure 5.28 Initial thickness map of brackets and spars in size/parameter optimization

The first natural frequency constraint exceeds the lower bound of the design response after eleven iterations of size/parameter optimization and is obtained as 50.52Hz. Figure 5.29 and Figure 5.30 demonstrate changes in the first natural frequency and the mass during the iterations of size/parameter optimization, respectively.

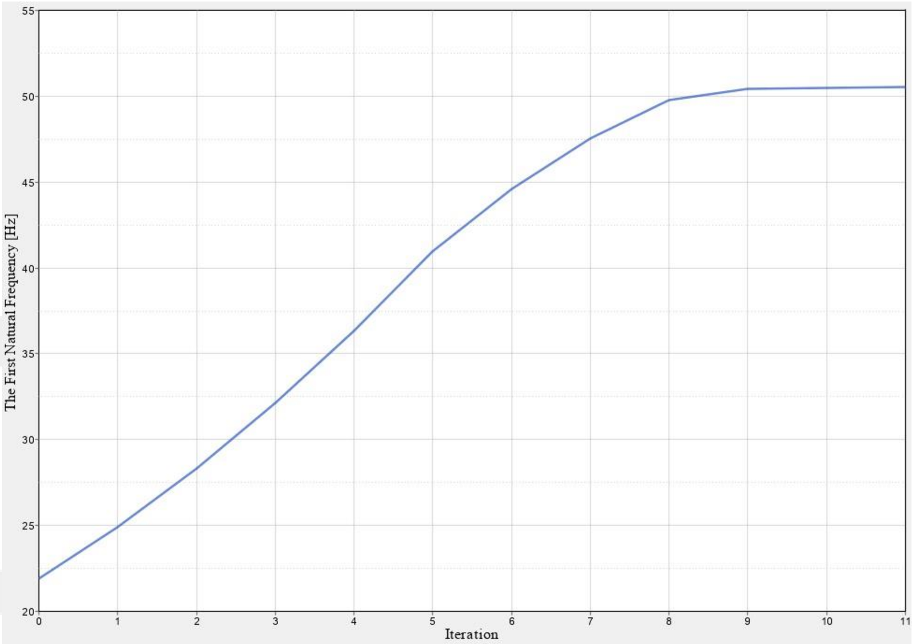

Figure 5.29 The first natural frequency change during the size/parameter optimization

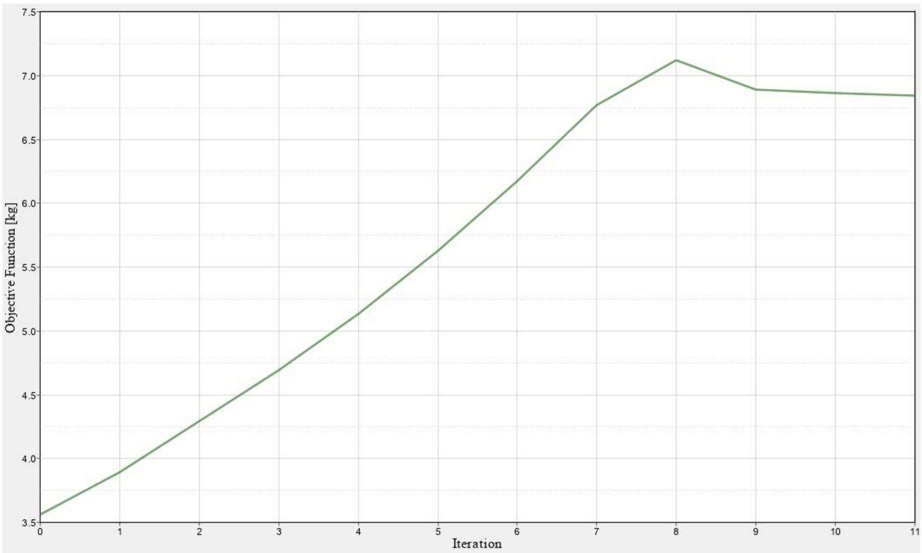

Figure 5.30 Objective function change during the size/parameter optimization

The thickness map of brackets and spars after size/parameter optimization is illustrated in Figure 5.31. The thicknesses of L-sections and ribs were obtained from the optimization result as 2.5 mm and 3 mm, respectively. As a consequence of the optimization analysis, it is concluded that the thickness of the spar's base is at 3.5 mm and the thickness of the spar's reinforcing regions is at 4.7 mm.

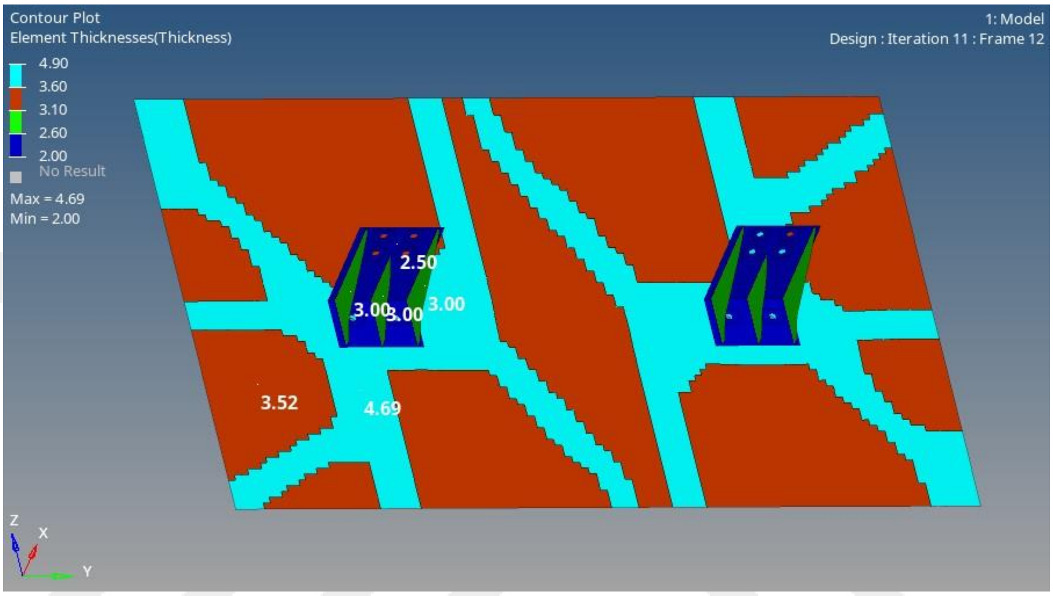

Figure 5.31 Thickness map of brackets and spars after size/parameter optimization

5.3 The Optimized Hydraulic Reservoir Tank System Components

Topology and size/parameter optimizations were performed to reach the target of the first natural frequency and fatigue life. The thickness values of the optimized hydraulic reservoir tank system components are listed in Table 5.10, and illustrated in Figure 5.32.

Table 5.10 Thickness map [mm] of the optimized hydraulic reservoir tank system components

Components	Thickness [mm]
L-sections	2.5
Rib-1	3
Rib-2	3
Spar Base Thickness	3.5
Spar Reinforcement Regions	4.7

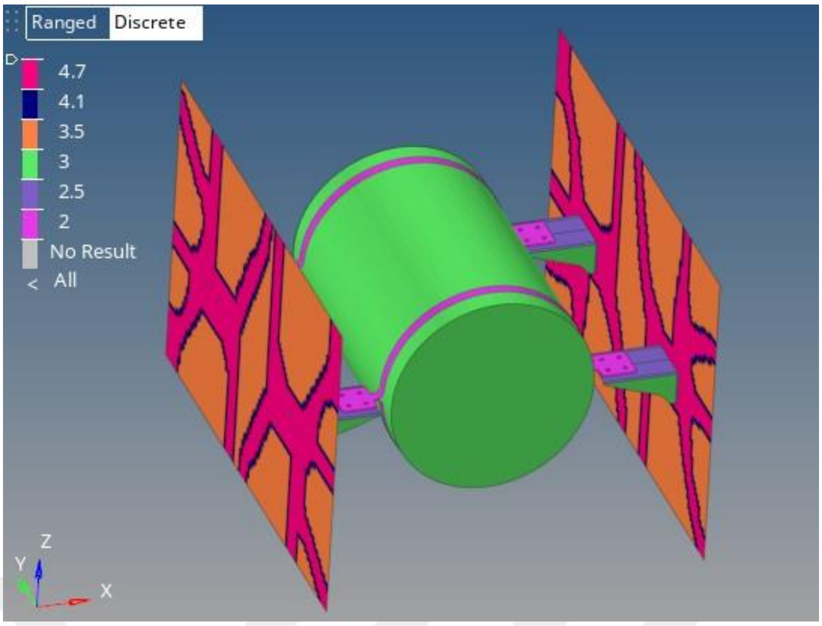

Figure 5.32 Thickness map [mm] of the optimized hydraulic reservoir tank system components

5.3.1 Modal Analysis of the Optimized Hydraulic Reservoir Tank System

The purpose of the topology and size optimization study to determine efficient design space is to improve the first natural frequency of the hydraulic reservoir tank system as well as the fatigue life. The optimization study for the brackets was completed first, followed by the optimization of the thickness map for the spars. Finally, in order to increase the first natural frequency and fatigue life, the thickness properties of both brackets and spars were defined as design parameters in size/parameter optimization.

The first natural mode of the optimized design is higher than the target frequency. As a result of the optimization study, a percent improvement of 78 according to the existing design was obtained. The first natural frequency increased from 30.39 Hz to 54.07 Hz compared to the existing design. The natural frequencies of the existing and optimized designs of the hydraulic reservoir tank system are examined in Table 5.11. In addition, the total mass change is also given in the table. Compared to the existing model, the total mass has been increased by 11%.

Table 5.11 Comparison of the natural modes and the total mass changes of the existing and optimized designs

	Frequency [Hz]						Total Mass [kg]
	Mode 1	Mode 2	Mode 3	Mode 4	Mode 5	Mode 6	
Existing Design	30.39	30.78	35.95	44.64	50.62	70.06	15.48
Optimized Design	54.07	55.07	56.37	73.53	80.86	103.34	17.13
Increase Rate	78%	79%	57%	65%	60%	48%	11%

The modal analysis of the optimized hydraulic reservoir tank system is restricted by the x, y, and z axes of the nodes at the front-rear edges of spars as well as the x and y axes of the nodes at the up-down edges. The same frequency range is defined in the modal analysis since the PSD data that will be employed for the random-vibration fatigue evaluation is up to 2000Hz. Utilizing the Lanczos eigenvalue extraction technique, analysis was carried out in the OptiStruct solver. In figures between Figure 5.33 and Figure 5.38, the system's free vibration mode shapes are illustrated.

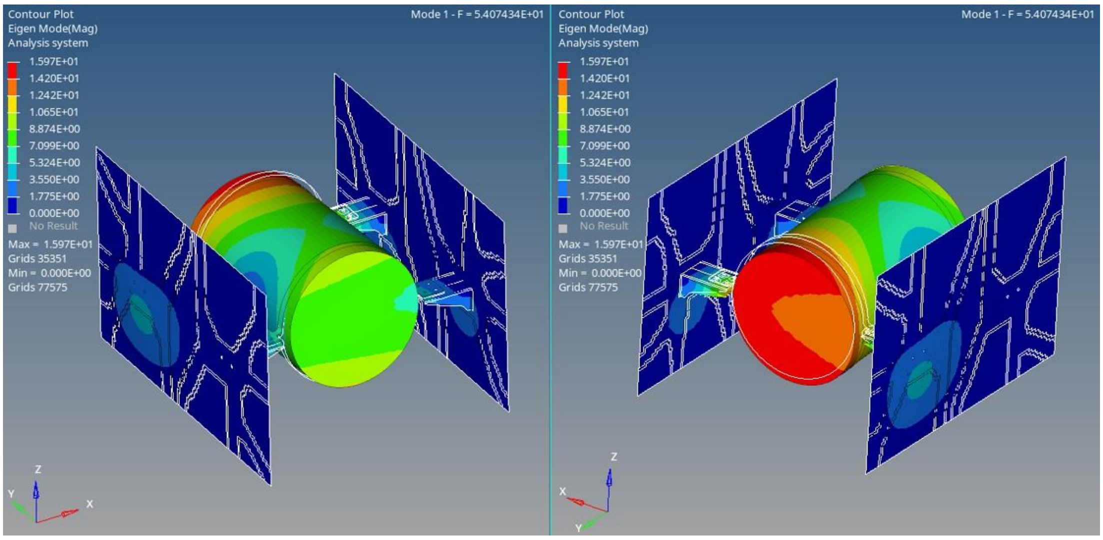

Figure 5.33 The first mode shape of the optimized hydraulic reservoir tank system components (Mode-1 f=54.07 Hz)

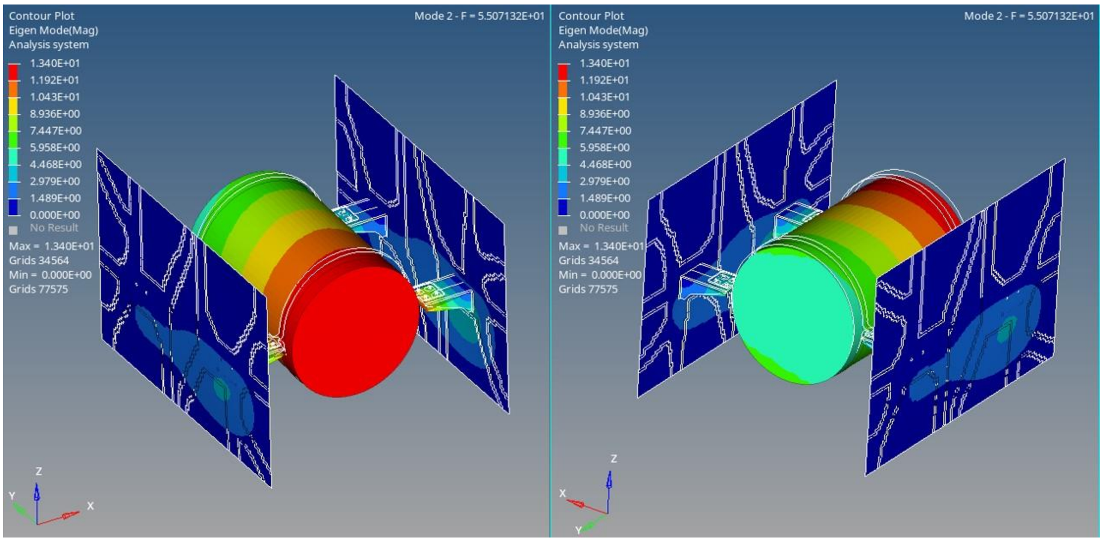

Figure 5.34 The second mode shape of the optimized hydraulic reservoir tank system components (Mode-2 f=55.07 Hz)

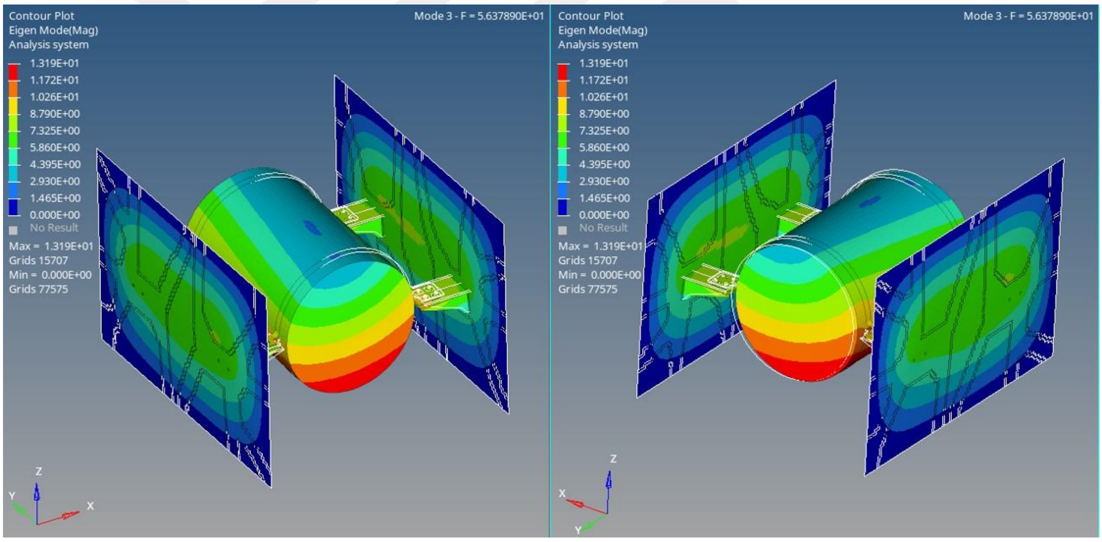

Figure 5.35 The third mode shape of the optimized hydraulic reservoir tank system components (Mode-3 f=56.37 Hz)

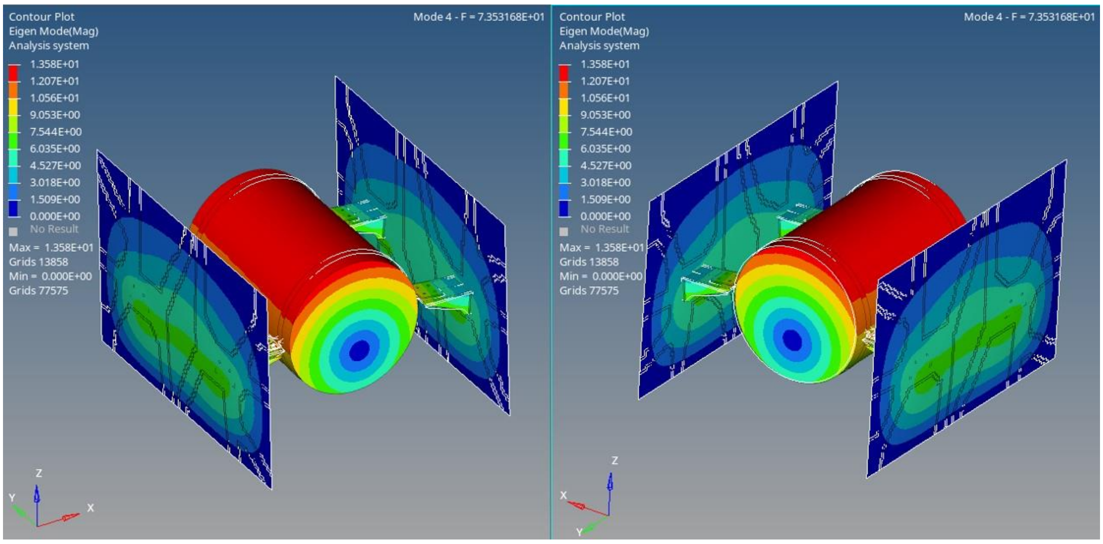

Figure 5.36 The fourth mode shape of the optimized hydraulic reservoir tank system components (Mode-4 f=73.53 Hz)

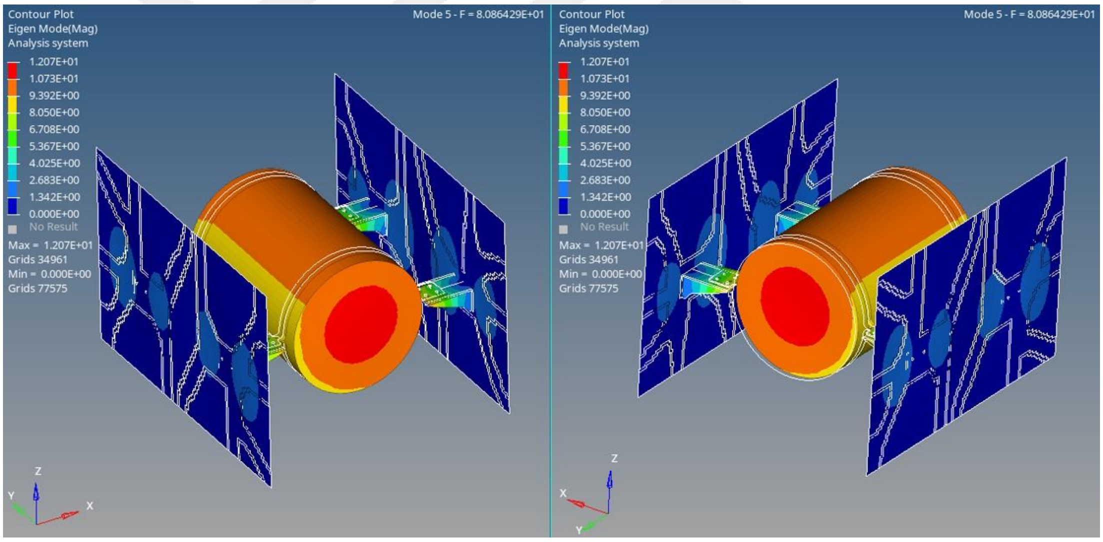

Figure 5.37 The fifth mode shape of the optimized hydraulic reservoir tank system components (Mode-5 f=80.86 Hz)

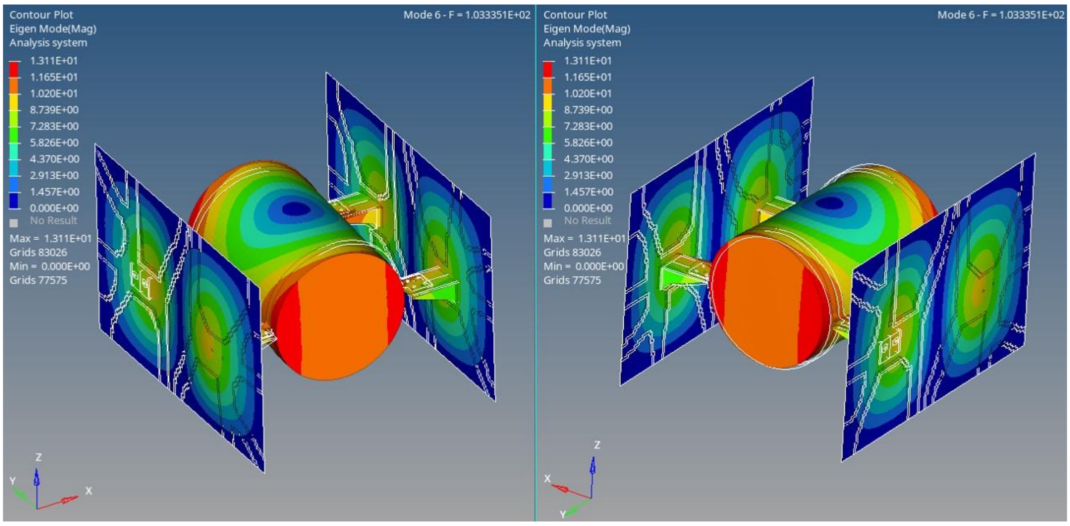

Figure 5.38 The sixth mode shape of the optimized hydraulic reservoir tank system components (Mode-6 f=103.34 Hz)

A numerical modal analysis was performed to determine the natural frequencies of the hydraulic reservoir tank system. Until 1000Hz, the natural frequencies are indicated in Table 5.12.

Table 5.12 The optimized hydraulic reservoir tank system's natural frequencies until 1000 Hz

Mode	Frequency [Hz]	Mode	Frequency [Hz]	Mode	Frequency [Hz]
1	54.07	24	559.75	47	985.51
2	55.07	25	567.32	48	995.43
3	56.38	26	580.59	49	1027.76
4	73.53	27	623.16		
5	80.86	28	632.93		
6	103.34	29	699.86		
7	209.61	30	707.73		
8	240.29	31	711.84		
9	278.20	32	720.82		
10	299.14	33	725.25		
11	370.46	34	728.88		
12	374.44	35	750.86		
13	428.91	36	761.20		
14	436.38	37	763.40		
15	437.20	38	784.33		
16	439.93	39	795.68		
17	443.08	40	810.18		
18	448.08	41	832.55		
19	476.50	42	838.61		
20	497.36	43	846.54		
21	499.41	44	877.15		
22	500.24	45	884.58		
23	518.93	46	895.95		

When the modal participation factor ratios of the optimized design are examined (Table 5.13), it is observed that the z-axis at the first and second modes, the x-axis at the third and fourth modes, and the y-axis at the fifth mode are dominant. This means that stress results at the dominant axis are higher than at other axes.

Table 5.13 Modal participation factors ratios of the optimized hydraulic reservoir tank system from modal analysis up to 1000 Hz

Mode	Frequency [Hz]	X-Trans	Y-Trans	Z-Trans	Mode	Frequency [Hz]	X-Trans	Y-Trans	Z-Trans	Mode	Frequency [Hz]	X-Trans	Y-Trans	Z-Trans
1	54.07	14%	2%	35%	24	559.70	1%	0%	0%	47	985.50	8%	0%	1%
2	55.07	3%	1%	100%	25	567.30	18%	0%	0%	48	995.40	11%	0%	0%
3	56.38	100%	0%	3%	26	580.60	3%	0%	1%	49	1028.00	2%	0%	0%
4	73.53	56%	0%	3%	27	623.20	4%	0%	2%	50				
5	80.86	1%	100%	0%	28	632.90	9%	0%	1%	51				
6	103.30	0%	4%	1%	29	699.90	0%	0%	1%	52				
7	209.60	0%	0%	0%	30	707.70	0%	0%	0%	53				
8	240.30	0%	6%	0%	31	711.80	1%	0%	0%	54				
9	278.20	1%	0%	5%	32	720.80	0%	4%	0%	55				
10	299.10	11%	0%	1%	33	725.30	0%	5%	0%	56				
11	370.50	0%	0%	6%	34	728.90	0%	1%	0%	57				
12	374.40	0%	0%	4%	35	750.90	0%	0%	0%	58				
13	428.90	1%	1%	0%	36	761.20	1%	0%	0%	59				
14	436.40	1%	0%	0%	37	763.40	9%	0%	0%	60				
15	437.20	0%	0%	0%	38	784.30	0%	0%	0%	61				
16	439.90	0%	0%	0%	39	795.70	0%	0%	1%	62				
17	443.10	0%	0%	0%	40	810.20	1%	0%	0%	63				
18	448.10	0%	0%	0%	41	832.50	0%	2%	0%	64				
19	476.50	12%	0%	0%	42	838.60	1%	2%	0%	65				
20	497.40	0%	0%	2%	43	846.50	0%	0%	0%	66				
21	499.40	0%	0%	0%	44	877.20	0%	1%	0%	67				
22	500.20	0%	0%	1%	45	884.60	0%	0%	0%	68				
23	518.90	0%	0%	0%	46	895.90	0%	0%	0%	69				

5.3.2 Frequency Response Analysis of the Optimized Hydraulic Reservoir Tank System under Unit Acceleration

Frequency response analysis is conducted to examine the transfer function relations of input acceleration with output stresses required for fatigue calculations. The analysis of frequency response under 1g mm/s^2 unit acceleration is performed after the modal analysis of the hydraulic reservoir tank system. The ratio of structural damping is considered to be 2%.

The structure is subjected to a sinusoidally fluctuating 1g unit loading excitation, which is defined separately for each axis. The stress response under 1g sinusoidal excitation in the z-axis is illustrated in Figure 5.39.

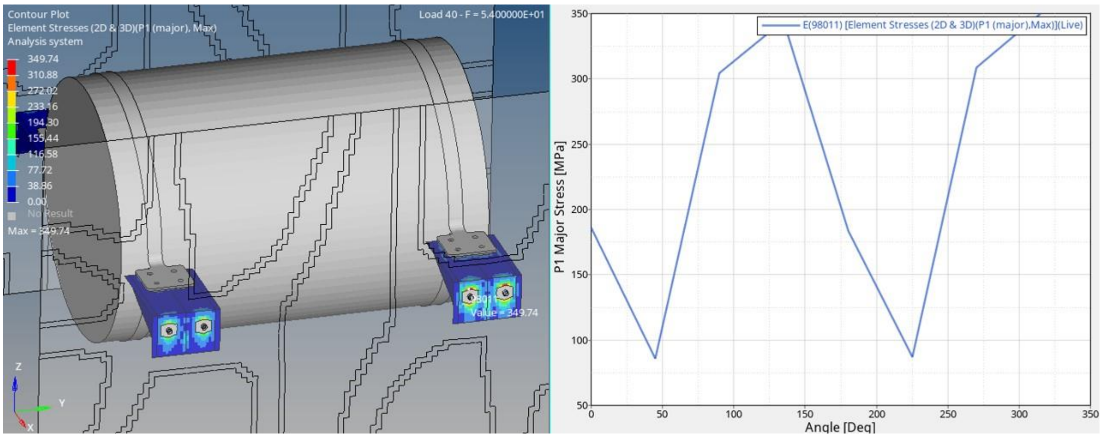

Figure 5.39 Stress response at 54 Hz under 1g sinusoidal excitation in the z-axis for frequency response analysis

From the numerical analysis, the transfer functions of the hydraulic reservoir tank system are extracted at each node. The frequency increment is set to 1 Hz and the stress values at each frequency are written to the output file. Figures from Figure 5.40 to Figure 5.42, respectively, represent the stress plot versus frequency obtained from the frequency response analysis under unit acceleration loading applied separately on the x, y, and z axes.

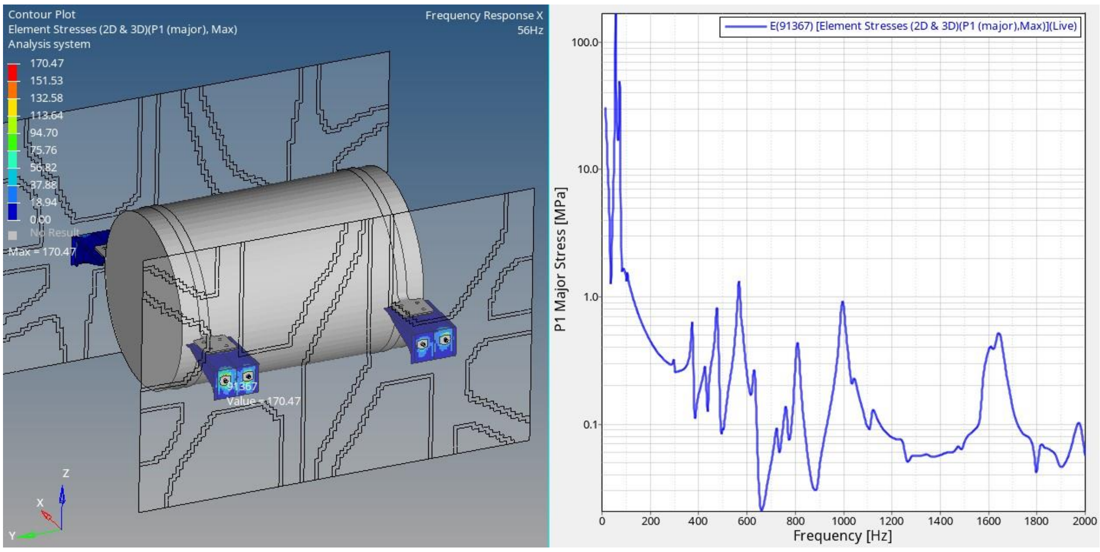

Figure 5.40 Maximum principal stress plot of the optimized design versus frequency obtained from the frequency response analysis under x axis unit loading (logarithmic scale)

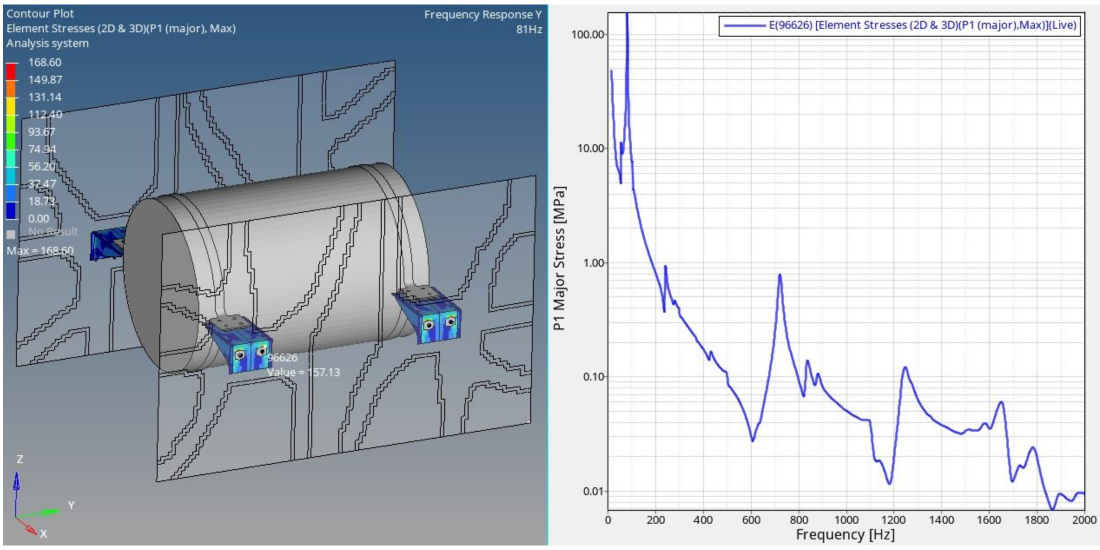

Figure 5.41 Maximum principal stress plot of the optimized design versus frequency obtained from the frequency response analysis under y axis unit loading (logarithmic scale)

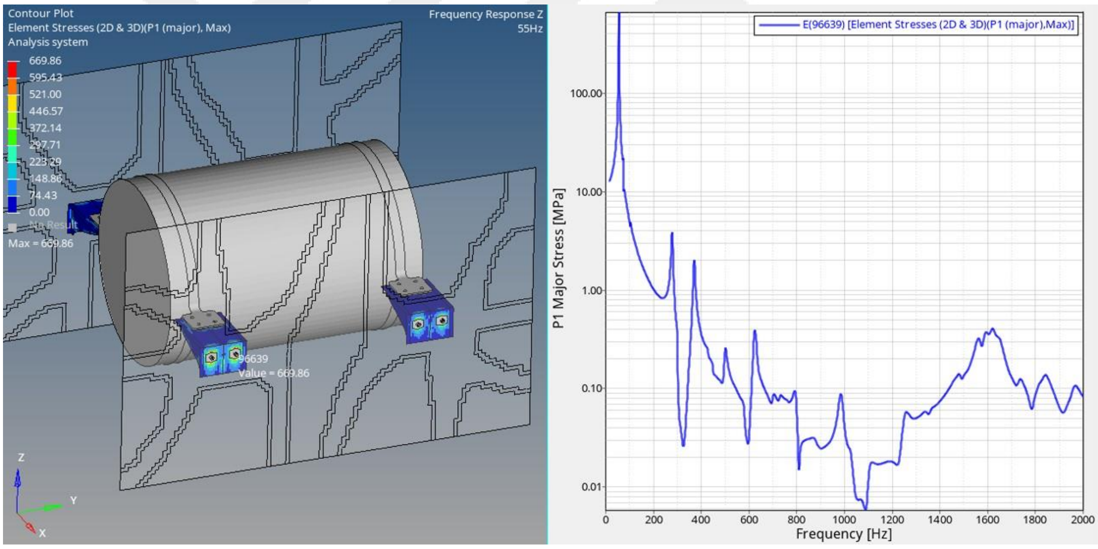

Figure 5.42 Maximum principal stress plot of the optimized design versus frequency obtained from the frequency response analysis under z axis unit loading (logarithmic scale)

5.3.3 Random Response Analysis of the Optimized Hydraulic Reservoir Tank System under Unit Acceleration

The inputs for random response analysis are the transfer functions derived from frequency response analysis and the PSD, which is taken from military standards.

The RANDPS definition is employed in Altair HyperMesh to define a load case of random response analysis. It combines the frequency response analyses of the x, y, and z directions with PSD excitation. The maximum RMS stress value is 93.46 MPa on the system brackets obtained from the random response analysis and it is illustrated in Figure 5.43. The frequency-dependent PSD stress curve in element number 96639, where the maximum RMS stress occurs, is depicted in Figure 5.44.

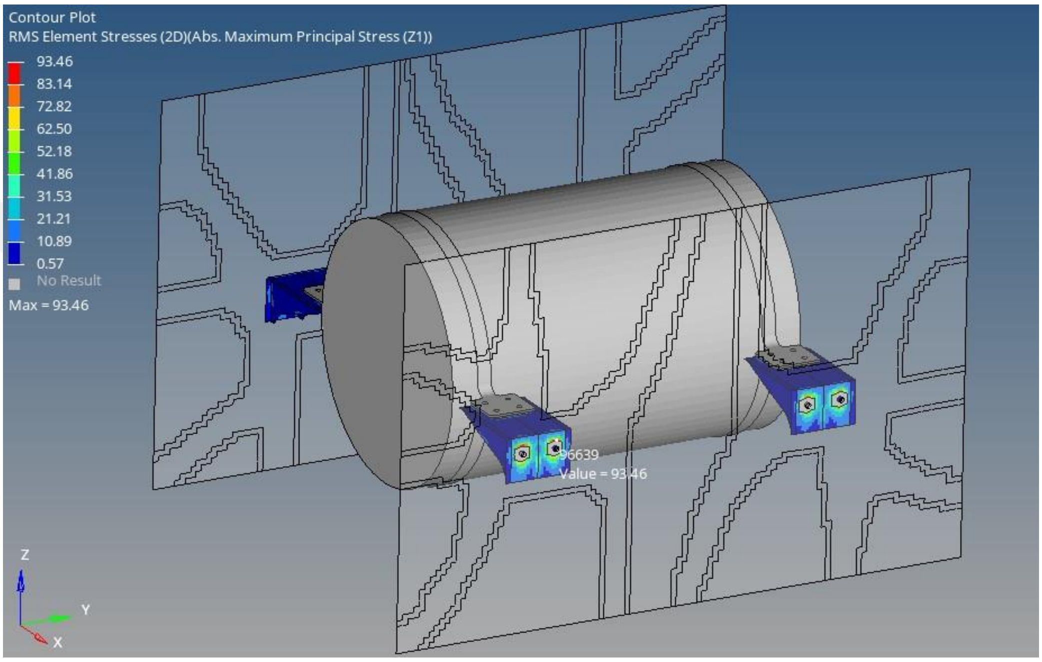

Figure 5.43 The maximum RMS stress value on the system brackets obtained from the random response analysis

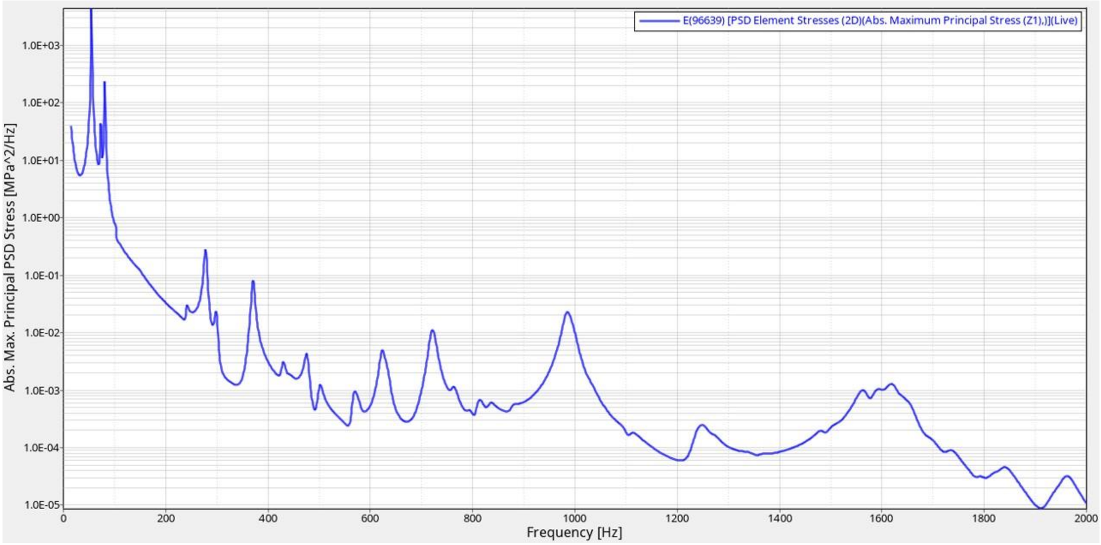

Figure 5.44 The frequency-dependent PSD stress curve in element number 96639

Evaluating the frequency dependent PSD stress graph of the existing and optimized designs in the range of 15Hz to 105Hz, including the first six natural frequencies, it is clearly seen that the natural frequencies of the optimized design are shifted above 50Hz. Also, the PSD stresses at each frequency of the optimized design were decreased compared to the existing design, as shown in Figure 5.45.

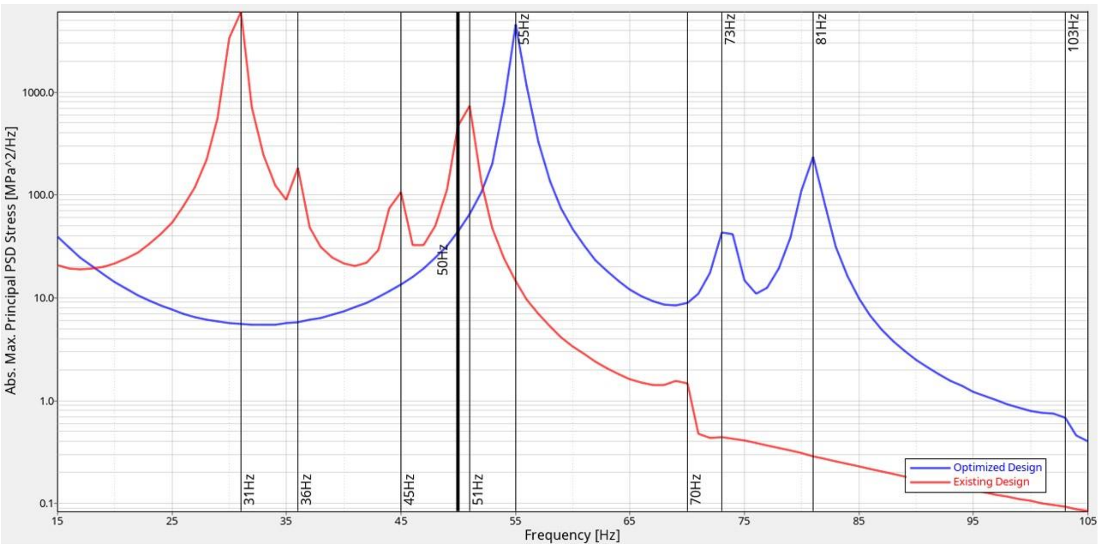

Figure 5.45 Comparison of the frequency dependent PSD stress plot of the existing and optimized designs

5.3.4 Random-Vibration Fatigue Analysis of the Optimized Hydraulic Reservoir Tank System under Unit Acceleration

After the frequency-dependent PSD stress curves are obtained from random response analysis, Dirlik's approach is used for assessing the random-vibration fatigue life of the optimized hydraulic reservoir tank system. In the numerical model, the effects of mean stress on fatigue are not taken into account. The absolute maximum principal stress value is preferred as the input of the analysis, and the total fatigue life is predicted from the stress ranges calculated by considering these stresses. The minimum fatigue life of the optimized hydraulic reservoir tank system brackets is calculated as 2297 cycles as depicted in Figure 5.46.

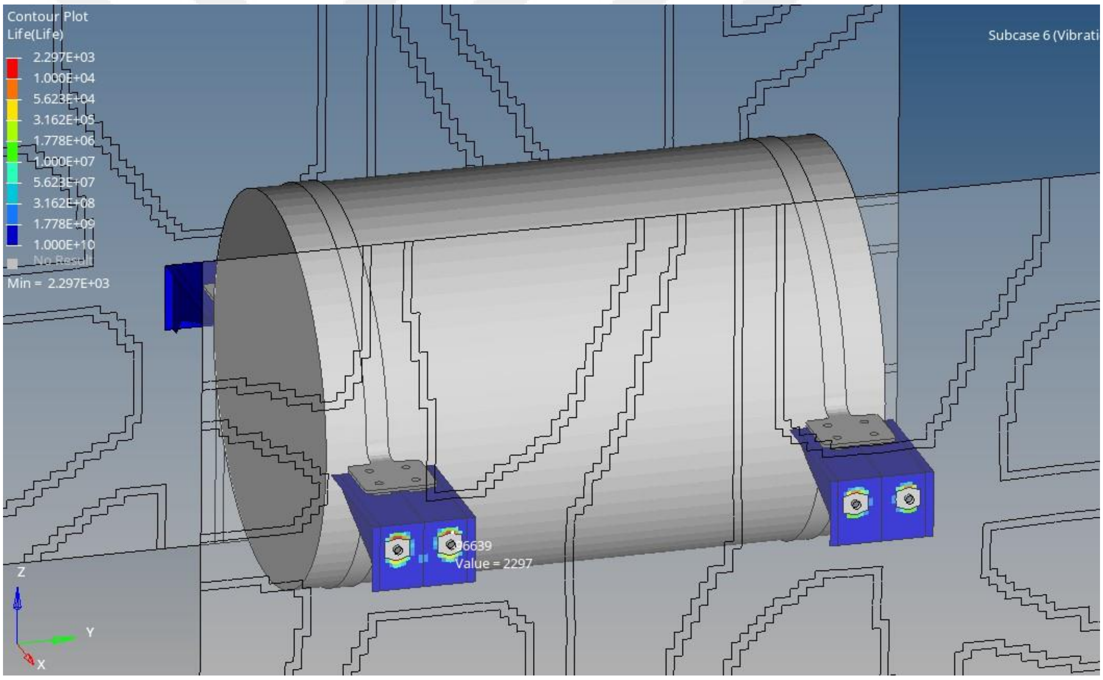

Figure 5.46 Fatigue life of the optimized hydraulic reservoir tank system brackets

The rainflow cycle count history might be extracted from the analysis. Its extension file is the RNF file, as shown in Table 5.14. It contains stress amplitudes, the probability of the corresponding stress amplitude occurring, the number of cycles of the specific stress amplitude, and the cumulative damage value of all cycles at the current stress amplitude. In the last row, total damage is given for the exposure duration of PSD.

The rainflow cycle count history of element number 96639 is demonstrated in Table 5.14. For a PSD exposure duration of 60 seconds, the total damage is 0.181412E-05. For a total exposure duration of 4 hours, total life could be calculated as 2297 cycles.

Table 5.14 Fatigue damage result table of random response fatigue analysis in element number 96639 for 60 second exposure duration

```
                               Element 96639
-------------------------------------------------------------------------------------------
Event 9 (1st of total 1 event): 98 stress amplitudes
-------------------------------------------------------------------------------------------
DIRLIK
 Stress #  Stress amp.    Prob.     No. of cycles  Mean stress   Cor. stress amp.  Damage
      1  0.373861E+01  0.118063E+00  0.311669E+02  0.000000E+00  0.373861E+01  0.000000E+00
      2  0.112158E+02  0.187774E+00  0.495697E+02  0.000000E+00  0.112158E+02  0.000000E+00
 .
 .
 .
     30  0.220578E+03  0.251346E-02  0.663517E+00  0.000000E+00  0.220578E+03  0.119525E-07
     31  0.228055E+03  0.213881E-02  0.564616E+00  0.000000E+00  0.228055E+03  0.151953E-07
     32  0.235532E+03  0.180743E-02  0.477135E+00  0.000000E+00  0.235532E+03  0.189376E-07
     33  0.243010E+03  0.151685E-02  0.400427E+00  0.000000E+00  0.243010E+03  0.231557E-07
     34  0.250487E+03  0.126423E-02  0.333739E+00  0.000000E+00  0.250487E+03  0.277998E-07
     35  0.257964E+03  0.104646E-02  0.276252E+00  0.000000E+00  0.257964E+03  0.327926E-07
     36  0.265441E+03  0.860297E-03  0.227106E+00  0.000000E+00  0.265441E+03  0.380312E-07
     37  0.272918E+03  0.702448E-03  0.185436E+00  0.000000E+00  0.272918E+03  0.433904E-07
     38  0.280396E+03  0.569689E-03  0.150390E+00  0.000000E+00  0.280396E+03  0.487281E-07
     39  0.287873E+03  0.458923E-03  0.121149E+00  0.000000E+00  0.287873E+03  0.538917E-07
     40  0.295350E+03  0.367231E-03  0.969438E-01  0.000000E+00  0.295350E+03  0.587264E-07
 .
 .
 .
     97  0.721551E+03  0.176284E-09  0.465365E-07  0.000000E+00  0.721551E+03  0.132377E-08
     98  0.729029E+03  0.143713E-09  0.379382E-07  0.000000E+00  0.729029E+03  0.122184E-08
===========================================================================================
         Total damage                              0.181412E-05
```

CHAPTER 6
CONCLUSIONS

Random-vibration fatigue is a typical source of damage to aerospace structures due to severe dynamic loads under operating conditions. If the load has dynamic characteristics and a broadband spectrum, the response of the structure probably proceeds at resonance frequencies, and the resonance effects cause rapid progression of the process from crack formation to fatigue failure in the structure. Accounting for dynamic effects, the random-vibration fatigue of the structure should be examined in the frequency domain; otherwise, it becomes unavoidable to have catastrophic failure due to random cyclic load and the operating frequency range of the structure.

For the calculation of random-vibration fatigue where loading is applied in the frequency domain, the result of the frequency response analysis of the structure under unit load and the PSD data of the dynamic loading to be applied are needed. For this purpose, first a modal analysis of the structure is carried out to find natural frequencies. It is preferred that the natural frequencies of the structure should be higher than the operating frequency to avoid resonance effects. Second, the frequency response analyses based on the modal stress approach are performed under unit acceleration loading at each axis. The structure's transfer functions are the outputs of the frequency response analyses that were performed at three axes separately. The random response analysis inputs are the transfer functions of the structure and random dynamic loading in the frequency domain. Dynamic load is represented by PSD data in the frequency domain. In this study, it is taken from military standards. Stress levels are obtained from the random response analysis, which is the result of multiplying the transfer function with PSD. The accumulation of vibration-fatigue damage is estimated using the Palmgren-Miner rule. The Dirlik method is preferred for calculating fatigue life since it is a well-known approach and provides accurate results over a wide band spectrum.

In this thesis, structural random-vibration fatigue evaluation of hydraulic reservoir system brackets with a modal stress approach is performed in the frequency domain by using Altair HyperWorks software with OptiStruct solver. The system is expected to meet the natural frequency and random vibration fatigue life targets. The target minimum natural frequency of the hydraulic reservoir tank system should be higher than 50 Hz due to being stimulated by the hydraulic pump at a maximum of 3000 rpm. For evaluating random-vibration fatigue life, the random response analysis is repeated 240 times and then total damage is calculated. The target fatigue life is determined to be at least 2000 cycles. Another aim of this research is to discuss and show how the optimization study may be implemented to enhance fatigue life in the frequency domain.

The existing hydraulic reservoir tank system's analysis results do not meet the targets for both natural frequency and fatigue life. Thus, optimization studies are performed to provide the system's targets. The components of the hydraulic reservoir tank system are connection brackets and spars. The optimization study is divided into two steps. First, the topology optimization is conducted for brackets and then for spars.

Two different topology optimization studies were performed for bracket design. The first natural frequencies of the designs are almost the same. On the other hand, there is almost a 2-times difference for fatigue life. It is preferred that the bracket design 1 model that has both a high natural frequency and a high fatigue life. As a result, the system's first natural frequency is raised from 30.39 Hz to 37.27 Hz, and bracket fatigue life is increased from 242 to 2525 cycles. Bracket optimization study has been completed. Then the optimization study for spar is passed. The regions that need to be thickened on the spar are obtained from the topology optimization. It is called the reinforcement regions of the spar. As a result of the topology optimization, the first natural frequency of the system reaches 46.95 Hz, and the fatigue life of the brackets is obtained as 179 cycles. With this study, the system still does not provide the targets. After that, size/parameter optimization studies are conducted on brackets and spars to achieve the system targets. The size/parameter optimization is performed to increase the first natural frequency of the system and brackets fatigue life. Optimized thickness map of brackets and spars is obtained from that study.

The system's first natural frequency is increased from 30.39 Hz to 54.07 Hz after topology and size/parameter optimizations, and bracket fatigue life is enhanced from 242 to 2297 cycles. Considering the numerical results obtained, it can be said that the targeted values for the system have been achieved.

REFERENCES

Altair 2021 Student Edition: OptiStruct. (2022, January 1). https://2021.help.altair.com/2021/hwsolvers/os/

Benasciutti, D., & Tovo, R. (2005). Spectral methods for lifetime prediction under wide-band stationary random processes. *International Journal of fatigue*, *27*(8), 867-877.

Bendat, J. S. (1964). Probability functions for random responses: prediction of peaks. *Fatigue Damage and Catastrophic Failures, NASA technical report.*

Bendsoe, M. P., & Sigmund, O. (2003). *Topology optimization: theory, methods, and applications.* Springer Science & Business Media.

Bishop, N. W. M., & Sherratt, F. (1989). Fatigue life prediction from power spectral density data. *Environmental Engineering*, *2*(1), 2-11.

Bishop, N. W. M., & Sherratt, F. (2000). Finite Element Based Fatigue Calculations (NAFEMS). *Glasgow, UK.*

Cooley, J. W., & Tukey, J. W. (1965). An algorithm for the machine calculation of complex Fourier series. *Mathematics of computation*, *19*(90), 297-301.

Demirel, G. İ., & Kayran, A. (2019). Implementation of Dirlik's damage model for the vibration fatigue analysis. *Procedia structural integrity*, *21*, 101-111.

Dowling, N. E. (2013). Mechanical Behaviour of Materials. Engineering Methods for Deformation, Fracture, and Fatigue. Fourth.

Dirlik, T. (1985). *Application of computers in fatigue analysis* [Doctoral dissertation]. University of Warwick.

Element Materials Technology. (2022, June 4). *Five disasters caused by material fatigue and what we learned from them.* https://www.element.com/nucleus/2016/5-disasters-caused-by-material-fatigue-and-what-we-learned-from-them

Gao, Z., & Moan, T. (2008). Frequency-domain fatigue analysis of wide-band stationary Gaussian processes using a trimodal spectral formulation. *International journal of fatigue*, *30*(10-11), 1944-1955.

Halfpenny, A. (1999). A frequency domain approach for fatigue life estimation from finite element analysis. *Key Engineering Materials*, *167*, 401-410.

Matsuishi, M., & Endo, T. (1968). Fatigue of metals subjected to varying stress. *Japan Society of Mechanical Engineers*, *Fukuoka*, *Japan*, *68*(2), 37-40.

MIL-STD-810F. (2000). *Environmental Engineering Considerations and Laboratory Tests*, *Department of Defense Test Method Standard, USA.*

Mrsnik, M., Slavic, J., & Boltezar, M. (2013). Frequency-domain methods for a vibration-fatigue-life estimation–application to real data. *International journal of fatigue*, *47*, 8-17.

Naess, A. A., Haagensen, P. J., Lian, B., Moan, T., & Simonsen, T. (1982, May). Investigation of the Alexander L. Kielland failure-metallurgical and fracture analysis. In *Offshore Technology Conference*. OnePetro.

nCode 11.0: Material Library Documentation. (2022, July 23). https://www.ncode.com

Querin, O. M., Victoria, M., Alonso, C., Loyola, R. A., & Montrull, P. M. (2017). *Topology design methods for structural optimization*. Butterworth-Heinemann.

Quigley, J. P., Lee, Y. L., & Wang, L. (2016). Review and assessment of frequency-based fatigue damage models. *SAE International Journal of Materials and Manufacturing*, *9*(3), 565-577.

Rahman, M. M., Ariffin, A. K., Jamaludin, N., Haron, C. H. C., & Bakar, R. A. (2008). Fatigue life prediction of two-stroke free piston engine mounting using frequency response approach. *European journal of scientific research*, *22*(4), 480-493.

Rice, S. O. (1954). Mathematical analysis of random noise. Selected papers on noise and stochastic processes. *Dover*, *New York*, 133-294.

Schijve, J. (Ed.). (2009). *Fatigue of structures and materials*. Dordrecht: Springer Netherlands.

Singiresu, S. R. (2011). *Mechanical vibrations*. Global Eds. Pearson.

Smith, R. (1990). The versailles railway accident of 1842 and the first research into metal fatigue. (retroactive coverage). *Fatigue 90*, 2033-2041.

Steinberg, D. S. (2000). *Vibration analysis for electronic equipment* (3rd ed.). John Wiley & Sons.

Wijker, J. (2018). *Miles' Equation in Random vibrations: Theory and applications in spacecraft structures design* (Vol. 248). Springer.

Yeşilçimen, Ü., & Kıral, Z. (2022, July 23-25). [Structural analysis and fatigue life evaluation of bracket type components subjected to random excitations]. Tenth international Istanbul scientific research congress proceedings book, Istanbul, Turkey. https://drive.google.com/file/d/1_fdMcSTOPbLOK13fNReMJirLDIZzQLyC/view

Zhou, Y., Fei, Q., & Wu, S. (2017). Utilization of modal stress approach in random-vibration fatigue evaluation. *Proceedings of the Institution of Mechanical Engineers, Part G: Journal of Aerospace Engineering*, *231*(14), 2603-2615.

Zigo, M., Arslan, E., Mack, W., & Kepplinger, G. (2019). Efficient frequency-domain based fatigue life estimation of spot welds in vehicle components. *Forschung im Ingenieurwesen*, *83*(4), 921-931.